Search for Long-Lived Neutral Particles decaying to Photons and Missing Tranverse Energy in *pp* Collisions at $\sqrt{S} = 8$ TeV

A DISSERTATION
SUBMITTED TO THE FACULTY OF THE GRADUATE SCHOOL
OF THE UNIVERSITY OF MINNESOTA
BY

Tambe Ebai Norbert

IN PARTIAL FULFILLMENT OF THE REQUIREMENTS
FOR THE DEGREE OF
Doctor of Philosophy

Prof. Yuichi Kubota

August, 2015

Acknowledgements

Humility is not about thinking less of yourself, rather, humility is thinking about yourself less.

There are many people that have earned my gratitude for their contribution to my time in graduate school.

So I would claim you are profoundly misled by thinking about physics as similar to logic or number theory. Its not! its dynamical evolution, and most results of physics problems are not nice numbers like 1 or π *or even* e^{π}.

Matt Strassler

The Universe is unbiased, she chooses to reveal herself to whoever she wants, irrespective of the label.

Norbert E. Tambe

Dedication

What ever it is that doesn't workout, get up...I think you've got to realized that there is no personal ambition you have which can be extinguished by anybody else...Only YOU by giving up your dreams can extinguish them. And if your dreams doesnt work out EXACTLY like you intended, it will still take you someplace interesting and you will make a DIFFERENCE. So, DON'T be AFRAID TO FAIL because you probably will whether you are afraid to or not and it's scary. You just gotta get out. The world belongs to tomorrow not yesterday. Don't give anybody else permission to take your life away, just keep living and keep giving and never make the perfect enemy the good. Never think that what I'm doing is too little to make a difference, THAT'S NOT TRUE!, THAT'S NOT TRUE! Do something everyday. Someday, for all of us, it will be our last day and what would matter will be all the steps we took along the way and what they amounted to, NOT the home run we hit on day X. I wish you well.
US Pres Bill Clinton, Dallas, TX

No, I have nothing against Mr. Einstein. He is a kind person and has done many good things, some of which will become part of the music. I will write to him and try to explain that the ether exists, and that its particles are what keep the Universe in harmony, and the life in eternity.
Nikola Tesla

Abstract

We have performed a search for events with delayed photons and large missing transverse momentum from the decay of neutral long-lived particles produced in proton-proton collisions with a center of mass energy, $\sqrt{S} = 8$ TeV at the LHC. Capitalizing on the excellent timing resolution of the CMS electromagnetic calorimeter, we searched for events with delayed photons using the measured photon arrival time at the electromagnetic calorimeter. We observed a single event, consistent with our background expectations from the standard model and proceed to set limits on the cross section, $\sigma_{\widetilde{\chi}_1^0} > 0.02$ pb, for the production and decay of the lightest neutralino ($\widetilde{\chi}_1^0$) with mass, $m_{\widetilde{\chi}_1^0} \geq 235$ GeV/c^2, and lifetime, $\tau_{\widetilde{\chi}_1^0} \geq 35$ ns, according to a R-parity conserving Gauge Mediated Supersymmetry Breaking model. We show, for the first time, that using only timing information from the CMS electromagnetic calorimeter, the CMS detector is sensitive to neutralinos with lifetimes up to 40 ns and masses up to 260 GeV/c^2. A description of timing measurement by the electromagnetic calorimeter and its performance is presented.

Contents

List of Tables

List of Figures

Chapter 1

Introduction

The search for a Long-Lived Neutral Particle (LLNP) produced in pp collisions at $\sqrt{S} = 8\,\text{TeV}$ by the Large Hadron Collider (LHC) on data recorded by the Compact Muon Solenoid (CMS) detector is presented in this thesis.

The Standard Model (SM) describes the interactions of fundamental particles with unmatched precision and has been very successful in terms of all its predictions of new particles and their properties agreeing with experiments. However, there are strong indications that the SM is incomplete. For example, the SM does not include gravity in its formulation and describes only visible matter, which is about 5 times less abundant than the total matter in the universe. The rest of the matter in the universe is referred to as Dark Matter (DM) [1, 2, 3], because we have very little understanding of it.

There are many extensions to the SM where DM and other new phenomena are described. LLNPs, which are not described by the, SM, are predicted to exist by many models generally referred to as Beyond the Standard Model (BSM) models. These LLNPs can decay into stable, neutral particles which are good candidates for DM particles and if they have low enough mass, may be produced and detected at the LHC. The signature for the decay of a LLNP, is the presence of Missing Transverse Energy (MET), which indicates the presence of an undetected DM particle candidate, and an electromagnetic particle like a photon which is detected late with respect to LHC pp collision times, in the same event. The combination of a late photon and large MET is the central idea in the search presented in this thesis.

The LHC completed a successful first long operation in 2012. Data from pp collisions during this period of operation (LHC RUN 1) was recorded by the CMS detector. The CMS detector was fully operational for nearly all of this period. The Electromagnetic Calorimeter (ECAL) recorded the arrival time and energy of electromagnetic particles produced from *pp* collisions with excellent resolution. This resolution was maintained through out the entire LHC RUN 1 by continuous energy and timing performance monitoring and calibration. The search for LLNPs in this data is presented here.

Understanding the signature of a LLNP in the CMS detector is provided by using samples of events generated in a Monte Carlo simulation of the production and decay of LLNPs.

This thesis is organized as follows: A brief introduction of the standard model, Supersymmetry (SUSY) and the description of GMSB models,[16], with LLNPs is presented in Chapters 2.

In Chapter 3, the LHC and CMS particle detector are described with an emphasis on the sub-detectors used in our search for LLNPs.

A description of the photon timing measurements made using the ECAL and its performance is discussed in Chapter 4, while the reconstruction of events and their constituent particles are described in Chapter 5, where the definition and measurement of quantities like MET and jets are presented.

Chapter 6 describes the search method in detail including the data samples used, observables, event selection requirements and background estimation techniques. The systematics arising from signal efficiency and acceptance in our signal event selection are also discussed in this chapter. In Chapter 7, we describe the statistical methods used to estimate the precision of the measurement.

Limits on the product of the production cross sections and the branching ratio for different lifetimes and masses of a LLNP is discussed in Chapter 8. The interpretation of our results in terms of the possible extensions to the SM by our analysis is also discussed in this chapter and in Chapter 9 the conclusions are presented.

Chapter 2

Phenomenology of Long-Lived Particles

2.1 The Standard Model

The Standard Model (SM) is a mathematical description of the fundamental components of matter and their interactions. Fermions are the building blocks of matter and their interaction is mediated by vector bosons. The SM describes the interactions of fermions through, the weak, electromagnetic and strong interactions but does not describe gravity. Fermions and bosons get their mass by interacting with a scalar boson in a process of spontaneous gauge symmetry breaking,[6].

2.1.1 Fermions

Half-integer spin ($\frac{1}{2}\hbar$) particles called *fermions* exist in nature, together with their anti-particles (particle with opposite charge), as either leptons (ℓ) or quarks (q). Fermions come in 3 *generations* or *flavors* and are arranged in a mass hierarchy, where the third generation fermions are the heaviest. The third and second generation fermions are meta-stable decaying to the first generation fermions which are stable. The heaviest SM fermion, which is the `top` quark (t) has a mass of $m_t = 173\,\mathrm{GeV}/c^2$, and a lifetime of about 10^{-24} seconds.

Quarks carry fractional electric charges and participate in weak and electromagnetic interactions and also in strong interactions, since in addition to the electric charge and a *color* charge. Each generation of quarks is a pair of an "*up-type*" and a "*down-type*" quark. The *Up-type* quarks (`up` (u), `charm` (c), `top` (t)) have a charge of $+\frac{2}{3}$, while the *down-type* quarks (`down` (d), `strange` (s), `bottom` (b)) have a charge of $-\frac{1}{3}$. Quarks do not exist as free particles in nature but as bound states of quarks and anti-quarks in the form of composite particles called *Hadrons*.

Leptons on the other hand exist free in nature and come in pairs consisting of a given lepton flavor and its corresponding neutrino. Leptons from all 3 generations (`electron` (e), `muon` (μ), `tau` (τ)) have a charge of -1, while their corresponding neutrinos (`electron neutrino` (ν_{e}), `muon neutrino` (ν_{μ}), `tau neutrino` (ν_{τ})) have a charge of 0. Leptons can participate only in weak and electromagnetic interactions. In Table 2.1, we present a summary of the fermions in each generation arranged according to the SM.

2.1.2 Bosons

Bosons have integer spins and they exists in nature in two types: scalar ($0\hbar$) and vector ($1\hbar$) bosons. Vector bosons are responsible for mediating the interactions between fermions and the only scalar boson (Higgs boson), discovered so far, provides mass to both fermions and bosons.

The vector bosons $\mathrm{W}^{\pm}$ (charged) and Z (neutral) are massive and mediate the *weak* interactions, while the massless vector bosons: *photon* (γ) and 8 *gluons* (g) mediate the *electromagnetic* and *strong* interactions, respectively [6, 7]. A summary of the interactions in the SM and their corresponding mediating vector bosons is presented in Table 2.2. The characteristic lifetimes of a particle decay involving each of the interactions is also shown in the Table. The longest lifetimes are characteristic of the weak interactions, explained partly because the mediating vector bosons is massive or the interaction strength is weakest.

2.1.3 Spontaneous Symmetry Breaking

In the SM, the weak, electromagnetic and strong interactions can be described using *gauge* symmetries and a *conserved quantum number* associated to the symmetry. The gauge symmetry of the SM is a combination of 3 different gauge symmetries

$$SU(3)_C \otimes SU(2)_L \otimes U(1)_Y. \tag{2.1}$$

where, $SU(3)_C$ is the gauge symmetry describing strong interactions with *color* (C) charge as its conserved quantum quantity. Quarks participate in strong interactions mediated by 8 gluons because of the color charge
$SU(2)_L \otimes U(1)_Y$ is the gauge symmetry describing the weak and electromagnetic interactions also known as the *electro-weak* interaction and the conserved quantum number derived from a combination of conserved quantum numbers: *isospin* (T_3) of $SU(2)_L$ and *hypercharge* (Y) of $U(1)_Y$ symmetry. After the spontaneous breaking of this electroweak symmetry ($SU(2)_L \otimes U(1)_Y \rightarrow U(1)_Q$), the resulting conserved quantum number describing the electromagnetic interaction which is based on the $U(1)_Q$ symmetry, is the electric charge, Q. The electric charge is related to T_3 and Y through the relation

$$Q = T_3 + \frac{Y}{2}. \tag{2.2}$$

Corresponding to the $SU(2) \otimes U(1)$ symmetry, are 4 massless vector bosons or *eigen* states, $W_\mu^{1,2,3}, B_\mu$, which combine to form the physical electro-weak vector bosons or *mass* states, $\mathrm{W}^\pm, \mathrm{Z}, \gamma$. These mass states are related to the eigenstates through a rotation which is expressed as

$$\mathrm{W}^\pm = \frac{W_\mu^1 \pm iW_\mu^2}{\sqrt{2}}, \qquad \begin{pmatrix} \gamma \\ \mathrm{Z} \end{pmatrix} = \begin{pmatrix} \cos\theta_w & \sin\theta_w \\ -\sin\theta_w & \cos\theta_w \end{pmatrix} \begin{pmatrix} B_\mu \\ W_\mu^3 \end{pmatrix} \tag{2.3}$$

The angle, θ_w, known as the *Weinberg angle*, relates the physical electric charge, e, to the coupling strengths, g and g' of $SU(2)_L$ and $U(1)_Y$ gauge symmetries, respectively, in a relation given as $e = g\sin\theta_w = g'\cos\theta_w$. This angle is one of the input parameters of the SM and has been measured from experiments to be equal to 28.726 degrees, which is equal to the arc cosine of the ratio of the mass of the W boson to that of the Z boson.

According to the SM, the only way to realize the massive vector bosons and explain how fermions get their mass is through the *Higgs mechanism*, [8], and involves spontaneously breaking the gauge symmetry of the SM, expressed as

$$SU(3)_C \otimes SU(2)_L \otimes U(1)_Y \xrightarrow{SSB\ into} SU(3)_C \otimes U(1)_Q. \tag{2.4}$$

In the SM, spontaneous symmetry breaking is realized through the potential of a spin-0 complex scalar field called the *Higgs boson*. The Higgs boson takes the representation of an weak isospin *doublet*. Its potential, $V(\phi^*, \phi) = \mu^2(\phi^*\phi) + \lambda(\phi^*\phi)^2$, is written in terms of the Higgs field (ϕ) and its complex conjugate (ϕ^*), where μ and λ are parameters. Among the many possible choices of configuration for this potential, only one particular configuration, represented by the choice of the parameters: $\mu^2 < 0$ and $\lambda > 0$, such that the minimum value of this potential, or the *Vacuum Expectation Value* (VEV) of the Higgs field, $|\phi_0| = \sqrt{\frac{-\mu^2}{\lambda}} = \nu = 246\,\mathrm{GeV}$, spontaneously breaks the $SU(2)_L \otimes U(1)_Y$ symmetry into a $U(1)$ symmetry. This particular configuration of the potential of the Higgs field is shown in Figure 2.1.

Fermions acquire their mass through their interaction with the Higgs field and the fermion's mass, m_f, is proportional to the strength of its interaction (Yukawa coupling λ_f) with the Higgs field. The relationship between the masses of the fermions and the W,Z masses is given in Equation 2.5.

The massive vector bosons, Z and $\mathrm{W}^{\pm}$, obtain their mass, $m_Z = 91\,\mathrm{GeV}/c^2$ and $m_{\mathrm{W}^\pm} = 80\,\mathrm{GeV}/c^2$, respectively, by engulfing or "*eating*" the available massless components (*Nambu-Goldstone bosons*) of the complex Higgs doublet. Out of the four scalar fields, only one physically massive scalar particle *Higgs boson* remains. The masses of the charge and neutral vector bosons, given in Equation 2.5, are connected through the cosine of the *Weinberg angle.*

$$m_f = \lambda_f \frac{\nu}{\sqrt{2}}, \qquad \frac{m_{W^\pm}}{m_Z} = \frac{\frac{1}{2}\nu g}{\frac{1}{2}\nu\sqrt{g^2 + g'^2}} = \cos\theta_w \tag{2.5}$$

It took nearly 40 years for the Higgs boson to be discovered after its prediction in the 1960s. The Higgs boson was discovered at CERN on July 04, 2012, through its decay into two photons, $\mathrm{H} \to \gamma\gamma$, and a pair of Z bosons, $\mathrm{H} \to \mathrm{ZZ}$, channels. Its mass has been measured to be, $m_H = 125 \pm 0.21\,\mathrm{GeV}/c^2$. As shown in Figure 2.2, every SM particle interacts with the Higgs boson either directly or indirectly as in the case for photons and gluons.

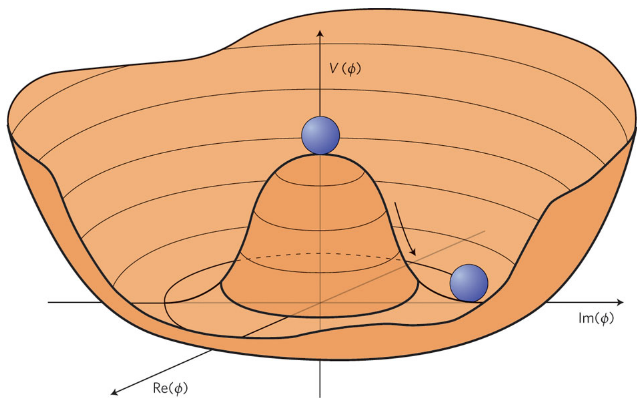

Figure 2.1: Higgs boson "Mexican hat" potential, $V(\phi^*\phi) = \mu^2(\phi^*\phi) + \lambda(\phi^*\phi)^2$, which leads to spontaneous symmetry breaking with choice of parameters $\mu^2 < 0$, $\lambda > 0$.

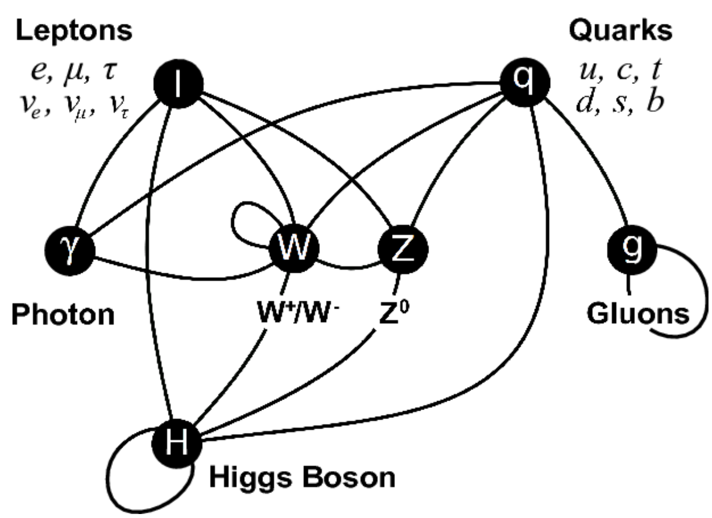

Figure 2.2: Fermions and bosons and their interactions in the SM. All bosons (except the Higgs) mediate interactions between fermions.

Fermions	**Generation**			**Charge**
	`First`	`Second`	`Third`	
Leptons	$\begin{pmatrix} \mathrm{e}^- \\ \nu_\mathrm{e} \end{pmatrix}$	$\begin{pmatrix} \mu^- \\ \nu_\mu \end{pmatrix}$	$\begin{pmatrix} \tau^- \\ \nu_\tau \end{pmatrix}$	$\begin{pmatrix} -1 \\ 0 \end{pmatrix}$
Quarks	$\begin{pmatrix} \mathrm{u} \\ \mathrm{d} \end{pmatrix}$	$\begin{pmatrix} \mathrm{c} \\ \mathrm{s} \end{pmatrix}$	$\begin{pmatrix} \mathrm{t} \\ \mathrm{b} \end{pmatrix}$	$\begin{pmatrix} +\frac{2}{3} \\ -\frac{1}{3} \end{pmatrix}$

Table 2.1: Fermions of the SM. Particle symbols are explained in text.

Bosons	**Interaction**	**Symmetry**	**Characteristic Lifetime**
$\mathrm{W}^{\pm}$,Z	Weak	$SU(2)_L \otimes U(1)_Y$	10^{-8} to 10^{-13} seconds
γ	Electromagnetic	$U(1)_Q$	10^{-14} to 10^{-20} seconds
g	Strong	$SU(3)_C$	$< 10^{-22}$ seconds

Table 2.2: Interaction mediating vector bosons in the SM and the characteristic lifetime of the interaction.

2.1.4 Beyond Standard Model Physics

The Higgs boson is a crucial component in the formulation and experimental success of the SM, yet the SM itself provides no explanation for the above choice of parameters ($\mu^2 < 0$ and $\lambda > 0$) of the Higg's potential or whether there is only one type of Higgs field with which all fermions couple to obtain their mass. Some Beyond the Standard Model (BSM) models, like *Supersymmetry*, allow for the possibility of more than one Higgs field and predicts the existence of additional particles to those in the SM. The following are some of the reasons for the interest in BSM physics, particularly Supersymmetry:

The Hierarchy Problem

Predictions of the Higgs boson's mass, m_H^2, by the SM, include corrections to the Higgs boson's mass, δm_f^2, from its coupling with fermion. These corrections from first order interaction (1-loop level) of the Higgs boson with fermions are computed using the Feynman diagram shown in Figure 2.3(a) and given as

$$\delta m_f^2 = \frac{1}{16\pi^2}|\lambda_f|^2\left(-2\Lambda^2 + 6m_f^2 \ln\left(\frac{\Lambda}{m_f}\right) + ...\right) \tag{2.6}$$

where, λ_f is the coupling parameter of the Higgs boson to fermions with the interaction Lagrangian density written as $\lambda_f H\bar{f}f$. Λ represents an arbitrary high energy scale (of the order 10^{18} GeV) known as the *cut-off* energy scale. Because $\Lambda = 10^{18}$ GeV is very large, we would expect the correction to the Higgs boson's mass to also be very large eventually making the Higgs boson's mass, m_H^2, to be very large. However, the Higgs boson's mass measured from experiment is only about 125 GeV/c^2. A dilemma thus arises, if one is to trust SM predictions of the Higgs boson's mass, why are all these large corrections to the Higgs boson's mass not observed in experiments? The SM cannot provide an explanation for this. This problem is known as the *Hierarchy problem*.

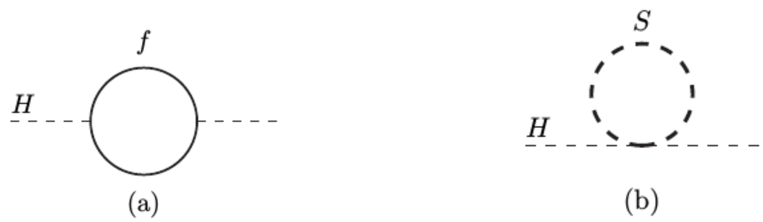

Figure 2.3: Higgs mass contributions arising from the Higgs field coupling to fermions (a) and scalar (b) fields.

SUSY, on the other hand, provides a plausible explanation as to why these corrections are not observed in experiments. In SUSY models, there are in addition to the scalar Higgs boson new supersymmetric scalar particles, which are yet to be observed, that can also couple to the Higgs field as shown in the 1-loop Feynman diagram in Figure 2.3(b). The contributions to the Higgs boson's mass from these new scalar supersymmetric particles, δm_S^2, is computed at the order of 1-loop and given as

$$\delta m_S^2 = \frac{1}{16\pi^2}|\lambda_S|^2 \left(\Lambda^2 - 2m_S^2 \ln\left(\frac{\Lambda}{m_S}\right) + ...\right) \tag{2.7}$$

where λ_S is also the coupling constant of the Higgs field to the new scalar particle given as, $\lambda_S HS\bar{S}$. An interesting observation comparing Equations 2.6 to Equation 2.7, up to the Λ^2-terms is that their signs are different. The opposite sign corrections to the Higgs boson's mass cancel each other and as a result their net contribution to the Higgs mass, m_H^2 is zero. This cancellation which happens at all orders of corrections is the reason why one does not observe very large Higgs boson mass from experiment.

Dark Matter and Long-Lived Particles

There is ample evidence [1], that dark matter (matter which does not interact with light) exists in the universe, and if this form of matter is made of particles, then the lifetime of a dark matter particle must be comparable to the age of the universe. Furthermore, it must also be neutral. Such neutral stable particles are not part of the SM. Therefore, dark matter particles must certainly posses a new kind of interaction.

Long-Lived Neutral Particles (LLNP) which are meta-stable (particles that are stable for a period of time and then decay) and can decay into possible dark matter particles through new kind of interactions also do not exist in the SM. These LLNPs are predicted, by BSM models, to have lifetimes longer than the characteristic lifetimes of particles and interactions in Table 2.2. In addition to Supersymmetry providing a possible explanation for stability of the Higgs boson's mass, it also predicts the existence of LLNPs, which can decay into dark matter candidate particles with lifetime beyond those of the SM [2, 3, 16, 4, 5, 18]. These LLNPs decay into dark matter candidate particles through new kind of interactions. Such predictions from Supersymmetry have motivated many of the studies of Supersymmetry as an interesting candidate among many models beyond the SM, in both theory and experiment. It is certainly a motivation for the study presented in this thesis.

2.2 Supersymmetry

Suppersymmetry (SUSY) relates space-time symmetries (rotation and translation) to gauge symmetries ($SU(3)_C \otimes SU(2)_L \otimes U(1)_Y$) [10, 11]. The generators of SUSY, Q, transform fermions to bosons and bosons to fermions;

$$\mathrm{Q}|\mathbf{Fermion}\rangle = |\mathbf{Boson}\rangle, \quad \mathrm{Q}|\mathbf{Boson}\rangle = |\mathbf{Fermion}\rangle, \tag{2.8}$$

and as a consequence, the fermions and their corresponding bosons have the same mass.

2.2.1 The Minimal Supersymmetric Standard Model

The *Minimal Supersymmetric Standard Model* (MSSM) uses only one SUSY generator,Q, in its formulation as an extension of the SM, to include the supersymmetric partners of the particles in the SM. The number of fundamental particles in the MSSM is obviously doubled, however, the gauge symmetries are the same. Supersymmetric particles and their SM counterparts differ by a half-integer in spin (s). Bosons (fermions) in the SM have superpartners which are fermions (bosons).

Two complex Higgs doublets are required in the MSSM, $\mathbf{H_d} = (H_1^0, H_1^-)$ and $\mathbf{H_u} = (H_2^+, H_2^0)$ to give mass to the down-typed quarks (and leptons) and to the up-typed quarks, respectively. Particles interact with the Higgs bosons through a superpontential through dimensionless Yukawa couplings to acquire masses. Details of the nature of these interactions and spontaneous SUSY breaking can be found in [12, 13, 15].

The names of supersymmetric particles are derived from their SM counterparts by adding an "s" in front of the SM particle name. For example, a *selectron* is the supersymmetric partner of the electron, *squarks* are the supersymmetric partners of SM quarks. The symbol of SUSY particles carry the "˜" sign above the symbol. For example if q is a SM particle then its supersymmetric partner is written as $\widetilde{q}$. Superpartners of bosons are indicated with the suffix "-ino ", as in *wino* and *gluinos*.

The superpartners of SM fermions are scalars called *sfermions* ($\tilde{l}$), sneutrinos ($\tilde{\nu}$) and squarks ($\tilde{q}$) while *gluinos* ($\tilde{g}$) are the superpartners of the massless gauge bosons of strong interaction, gluons. The vector bosons ($\mathrm{W}^{\pm}$,W^0,B) have fermionic superpartners called *Winos* and *Binos*.

Standard Model			Supersymmetry		
Particle	Symbol	Spin	Particle	Symbol	Spin
quark	q	$\frac{1}{2}$	squark	$\widetilde{q}$	0
lepton	ℓ	$\frac{1}{2}$	slepton	$\widetilde{\ell}$	0
W Bosons	$\mathrm{W}^{\pm}$,W^0	1	Wino	$\tilde{W}^{\pm}, \tilde{W}^0$	$\frac{1}{2}$
B Boson	B	1	Bino	$\widetilde{\mathrm{B}}$	$\frac{1}{2}$
gluon	g	1	gluino	$\widetilde{\mathrm{g}}$	$\frac{1}{2}$
Higgs Bosons	H $\times 4$	0	higgsino	$\widetilde{\mathrm{H}}$ $\times 4$	$\frac{1}{2}$
Graviton	G	2	gravitino	$\tilde{G}$	$\frac{3}{2}$

Table 2.3: Particles in the MSSM. SUSY particles (sparticles) have a "˜" on the symbol

Particle Names	Gauge eigenstates	Mass eigenstates
squark	$\widetilde{q}$	$\widetilde{q}$
slepton	$\widetilde{\ell}$	$\widetilde{\ell}$
Neutralinos	$\tilde{W}^0, \tilde{B}^0, \tilde{H}_1^0, \tilde{H}_2^0$	$\tilde{\chi}_1^0, \tilde{\chi}_2^0, \tilde{\chi}_3^0, \tilde{\chi}_4^0$
Charginos	$\tilde{W}^+, \tilde{W}^-, \tilde{H}^+, \tilde{H}^-$	$\tilde{\chi}_1^{\pm}$,$\tilde{\chi}_2^{\pm}$
Higgs bosons	$H_1^0, H_2^0, H_1^-, H_2^+$	$h^0, H^0, A^0, H^{\pm}$
gluino	$\tilde{g}$	$\tilde{g}$
Gravitino	$\tilde{G}$	$\tilde{G}$

Table 2.4: Gauge and mass eigenstates of SUSY particles in the Minimal Supersymmetric SM (MSSM).

The superpartners of these Higgs bosons ($H_1^0, H_2^0, H_1^-, H_2^+$) are fermions called *higgsinos* ($\tilde{H}_1^0, \tilde{H}_1^-, \tilde{H}_2^0, \tilde{H}_2^+$) while the superpartners of the gauge bosons are called *gauginos* ($\tilde{B}^0, \tilde{W}^0, \tilde{W}^-, \tilde{W}^+$). The neutral gauginos and higgsinos ($\tilde{B}^0, \tilde{W}^0, \tilde{H}_1^0, \tilde{H}_2^0$) mix together to form four neutral fermions called *Neutralinos* ($\tilde{\chi}_1^0, \tilde{\chi}_2^0, \tilde{\chi}_3^0, \tilde{\chi}_4^0$), and the charged gauginos and higgsinos ($\tilde{W}^-, \tilde{W}^+, \tilde{H}_1^-, \tilde{H}_2^+$) mix together to form four charged fermions called *Charginos* ($\tilde{\chi}_1^\pm$,$\tilde{\chi}_2^\pm$). The mass of the neutralinos and charginos depend on the mixing parameters of these gauginos and higgsinos and is model dependent.

We summarize in Tables 2.3 and 2.4 particles in the MSSM and how they relate to their SM partners. The gauge and mass eigen mass states of fermionic supersymmetric particles in the MSSM is also shown.

R-Parity

In supersymmetry, it is, in principle, acceptable to include terms in the MSSM Lagrangian density which may not conserved quantum numbers like the *baryon* (B) and *lepton* (L) numbers. For example, a consequence of adding such a term is that predictions of the proton's lifetime is much shorter than measured in experiments. Since no such phenomenon which violate these quantum numbers have been observed in experiments, SUSY models are constructed with the introduction of an additional matter symmetry called *R-Parity*, which relates the quarks to leptons through the baryon and lepton numbers. R-parity is defined as

$$R_P = (-1)^{3(B-L)+2S} \tag{2.9}$$

where, S is the particle's spin. SM particles like quarks have an *even* R-parity, $R_P = 1$, while supersymmetric particles like squarks have odd parity $R_P = -1$.
The phenomenological consequence of R-parity are the following: first, in the decay of supersymmetric particles, the lightest SUSY particle (LSP) have odd parity, $R_P = -1$, it is electrically neutral and considered to be absolutely stable. This makes the LSP a good dark matter candidate particle [2, 5], second, every supersymmetric particle produced will eventually decay into an odd number of LSPs, third, supersymmetric particles can only be produced in pairs. This phenomenological consequences make *R-parity Conserving* (RPC) SUSY models very attractive for experimental studies.

Cross Sections, Decay Rate and Branching Ratio

Cross Section

The cross section of producing a particle at a collider, like the LHC, is the probability that the proton beams will collide and interact in a certain way to produce the particle. The cross sections provides a way of counting the number of the particle produced when these proton beams collide. The cross section of producing a supersymmetric particle at the LHC depends on the following: the available energy of the proton beams compared to the mass of the particle, the type of interaction or size of the couplings during collision and the flux of the proton beams. Since the predicted mass of supersymmetric particles is higher than that of SM particles, we expect very few supersymmetric particles, if any, to be produced at the LHC, and even fewer supersymmetric particles for massive particles. The typical cross section of producing a supersymmetry particle at the LHC is of the order of 1 $pb = 10^{-12} \times 10^{-24}$ cm^2 or at times 1 $fb = 10^{-15} \times 10^{-24}$ cm^2 for extremely rare SUSY processes which can be compared to that for a standard model process, like, the production of the Z or W$^{\pm}$ bosons which is of the order of a few $nb = 10^{-9} \times 10^{-24}$ cm^2.

Supersymmetric particles are most likely to be produced at the LHC, through the process of strong interactions ($pp \rightarrow \widetilde{\mathrm{g}}\widetilde{\mathrm{g}}, \widetilde{q}\widetilde{q}$) than electro-weak interactions processes ($pp \rightarrow \widetilde{\chi}^{\pm}\widetilde{\chi}^{\mp}, \widetilde{\chi}^{0}\widetilde{\chi}^{\pm}$), since the cross section for strong interaction processes is larger. Figure 2.4, shows the cross section, on the vertical y-axis, against the mass of the supersymmetric particle, on the horizontal x-axis. With $20\,\mathrm{fb}^{-1}$ of LHC integrated luminosity (relates the cross section and the rate of particle produced) of data from proton-proton (pp) collisions at $\sqrt{S} = 8\,\mathrm{TeV}$, we expect to see more events (vertical z-axis) with supersymmetric particles produced at the LHC through strong interactions than electro-weak interactions for a given SUSY sparticle mass.

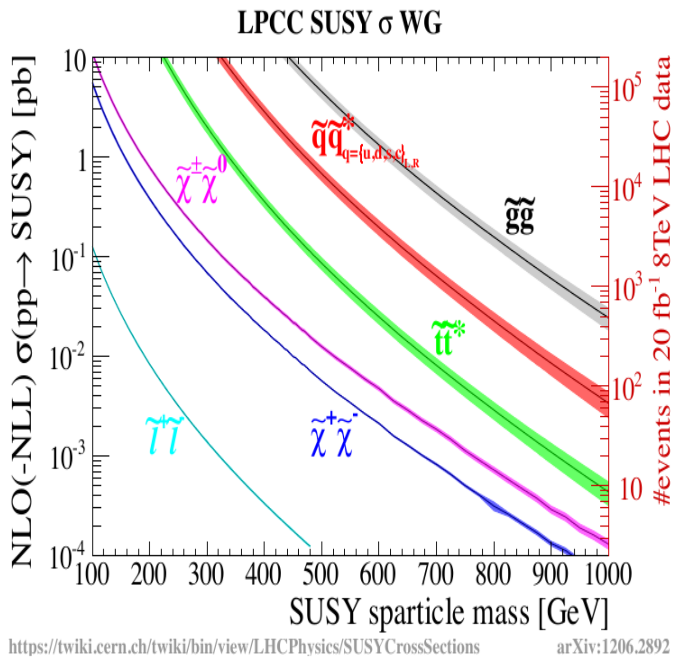

Figure 2.4: Cross section against SUSY sparticle mass for producing supersymmetric particles in different modes of interactions at the LHC. More supersymmetric particles are produced through strong interaction, $pp \rightarrow \widetilde{g}\widetilde{g}$, processes than the any other process.

Decay Rate and Branching Ratio

After the production of a SUSY sparticle, the particle may decay either immediately after it was produced to live for a while before it decays. The rate at which the SUSY sparticle decays is called the *decay width* (Γ) and it is related to the mean lifetime (τ) through the relation

$$\tau = \frac{\hbar}{\Gamma}. \tag{2.10}$$

Since the decay width depends on the coupling or the mass difference between the SUSY sparticle and its decay products, SUSY particles with small mass differences of large coupling to the daughter particles has smaller decay width and therefore have long lifetimes. The final products of the decay depends on the branching ratio for a given decay channel. In R-parity conserving models, SUSY sparticles are produced in pairs and each decay through a cascade decay process into the LSP and its SM partner.

A SUSY sparticle may decay through strong interactions in which case its mean lifetime is about 10^{-17} to 10^{-25} seconds, through electromagnetic interactions in which case its mean lifetime maybe between 10^{-20} seconds to about 10^{-14} seconds and through weak interactions in which case its mean lifetime maybe vary from 10^{-13} seconds to 10^{-8} seconds.

By Long-lived particles, we are interested in particles decays through none of the SM interactions and has a typical mean lifetime ranging from a few nanoseconds to hundreds of a nanosecond. These are the kind of long-lived particles we study in this thesis.

2.2.2 Gauge Mediated Supersymmetry Breaking Models

A consequence of SUSY is that supersymmetric particles and their SM partners must have the same mass. However, because no supersymmetric particle have been observed with the same mass as SM particles, it means SUSY is not an exact symmetry of nature and must be broken. SUSY breaking should happen such that the mass of supersymmetric particles are higher than their standard model counterparts. The two ways of breaking SUSY are explicit and spontaneous breaking. Similar to the motivation of spontaneous symmetry breaking through the Higgs mechanism in the SM, spontaneous SUSY breaking is theoretically favored because it preserves renormalisability also in the MSSM. SUSY breaking is realized by introducing SUSY-breaking terms known as *soft breaking terms* to the Lagrangian density, which ensures that coupling constants which may lead to quadratic divergence are not introduced and the mass of the supersymmetric particles can be at about the TeV energy scale [13, 14, 15]. In theory SUSY breaking happens in the so-called *Hidden Sector* [14], and can be mediated to the MSSM sector through interactions which do not change the flavor of the particles called *flavor blind interactions* e.g. gauge interactions [16]. SUSY models based on gauge interactions mediating SUSY breaking from hidden sector to MSSM sector are called *Gauge Mediated Supersymmetry Breaking* (GMSB) models. GMSB models are interesting at an experimental level because they predict the existence of long-lived particles which can decay into light gravitino, a spin-3/2 superpartner of the graviton field, which is a good candidate dark matter particle since it is stable and neutral.

Gauge Mediated Supersymmetry Breaking (GMSB) models are based on the idea that *Messenger* particles through gauge interactions are responsible for mediating SUSY breaking from the *hidden sector* to the visible or MSSM sector. The energy scale of the hidden sector, which is the Vacuum Expectation Value (VEV) of scalar fields responsible for SUSY breaking (some kind of *superHiggs mechanism*, [14]) is denoted by a fundamental parameter, $\mathbf{F}$, also known as the *Fundamental SUSY Breaking Parameter*. The mass of the messenger particle, $\mathbf{M}_{\text{mess}}$, is related to $\mathbf{F}$ through an *effective* SUSY breaking energy scale parameter, $\mathbf{\Lambda}$, at the MSSM level. This relationship can be written as $\mathbf{F}/\mathbf{\Lambda} = \mathbf{M}_{\text{mess}}$ and $\mathbf{\Lambda}$ can be interpreted as the energy scale at which SUSY breaking is felt by the MSSM particles.

For a given choice of the value of $\mathbf{F}$, the mass spectrum of all supersymmetric particles including the Lightest SUSY Particle (LSP) is well defined. Since the value of $\mathbf{F}$ is not known and can vary, the mass of the LSP can also vary. This variation of the fundamental SUSY breaking scale or equivalently the mass of the LSP is parametrized by a scaling parameter, C_{grav}.

In GMSB models and in SUSY models in general, the value of the VEVs, v_u and v_d, of the two Higgs doublets in the MSSM is not known and is therefore an additional parameter, $\tan(\beta)$, in most models. This parameter relates the VEVs; $\tan(\beta) = \frac{v_u}{v_d}$. Another parameter, $sgn(\mu)$, defines the sign, which is arbitrary, of the parameter μ in the Higgs Boson's potential.

Thus, in GMSB models there are only (compared to the SM which has at least 19) 5 input parameters given as

$$\{\mathbf{\Lambda}, \quad \mathbf{M}_{\text{mess}}, \quad \mathbf{N}_5, \quad \tan(\beta), \quad sgn(\mu), \quad C_{grav}\} \tag{2.11}$$

where, $\mathbf{N}_5$ is the number of messenger particles mediating SUSY breaking. Different choices for the values of these parameters will represent different scenarios for GMSB models.

A unique feature in GMSB models is that the mass of the Lightest SUSY Particle (LSP) can be made (through C_{grav}) to be as light as possible in order for a model prediction of the mass of the dark matter candidate particle to agree with bounds from cosmology. In GMSB models, the LSP is most certainly the gravitino ($\tilde{G}$) as long as, $\mathbf{M}_{\text{mess}}$ is very small compared to M_{Pl}, the energy scale where gravitational interactions become relevant. The gravitino's mass, $m_{\tilde{G}}$, can be expressed in terms of the parameter

C_{grav} and M_{Pl} as

$$m_{\tilde{G}} = C_{grav} \cdot \frac{\mathbf{\Lambda M}_{\text{mess}}}{\sqrt{3}\mathrm{M}_{pl}} \tag{2.12}$$

where, $\mathrm{M}_{Pl} = 1.3 \times 10^{19}$ GeV/c^2. By varying the scaling parameter, C_{grav}, the mass of the gravitino will also vary and the decay rate of the Next-to-Lightest-Supersymmetric Particle (NLSP) to the gravitino will also vary. Varying the decay rate will vary the lifetime of the NLSP from decaying immediately or promptly to being long-lived. The decay rate of the NLSP to the gravitino depends on the mass difference between the NLSP and the gravitino and also on the coupling or strength of its interaction with the gravitino, [16, 17].

2.3 Long-Lived Neutral Particles in GMSB Models

In GMSB, *gravitino-scalar-chiral fermion* $((\psi, \tilde{G}, \phi))$ and *gravitino-gaugino-gauge boson* $((\lambda, \tilde{G}, \mathrm{A}))$ interactions, between the gravitino and its partners in the same supermultiplet, shown in Figure 2.5, are present. These interactions allow for any supersymmetric particle, $\tilde{P}$, to decay to its SM partner, P, and the gravitino $(\tilde{G})$, with its decay rate suppressed because of the nature of the interaction coupling strength contributing as $\frac{1}{\sqrt{\mathbf{F}}}$.

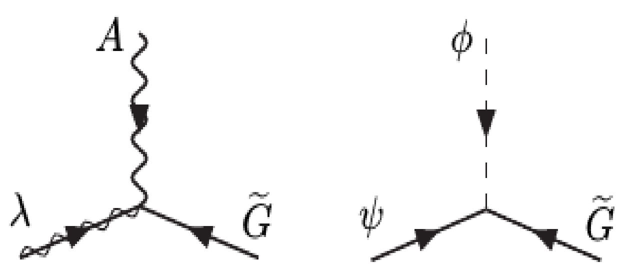

Figure 2.5: Feynman diagrams of Gravitino-Gaugino $((\lambda, \mathrm{A}))$ (*left*) and Gravitino-Scalar $((\psi, \phi))$ (*right*) couplings. The coupling strength goes like $\frac{1}{\sqrt{\mathbf{F}}}$

The decay rate for $\tilde{P} \to P + \tilde{G}$ can be computed as

$$\Gamma(\tilde{P} \to P + \tilde{G}) = \frac{m^5_{\tilde{P}}}{16\pi \mathbf{F}^2} \left(1 - \frac{m^2_P}{m^2_{\tilde{P}}}\right)^2 \tag{2.13}$$

where, the terms in the the decay rate are due to the nature of the interaction and also from the kinematic phase space integral where the mass of the gravitino can be neglected in the computation.
The decay width is larger for smaller values of fundamental SUSY breaking parameter, $\mathbf{F}$ or equivalently for smaller gravitino masses, $\mathrm{m}_{\tilde{G}}$. If we re-write the fundamental SUSY breaking scale as $\mathbf{F} = C_{grav} \cdot \mathrm{m}_{\tilde{G}}\sqrt{3}\mathrm{M}_{pl}$, we see that for different values of C_{grav}, which signifies changing the mass of the gravitino or the fundamental SUSY breaking scale, the decay width can also be vary. Thus, by varying the decay width, we can vary the lifetime of the supersymmetric particle $\tilde{P}$, for fixed mass, from being prompt to being long-lived.
In a scenario where the, SUSY particle $\tilde{P}$ is not the Next-To-Lightest Supersymmetric Particle (NLSP), the decay, $\tilde{P} \to P + \tilde{G}$, suffers from competition with other probably favorable decay channels and this process is not competitive enough to happen at a collider experiment. However, if $\tilde{P}$ is the NLSP, then there is no competition and this decay is always sure to happen at a collider.

It is important to observe here that, because the decay rate is large for smaller values of the fundamental SUSY breaking scale or equivalently smaller gravitino mass for a fixed lightest neutralino mass, if m_{NLSP} is of the order of 100 GeV or more and $\sqrt{\mathbf{F}} \ll 1000$ TeV, meaning $m_{\tilde{G}} \leq 1$ keV, then the above decay rate is of the order that can be observed at hadron collider detectors.

2.3.1 Benchmark Scenario

In this thesis, we focus on a benchmark working model of R-parity conserving GMSB models called the *Snowmass Point and Slopes* (SPS8),[18]. In the SPS8 model, the following choice of GMSB parameters are made:

$$\mathbf{M}_{\text{mess}} = 2\mathbf{\Lambda} \quad \tan(\beta) = 15 \quad \mathbf{N}_5 = 1 \tag{2.14}$$

where $\mathbf{\Lambda}$ and C_{grav} are the free to vary.
The LSP is the gravitino ($\tilde{G}$) and the lightest neutralino ($\widetilde{\chi}_1^0$) is the NLSP. Since the $\widetilde{\chi}_1^0$ is a mixture of the supersymmetric particles Bino ($\tilde{B}^0$), Wino ($\tilde{W}^0$), higgsino ($\tilde{H}_u^0, \tilde{H}_d^0$), its decay to its SM partner and the gravitino will depend on the choice of parameters which affect the mixing. Since the parameters: Λ, $\tan\beta$, and $sgn(\mu)$ do affect the mixing, these parameters have been choosen in the SPS8 model to maximize the branching ratio involving the decay of the $\widetilde{\chi}_1^0$ to a photon (γ) and a gravitino over the other possible SM partners: Z boson, Z') and a higgs boson (h), [17].
Thus, this thesis duels on the search for decay of the lightest neutralino, $\widetilde{\chi}_1^0$, as a LLNP, to a photon and the gravitino, $\widetilde{\chi}_1^0 \to \gamma + \tilde{G}$. By varying $\mathbf{\Lambda}$ and C_{grav}, we study the production and decay of $\widetilde{\chi}_1^0$ for different masses and lifetimes.

Supersymmetric Particle Mass Spectra

The masses of all supersymetric particles (sparticles) is determined by the effective SUSY breaking energy scale parameter, $\mathbf{\Lambda}$ and increases with increasing values of $\mathbf{\Lambda}$. Shown in Figure 2.6 , the sparticle mass spectra for $\mathbf{\Lambda} = 100\,\text{TeV}$ (left plot) and $\mathbf{\Lambda} = 180\,\text{TeV}$ (right plot) with the same values of $C_{grav} = 93.5$ computed according to the SPS8 model. As observed in the Figure, the mases of the sparticles, including the mass of the lightest neutralino, $\widetilde{\chi}_1^0$, is larger for $\mathbf{\Lambda} = 180\,\text{TeV}$ ($m_{\widetilde{\chi}_1^0} = 256\,\text{GeV}/c^2$) (right plot) than for $\mathbf{\Lambda} = 100\,\text{TeV}$ ($m_{\widetilde{\chi}_1^0} = 140\,\text{GeV}/c^2$) (left plot). This means that, in order to expand our search include heavier lightest neutralinos, we must scan large values of $\mathbf{\Lambda}$.

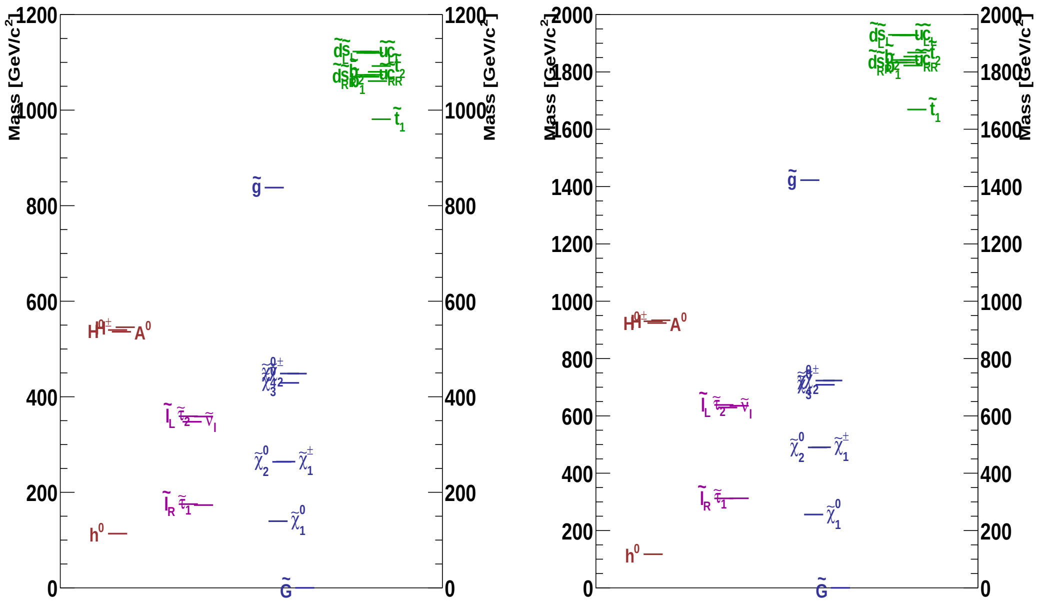

Figure 2.6: SUSY mass spectra for benchmark SPS8 model: $\mathbf{\Lambda} = 100$ TeV (left) and $\mathbf{\Lambda} = 180$ TeV (right) with $C_{grav} = 93.5$. SUSY particle mass increases with $\mathbf{\Lambda}$

Lightest Neutralino as Long-Lived Neutral Particle

The lifetime of the lightest neutralino, $\widetilde{\chi}_1^0$, in its decay; $\widetilde{\chi}_1^0 \rightarrow \gamma + \tilde{G}$, expressed in terms of its mass, $m_{\widetilde{\chi}_1^0}$ and the supersymmetry breaking scale, $\mathbf{F}$, is given as

$$c\tau_{\widetilde{\chi}_1^0} \approx \left(\frac{m_{\widetilde{\chi}_1^0,}}{\text{GeV}}\right)^{-5}\left(\frac{\sqrt{\mathbf{F}}}{\text{TeV}}\right)^{4} \tag{2.15}$$

and in terms of the parameter changing the $\widetilde{\chi}_1^0$ lifetime, C_{grav}, Equation 2.15 becomes

$$c\tau_{\widetilde{\chi}_1^0,} \approx C_{grav}^2\left(\frac{m_{\widetilde{\chi}_1^0}}{\text{GeV}}\right)^{-5}\left(\frac{\sqrt{\mathbf{\Lambda}\cdot\mathbf{M}_{\text{mess}}}}{\text{TeV}}\right)^{4}. \tag{2.16}$$

Thus, by changing the value of C_{grav}, we change the lifetime of $\widetilde{\chi}_1^0$, similar to changing the value of $\mathbf{\Lambda}$, we get $\widetilde{\chi}_1^0$ with different masses.

The probability for a neutralino ($\widetilde{\chi}_1^0$), produced with energy $\mathrm{E}_{\widetilde{\chi}_1^0}$ and mass $m_{\widetilde{\chi}_1^0}$ to travel a distance x before decaying to a photon and gravitino in the laboratory frame can be expressed as $\mathcal{P}(x) = 1 - \exp\left(-\frac{x}{\mathrm{L}}\right)$, where the distance traveled in a particle detector by the neutralino is given by Equation 2.17.

$$\mathrm{L} = \left(c\tau_{\widetilde{\chi}_1^0}\right) \cdot (\beta\gamma)_{\widetilde{\chi}_1^0} \tag{2.17}$$

From Equation 2.17, it is clear that this distance depends on two main factors. The boost factor, $(\beta\gamma)_{\tilde{\chi}_1^0} = \frac{|\vec{p}_{\tilde{\chi}_1^0}|}{m_{\tilde{\chi}_1^0}} = \sqrt{\left(\frac{E_{\tilde{\chi}_1^0}}{m_{\tilde{\chi}_1^0}}\right)^2 - 1}$, which indicates how fast the neutralino is traveling before it decays. For slow moving neutralino, $(\beta\gamma)_{\tilde{\chi}_1^0} \ll 1$.

In this theses, we are interested in the production of the lightest neutralino from strong interaction processes like $pp \to \widetilde{\mathrm{g}}\widetilde{\mathrm{g}}, \widetilde{q}\widetilde{q}$, as these processes have a higher production cross section at the LHC. These are called direct production processes, where the $\widetilde{\chi}_1^0$ is a product of the *cascade decay* of squarks ($\widetilde{q}$), excited squarks ($\widetilde{q}^{\star}$) and gluinos ($\widetilde{\mathrm{g}}$). The Feynmann diagrams in Figure 2.7 represent the different $\widetilde{\chi}_1^0$ production processes at the LHC, through the cascade decay of gluinos and squarks. The final state may include two photons (left Feynmann diagrams) and two gravitinos if both $\widetilde{\chi}_1^0$ decay to a photon and a gravitino or just a single photon (right Feynmann diagrams) if only one $\widetilde{\chi}_1^0$ decay to a photon and gravitino.

Our signal events are events produced at the LHC with at least a single photon which is late, with respect to LHC pp collision times and large Missing Transverse Energy or MET. The MET is due to the presence of at least a single gravitino which escapes undetected.

The Squarks and gluinos could directly decay into gravitinos and their SM partners, however, as explained previously, the direct decay to gravitino channel is competing with other channels which are most favorable which through cascade decay eventually produces the gravitino through the $\widetilde{\chi}_1^0$.

The photon arrival time at the detector from the $\widetilde{\chi}_1^0$ decay depends on the $\widetilde{\chi}_1^0$ lifetime $c\tau$, and the whether the $\widetilde{\chi}_1^0$ is produced with a high (moving fast) boost or low boost (moving slow). This means that the momentum ($p_{\widetilde{\chi}_1^0}$) of the $\widetilde{\chi}_1^0$ during production from gluino or squarks decays must be much smaller than the its mass, $m_{\widetilde{\chi}_1^0}$. Lightest neutralinos ($\widetilde{\chi}_1^0$ s) produced such that the $\widetilde{\chi}_1^0$ is moving slow, $p_{\widetilde{\chi}_1^0}/m_{\widetilde{\chi}_1^0} \ll 1$, are definitely good candidates for producing photons which arrive the detector late.

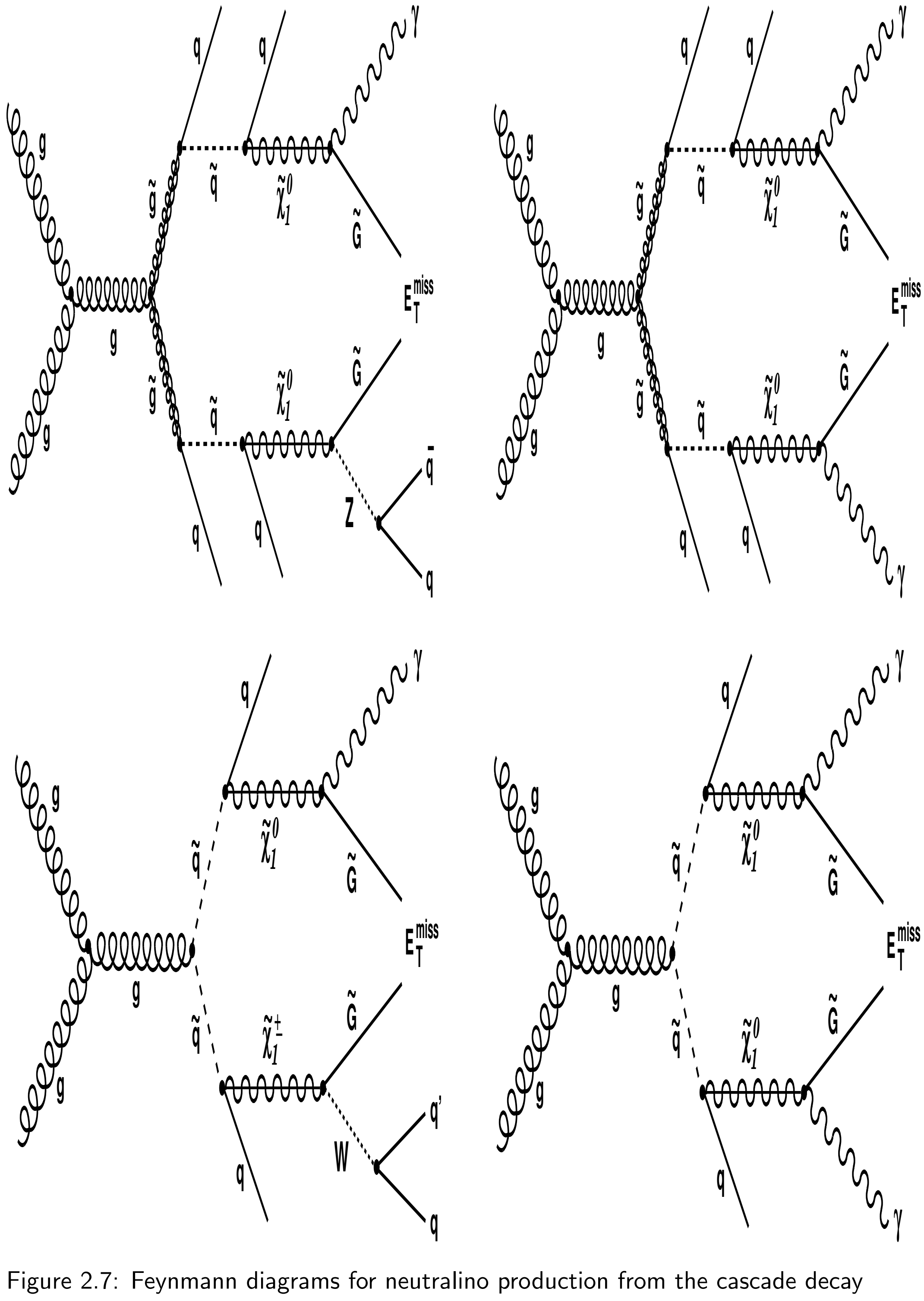

Figure 2.7: Feynmann diagrams for neutralino production from the cascade decay of a produced gluino (*top*) and squark (*bottom*). The final event has a single (*left diagrams*) or double photons (*right diagrams*) neutralino decay at LHC.

Since $\mathbf{\Lambda}$, determines the mass of gluino ($\widetilde{\mathrm{g}}$), squarks ($\widetilde{q}$) which decay to the $\widetilde{\chi}_1^0$. Therefore the momentum of $\widetilde{\chi}_1^0$ ($p_{\widetilde{\chi}_1^0}$) is determined by the masses of gluino and squarks. If the gluino or squark decays to the neutralino in association with a many gluons and quarks seen in the detector as *jets*, then the neutralino momentum is small with the ratio $p_{\widetilde{\chi}_1^0}/m_{\widetilde{\chi}_1^0} \ll 1$. This means the $\widetilde{\chi}_1^0$ produced with low boost or moving slow and therefore and the photon from its decay arrives late at the detector compared to proton-proton collision times. However, if the gluino or squark decays with less number of jets, then the $\widetilde{\chi}_1^0$ momentum is not small and it is produced with significant boost such that its decay happens outside the detector volume.
The other factor is the inherent long lifetime, $c\tau_{\widetilde{\chi}_1^0}$, of the $\widetilde{\chi}_1^0$. Lightest neutralinos with significantly large values of $c\tau_{\widetilde{\chi}_1^0}$, would travel some finite distance in the detector before decay, and the resulting photon would arrive late at the detector. On the other hand, if $c\tau_{\widetilde{\chi}_1^0}$ is very small, as in the case when the parameter, C_{grav} takes the value 1, the $\widetilde{\chi}_1^0$ decay is prompt and the photon is not longer late.

2.3.2 Signal Modeling

We produced simulated high-energy-physics signal events according to the SPS8 benchmark model using general-purpose event generators based on Monte Carlo (MC) methods of numerical computations. The process of event generation starts with the production of *SUSY Les Houches Accord* (SLHA) files using a SUSY software package called ISASUSY[20]. These SLHA files contain the masses, interaction couplings, decay widths and all possible decay channels and their Branching Ratio (BR) of every supersymmetric particles. Each file also contain the value of the fundamental GMSB model parameters;

$$\Big\{\mathbf{\Lambda}, \mathbf{M}_{\mathrm{mess}}, \mathbf{N}_5, \tan(\beta), sgn(\mu), C_{grav}\Big\} \tag{2.18}$$

spanning all the possible, in terms of particle kinematics, supersymmetric particle production and decay configurations or phase space, as defined by the model, in the production of events. In the SPS8 model, the choice of parameters is such that

$$sgn(\mu) = 1, \tan(\beta) = 15, \mathbf{N}_5 = 1, \mathbf{M}_{\mathrm{mess}} = 2\mathbf{\Lambda}, \tag{2.19}$$

where C_{grav} and $\mathbf{\Lambda}$ are not fixed . By varying, respectively, C_{grav} and $\mathbf{\Lambda}$, we can exploit different decay scenarios where the $\widetilde{\chi}_1^0$ has a different lifetime and mass. For a specific choice of C_{grav} and $\mathbf{\Lambda}$, we produce a signal sample where the events have a mean lifetime ($c\tau$) and mass of the $\widetilde{\chi}_1^0$. A special software package called HDECAY, is used to handle the decay of all supersymmetric particles including the $\widetilde{\chi}_1^0$.
The signal events are generated according to the processes described by the Feynmann diagrams in Figure 2.7 using particle generators based on Monte Carlo simulations. The produced $\widetilde{\chi}_1^0$ cascade decay of the gluino/squarks;

$$p + p \rightarrow \widetilde{\mathrm{g}}\widetilde{\mathrm{g}}, \widetilde{q}\widetilde{q} \rightarrow [\text{1 or 2 cascade decays}] \rightarrow 2\widetilde{\chi}_1^0 + \text{jets} \rightarrow 2\gamma + 2\tilde{G} + \text{jets}, \tag{2.20}$$

is allowed to decay to either γ, Z bosons, H, e^+e^-, and the $\tilde{G}$. However, its decay to a γ and $\tilde{G}$ is the dominant mode of decay with a branching fraction for single photon decay channel, $\widetilde{\chi}_1^0 \rightarrow \gamma + \tilde{G}$, about 83 to 94%. We observed that 97 to 99% of all our simulated signal events contain at least a single photon. We use PYTHIA-6 [21] as the MC event generator. It takes as input an SLHA file and generates events of supersymetric particles, produced at the LHC pp collider with center of mass energy, $\sqrt{S} = 8\,\text{TeV}$. The interaction of these supersymmetric particles with the CMS detector is simulated using the GEANT4 [22], particle detector simulation software. A full physics event is reconstructed from energy deposits (hits) in the CMS detector using the CMS event reconstruction Software (CMSSW). To minimize any disagreement between MC and data, we use the same CMSSW release version (**CMSSW_5_3_29**) in the MC event reconstruction with the same detector conditions as the recorded data.

We perform some sanity checks that the signal samples have been correctly generated by PYTHIA-6, by looking at the number of photons, $E_{\mathrm{T}}^{\mathrm{miss}}$ and number of jets in each signal event. We also measured the mean lifetime of the $\widetilde{\chi}_1^0$ by fitting the distribution of the $\widetilde{\chi}_1^0$ lifetime computed from its transverse distance traveled before decay. This distance is computed using its production and decay vertices. Comparing the mean lifetime,$c\tau$, obtained from the fit, to its theory value supposedly used in the event generation, we are able to check that each signal sample has been properly generated.
We also observed that most of the events had at least a single photon (left plot) and

at least 2 jets (right plot) shown in the top plots of Figure 2.9. Comparing different signal samples with $c\tau = 2000\,\text{mm}, 4000\,\text{mm}, 6000\,\text{mm}$ of $\Lambda = 180\,\text{TeV}$ and a $\gamma+$ jet with $120 < \hat{p_{\text{T}}} < 170\,\text{GeV}/c$ sample, we observed that the $E_{\text{T}}^{\text{miss}}$ (shown in the bottom plot of the same figure) from signal events was larger than the $E_{\text{T}}^{\text{miss}}$ of events from the $\gamma+$ jet sample agreeing with our expectation that the $\gamma+$ jet sample has mostly fake $E_{\text{T}}^{\text{miss}}$ while signal samples have large $E_{\text{T}}^{\text{miss}}$ due to the $\widetilde{\chi}_1^0$ decay to gravitino.

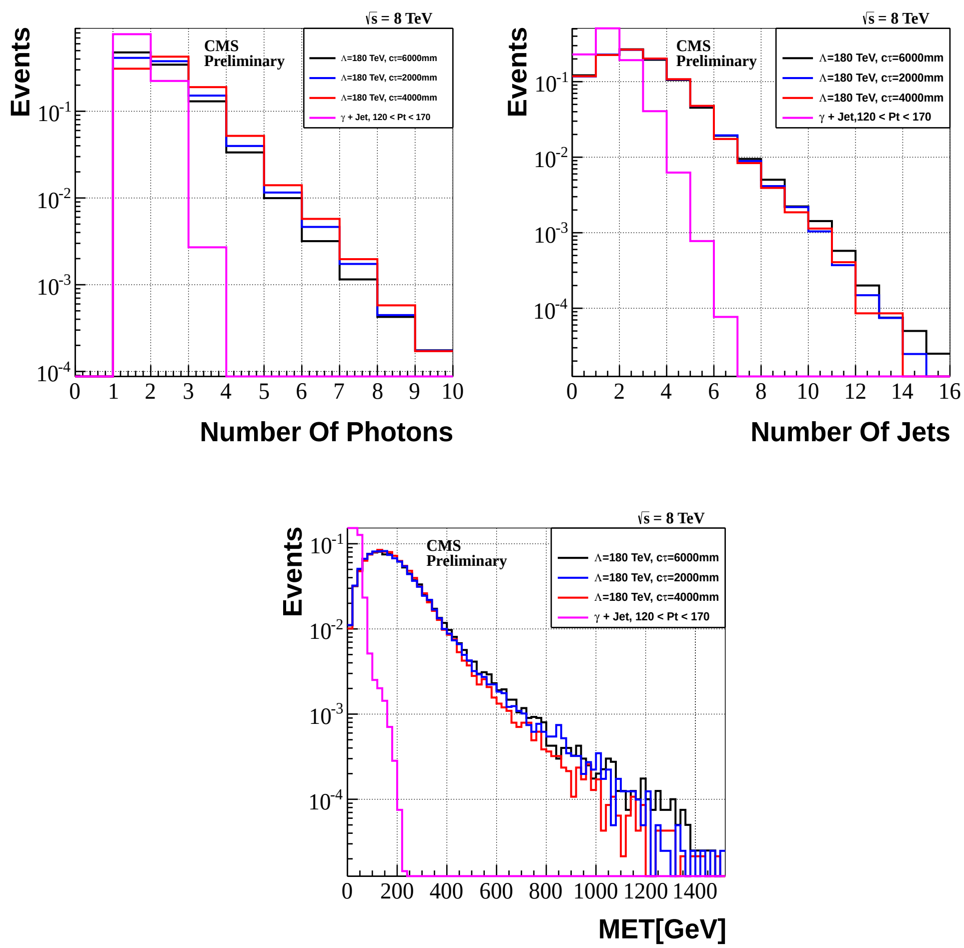

Figure 2.8: Number of photons (top left), Number of jets (top right) and $E_{\text{T}}^{\text{miss}}$ (bottom) for events with $\widetilde{\chi}_1^0$ decay to γ and $\tilde{G}$ for different $c\tau = 2000\,\text{mm}, 4000\,\text{mm}, 6000\,\text{mm}$ points of $\Lambda = 180$ TeV of the SPS8 model. A $\gamma+$jet with $120 < \hat{p_{\text{T}}} < 170\,\text{GeV}/c$ sample shown for comparison with the signal samples.

2.3.3 Lightest Neutralino's Lifetime

The distance traveled, in the CMS detector, by the $\widetilde{\chi}_1^0$ before it decays, mentioned previously section 2.3.1, is given as

$$\mathrm{L} = \left(c\tau_{\widetilde{\chi}_1^0}\right) \cdot (\gamma\beta) = \left(c\tau_{\widetilde{\chi}_1^0}\right) \cdot \left(\frac{p}{m_{\widetilde{\chi}_1^0}}\right). \tag{2.21}$$

This distance depends on the momentum (p) and mean lifetime ($c\tau_{\widetilde{\chi}_1^0}$) of the $\widetilde{\chi}_1^0$. Large values of $c\tau_{\widetilde{\chi}_1^0}$ means, this distance is large and if larger than the ECAL radius, can be interpreted as the $\widetilde{\chi}_1^0$ traveled outside the ECAL volume before it decayed, making detecting the delayed photon no longer possible. On the other hand, small values of $c\tau_{\widetilde{\chi}_1^0} < 10\,\mathrm{cm}$ means the $\widetilde{\chi}_1^0$ decayed early and the photon is not late enough such that its detection using ECAL time measurements alone is not reliable. High-p values means the $\widetilde{\chi}_1^0$ is boosted and could travel out of the ECAL before it decay, making the photon again undetectable. On the other hand, low-p values means the $\widetilde{\chi}_1^0$ is less boosted and traveling slow enough for its decay to happen inside the ECAL volume and the photon delayed arriving at ECAL. In Figure 2.9, we show a distribution of the momentum of the $\widetilde{\chi}_1^0$ in the transverse ($x - y$) plane (transverse momentum ($p_{\mathrm{T}}^{\widetilde{\chi}_1^0}$)), the $\widetilde{\chi}_1^0$ transverse distance traveled before it decay, the transverse momentum of the photon (p_{T}^{γ}) and photon's estimated time (T_γ) using only generator level information. These distributions are for different Λ and $c\tau_{\widetilde{\chi}_1^0}$ points of the SPS8 model. We observed that, the $p_{\mathrm{T}}^{\widetilde{\chi}_1^0}$ increases with increase values of Λ, from $\Lambda = 100\,\mathrm{TeV}$ to $220\,\mathrm{TeV}$, which agrees with our expectation. As Λ increases along with the masses of the gluino/squark and $\widetilde{\chi}_1^0$, the $p_{\mathrm{T}}^{\widetilde{\chi}_1^0}$ also increases since a massive gluino/squark decay into the $\widetilde{\chi}_1^0$. In the same way, increasing the mass of $\widetilde{\chi}_1^0$ ($m_{\widetilde{\chi}_1^0}$) through increasing Λ, leads to increase in the photon p_{T}. For a given value of $\Lambda = 180\,\mathrm{TeV}$, which means $p_{\mathrm{T}}^{\widetilde{\chi}_1^0}$ is fixed, the transverse distance traveled by the $\widetilde{\chi}_1^0$ before decay (shown in the top right plot of Figure 2.9) and photon time (shown in the bottom right plot of the same figure) increased with increasing value of $\widetilde{\chi}_1^0$ mean lifetime, $c\tau = 50\,\mathrm{cm}$ to $600\,\mathrm{cm}$ in the same way, qualitatively. These observations support our expectation that the photon is delayed primarily because of the long lifetime of the $\widetilde{\chi}_1^0$. However, one can argue that this is not entirely true and we will exploit this further in a detailed study of the source of delayed photons in the next section.

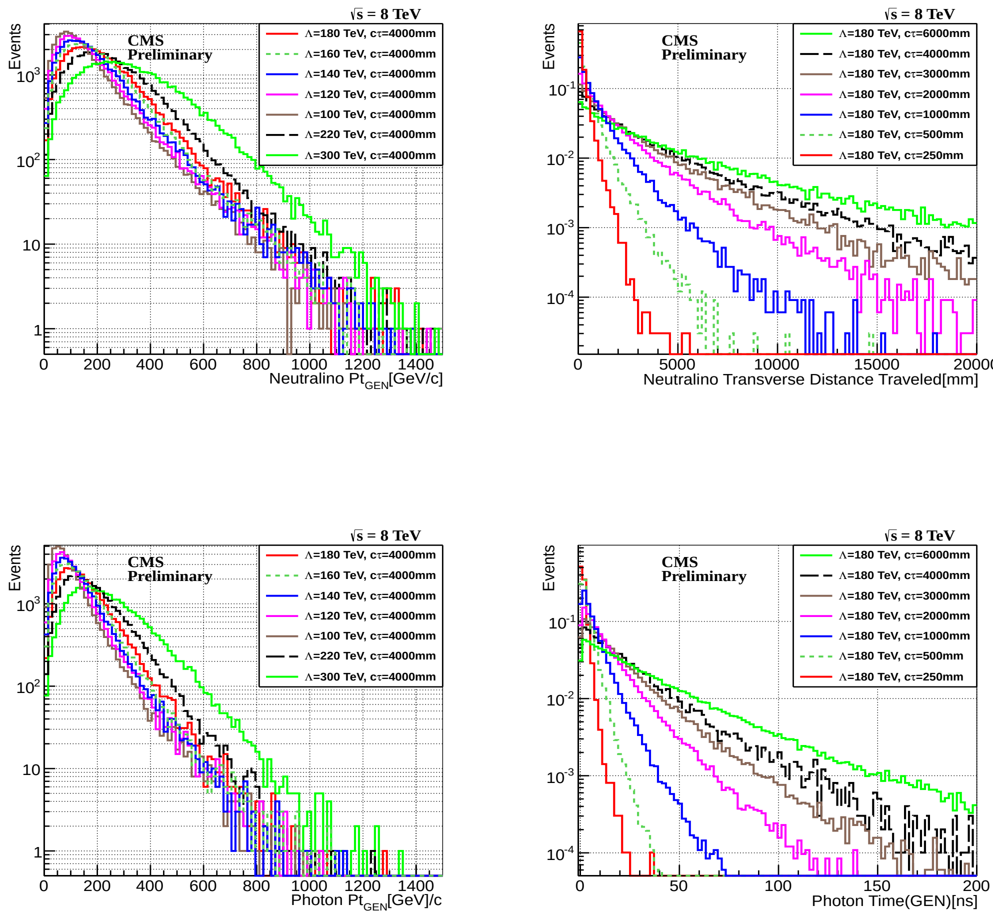

Figure 2.9: Neutralino transverse momentum ($p_{\mathrm{T}}^{\widetilde{\chi}_1^0}$) distribution (top left) and transverse distance traveled (top right). Transverse momentum (bottom left) and time (bottom right) of photon from neutralino decay for different Λ and $c\tau$ points in GMSB SPS8 model.

The photon from the decay of $\widetilde{\chi}_1^0$ can arrive late at ECAL for either one of the following reasons: first, because the $\widetilde{\chi}_1^0$ is traveling slow i.e. with boost, $\beta = \frac{p_{\widetilde{\chi}_1^0}}{m_{\widetilde{\chi}_1^0}} << 1$, and second, because the $\widetilde{\chi}_1^0$ was produced with significant boost such that the photon traveled to ECAL through a non-direct flight path from the nominal pp interaction point. We distinguish between these two sources of delayed photons by estimating the photon arrival time at ECAL in each scenario using the distance traveled by $\widetilde{\chi}_1^0$ before decay and the distance traveled by the photon from the decay point to the point of detection at ECAL. Figure 2.10 (left) is a schematic representation showing how we estimate the photon arrival time at ECAL in each of the possible travel flight path representing the different source of delayed photons. The estimated photon arrival ECAL time in each scenario is given as follows:

- For slow moving neutralinos: Δt_1 = (L1/cβ) - (L1/c)
- For non-direct traveled flight path: Δt_2 = (L1 + L2 - L3)/c
- ECAL measured time = $\Delta t_1 + \Delta t_2$

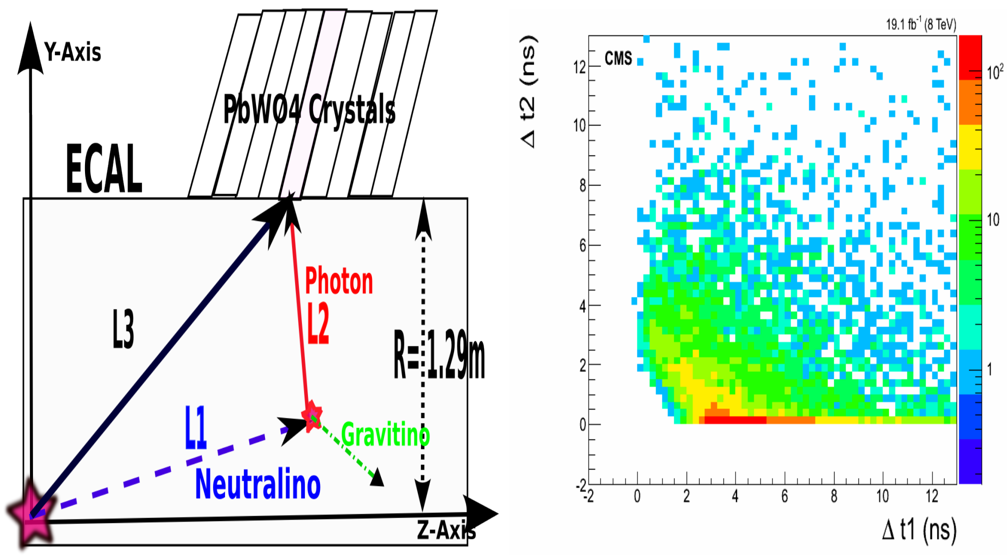

Figure 2.10: Schematic diagram showing $\tilde{\chi}_1^0 \rightarrow \gamma + \tilde{G}$ decay topology within the ECAL volume of the CMS detector (*Left*). The estimated photon arrival time at ECAL from the decay of $\tilde{\chi}_1^0$ in the SPS8 model with $m_{\tilde{\chi}_1^0} = 256\,\mathrm{GeV}/c^2$ and $c\tau = 600\,\mathrm{cm}$ (*Right*).

The $\tilde{\chi}_1^0$ is traveling with velocity, $v = c\beta$, where c is the speed of light in vacuum. The distribution of the estimated photon ECAL arrival times Δt_1 and Δt_2, is plotted shown in Figure 2.10(right), where the color intensity represents the photon population. We observed that most of the late arrival time photons are from the decay of slow moving $\tilde{\chi}_1^0$ compared to those from non-direct flight path to ECAL. This proves that a good number of $\tilde{\chi}_1^0$ produced with low momentum such that the ratio $\frac{p_{\tilde{\chi}_1^0}}{m_{\tilde{\chi}_1^0}} << 1$ produced most of our detectable delayed photons, using ECAL time measurements. While $\widetilde{\chi}_1^0$ with very long lifetimes ($c\tau$) produced with high momentum will very likely escape the ECAL without detection unless their decay happens within the ECAL volume such that the delayed photon arrives at the ECAL in a non-direct flight path.

2.4 Previous Search Experiments

The have been other search experiments for LLNPs decaying to photons and missing transverse energy. The results have been interprested int the context of the SPS8 benchmark models and other GMSB models. The results from DO, CDF, CMS and ATLAS,[23, 24, 25, 26, 27] experiments on the search for $\widetilde{\chi}_1^0$ as the NLSP decaying to photon and gravitino are shown in Figure 2.11. These results show that within the SPS8 model, $\widetilde{\chi}_1^0$ s with mass $m_{\widetilde{\chi}_1^0} \leq 245$ GeV and mean lifetime, $c\tau_{\widetilde{\chi}_1^0} \leq 6000\,\mathrm{mm}$ are excluded at hadron colliders, based on the particle signal and background definitions used in these experiments. The plot on the left of Figure 2.11 are exclusion results with the mass of $\widetilde{\chi}_1^0$ or effective SUSY breaking scale $\mathbf{\Lambda}$ on the horizontal x-axis and the $\widetilde{\chi}_1^0$ lifetime, $c\tau_{\widetilde{\chi}_1^0}$ on the vertical y-axis from data recorded by the ATLAS experiment at pp with center of mass, $\sqrt{S} = 7\,\mathrm{TeV}$. The plot on the left is for CMS experiment, with the same pp collision energy. The shaded regions are the excluded regions where the search results came out negative. We will discuss in detail these results in Chapter 8 when we compare our results to these results.

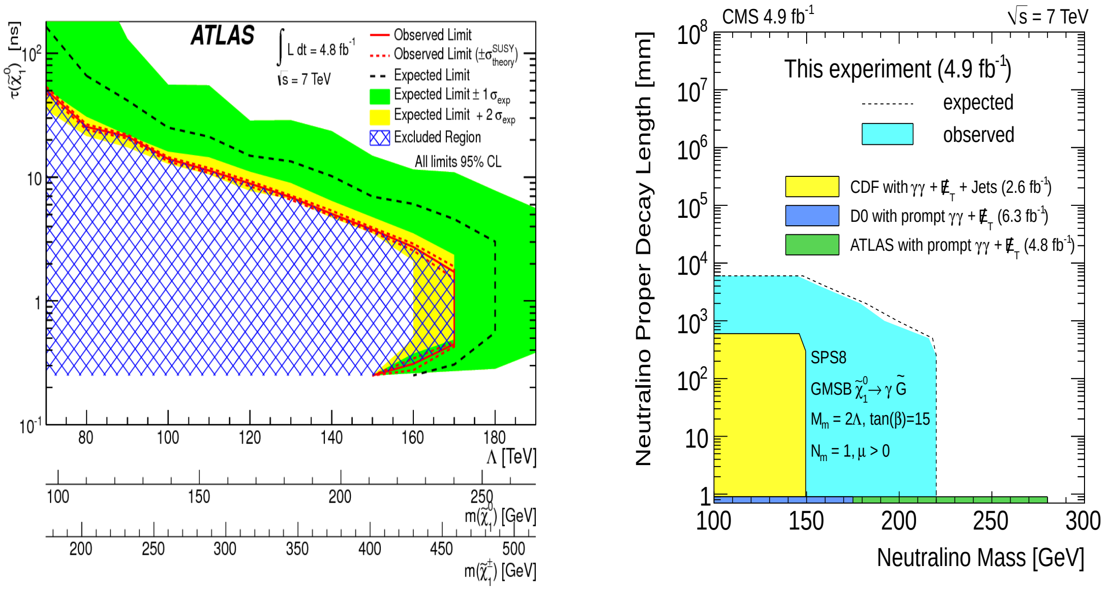

Figure 2.11: Neutralino lifetime and mass upper limit from ATLAS(left) and CMS(right) 7 TeV analysis with non-pointing photons and MET.

Chapter 3

Hadron Collider and Detector

The Large Hadron Collider (LHC) is a circular particle accelerator at CERN, accelerating two beams of either protons or ions through a circular ring in opposite directions and eventually colliding them at a collision point. Located at one of these collision points, is a general purpose multi-particle detector called the Compact Muon Solenoid (CMS). A detailed description of the LHC and CMS detector can be found in [28] and [29, 30].

3.1 Large Hadron Collider

3.1.1 Overview

The LHC accelerates and collides proton and heavy ion beams with a center of mass energy, $\sqrt{S}$, of 14 TeV. It is located across the border between France and Switzerland and hosted by the European Organization for Nuclear Research (CERN). The LHC uses powerful superconducting magnets to control and maintain the circulation of the beams in its circular ring of nearly 27 km in circumference. The circulating beams gain energy as they are transferred from the Booster and eventually into the LHC synchrotron where at 7 TeV they are steered by focusing magnets to a head-on collision against each other at a collision point. Figure 3.1 shows the LHC and the different stages of proton beam acceleration prior to collision.

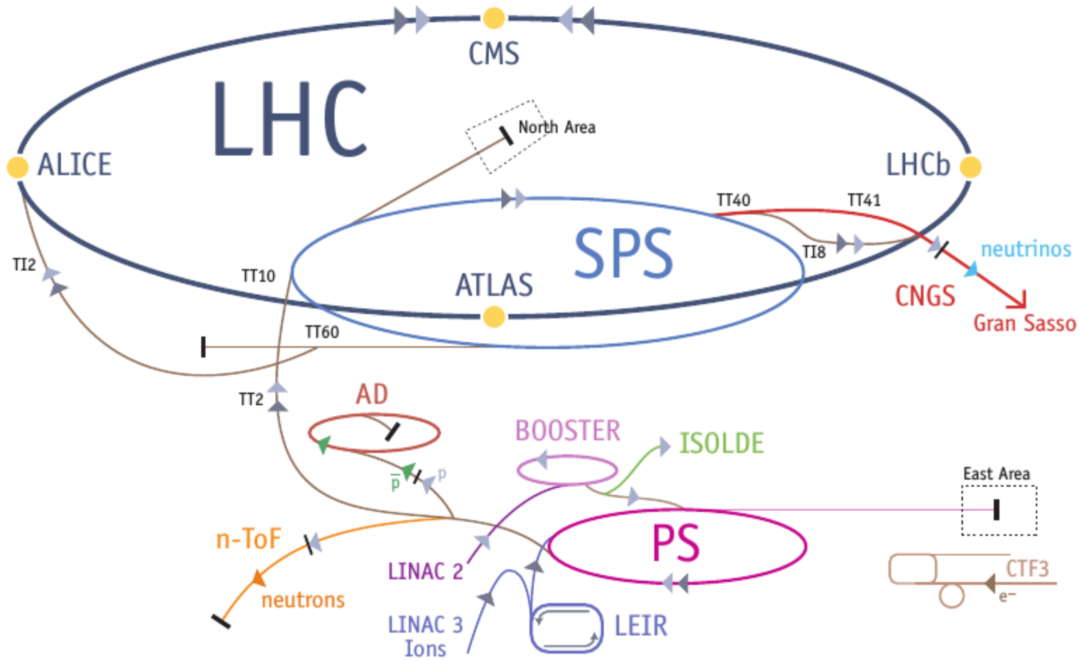

Figure 3.1: Schematic diagram showing the full Large hadron Collider.

3.1.2 Colliding Energy

Protons which are hydrogen ions from hydrogen gas where the orbiting electron has been striped away are inserted into a linear accelerator called LINAC 2. Using the electromagnetic fields in Radio Frequency (RF) cavities, these protons are accelerated to an energy of 50 MeV creating a stream of particles called *proton beams* which are arranged in packets known as *bunches*. The proton beams from the LINAC 2 are injected into the circular *Proton Synchrotron Booster* (PSB) where they gain acceleration as the pass many times through the RF cavities with their energy increasing after each pass. The PSB accelerates the protons up to 1.4 GeV and injects them into the *Proton Synchrotron* (PS) which increases their energy to 25 GeV. These protons, traveling at 99.93% the speed of light at this stage, are sent to the *Super Proton Synchrotron* (SPS) and further accelerated to an energy of 450 GeV. The 450 GeV protons are finally transferred into the LHC ring (split into two beams accelerating in a clockwise and anti-clockwise direction) where they are accelerated for about 20 minutes to their nominal energy of 7 TeV. By now the protons are traveling with the speed of 99.9999% the speed of light and powerful bending magnets are used to keep the beams traveling in the circular LHC ring.

In a circular particle collider like the LHC, the energy available to make new particles, which is the *center of mass* (COM) energy, denoted by $\sqrt{S}$, is simply the sum of the energy of the two beams i.e. $\sqrt{S} = E_{\text{beam1}} + E_{\text{beam2}}$. This is larger than that for fixed target colliders which is $\sqrt{E_{\text{beam}}}$, and makes circular colliders favorable for producing new particles with high enough mass. For example, in the LHC, each beam is designed to have an energy of 7 TeV making $\sqrt{S} = 14\,\text{TeV}$.

3.1.3 Luminosity

In colliding beam experiments, the center of mass energy available for producing a new phenomenon is very important. However, the number of useful interactions producing the new phenomenon (event) is equally important, especially in cases where the probability (or cross section) of producing events from a rare phenomenon or physics process is very small. The *Luminosity* ($\mathscr{L}$) of the colliding beams measures the potential of a particle accelerator to produce events from a required number of interactions and serves as the proportionality factor between the number of events per second and the cross section. The luminosity can be defined as a measure of the number of collisions that can be produced in a collider per squared area per second. It depends on factors ranging from the flux i.e. number of particles per second of the beams, the size of the beam at collision and the frequency of collision. For physics experiments, the integrated luminosity which is the total luminosity over a given period of time, usually a year, gives the amount of data that has been recorded by a given detector and represents events produced from many different physics processes. From the measured luminosity ($\mathscr{L}$) and the predicted cross section (σ_p) of a given physics process, we can estimate the number of events per second (event rate (R)) we expect to be produced in pp collisions as

$$\mathsf{R} = \mathscr{L} \cdot \sigma_p. \tag{3.1}$$

However, in measurement experiments, the observed number of events (N) and the measured integrated luminosity can be used to measure the cross section (σ) of a physics process using the relation

$$\sigma = \frac{N}{\mathscr{A} \times \epsilon \times \mathscr{L}}, \tag{3.2}$$

where ϵ, and $\mathscr{A}$, are the efficiency and acceptance in counting the observed number of events, respectively. This measured cross section can be compared to predictions of a model.

The LHC was designed to collide proton beams with a peak instantaneous luminosity of $1 \times 10^{34}\,\mathrm{cm}^{-2}s^{-1}$ and the total integrated luminosity measured by the CMS detector is separated into the "recorded" and "delivered" integrated luminosity. Delivered luminosity refers to the luminosity delivered by LHC to CMS and one would expect this to be equal to the amount recorded. However, there are instances when the CMS detector is unable to record data either because CMS Trigger and Data Acquisition System (TriDAS) is down or one of the CMS sub-detectors is temporarily being repaired. Figure 3.2 shows a monthly total integrated luminosity delivered by LHC and recorded using the CMS detector during the 8 TeV pp collision.

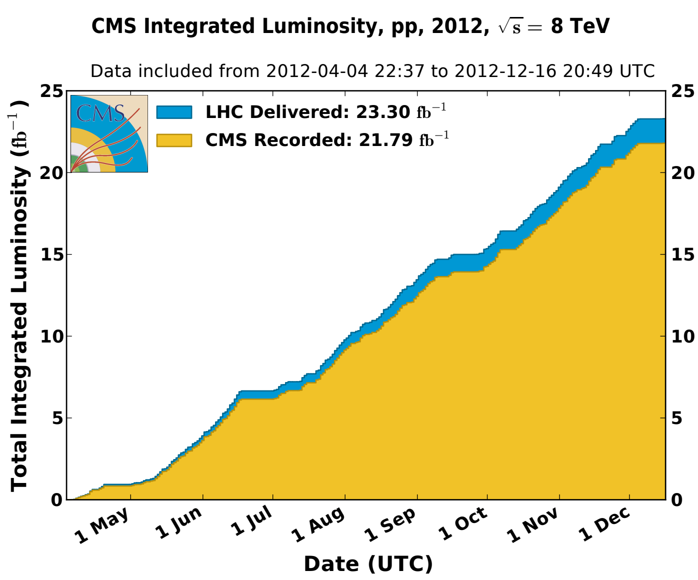

Figure 3.2: Cumulative luminosity versus month delivered to (blue), and recorded by CMS (orange) during stable beams of for pp collisions at $\sqrt{S} = 8$ TeV in 2012.

3.1.4 LHC Bunch Structure

Of the 3564 *bunch* places in an LHC orbit, only 2808 bunch places are occupied with protons. Each proton bunch has been placed inside an RF bucket during the proton beam filling process. The filling scheme is organized such that not all the RF buckets have protons. The empty buckets or beam gaps are necessary to avoid parasitic collisions near the collision point and to make room for beam halo removal and beam dump during beam cleaning, prior to and after collision. Each RF bucket, filled or empty, is separated in time from the next one by approximately 2.5 ns and carries about 10^{11} protons. During the filling in LINAC 2 and the splitting into proton bunches with each bunch occupying an RF bucket in the PS, it is possible that some empty RF buckets are also filled although they carry a much smaller proton population compared to the main proton bunch. These bunches carrying few protons can either be trailing the main proton bunch by a time of Δt = 2.5, 5.0, 7.5, ... ns, or leading the main proton bunch by Δt = -2.5, -5.0, -7.5, ... ns. If the bunch is 2.5 to 3.0 ns separated in time from the main proton bunch or another, it is called a *satellite* bunch and if the separation is about 5.0 ns, it is referred to as an *ghost* bunch. In Figure 3.3, we present a longitudinal profile of a typical LHC orbit showing the ghost, satellite and main proton bunches [31].

The presence of ghost/satellite bunches increase the uncertainty in LHC luminosity measurements and can also generate *pp* interactions near the collision point. Effects from ghost/satellite bunches on instantaneous luminosity measurements and recorded events have been studied by CMS, ATLAS and ALICE experiments. The results, seen in Figure 3.4, show a clear presence of events produced from ghost and satellite bunch collisions. CMS used the energy deposits in the endcap calorimeters to observe time spaced clusters which are consistent with expectations from ghost/satellite bunches while ATLAS uses the Longitudinal Density Monitor (LDM) detector to study ghost/satellite bunches. The details of these studies can be found in [32, 33].

We summarize in Table 3.1, the LHC design and operation conditions during LHC RUN 1.

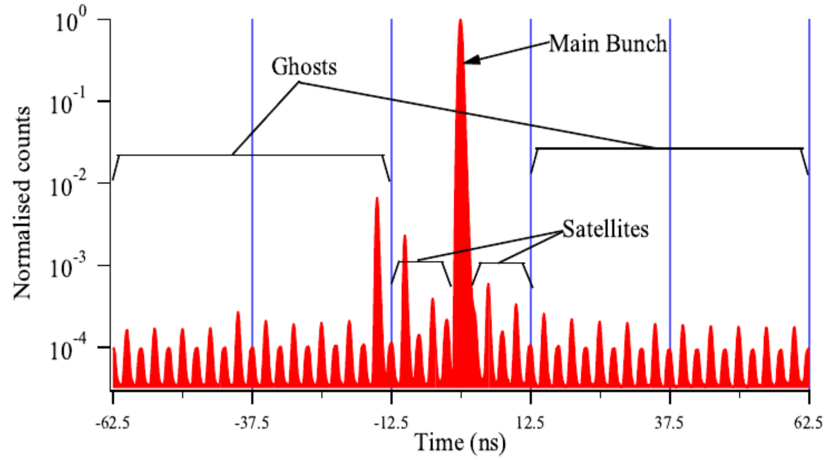

Figure 3.3: Longitudinal profile of a typical LHC proton beam taken with the Longitudinal Density Monitor (LDM) detector. Ghost/Satellite bunches and the main proton bunch shown.

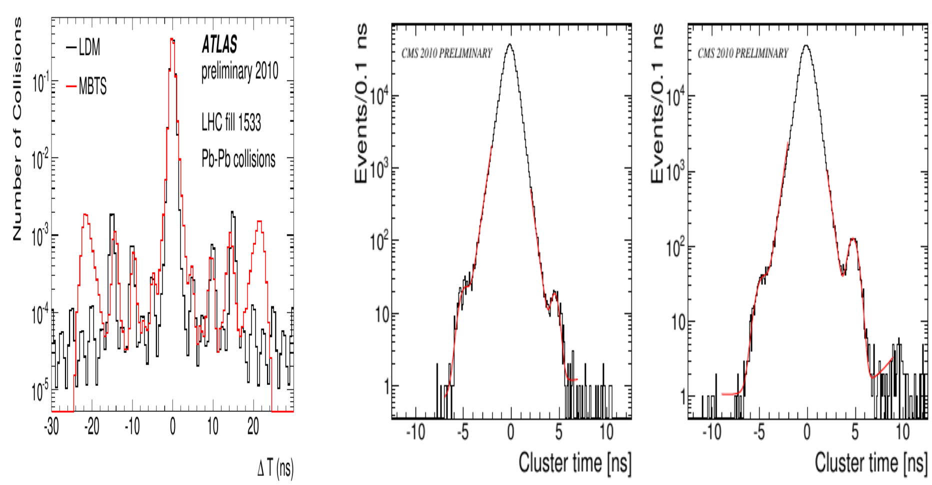

Figure 3.4: Left: Arrival time (red) of events in ATLAS for LHC fill 1533 during 2010 $PbPb$ collision and an LDM profile (black) for Beam2 (same for Beam1). Right: Cluster time in the CMS endcap calorimeters from fill 1089 of the positive endcap detector(left side of IP $z > 0$) (left) and negative endcap detector(right side of IP, $z < 0$) (right). Both plots show a clear presence of events from Ghost/Satellite bunches with the expected time separation.

LHC Operation Parameters 2010-2013

Parameter	2010 value	2011 Value	2012/13 Value	Design Value
Beam energy[Te]	3.5	3.5	4.0	7
β^* in IP 5[m]	3.5	1.0	0.6	0.55
Bunch spacing [ns]	150	75/50	50	25
Number of bunches	368	1380	1380	2808
Protons/bunch	1.2×10^{11}	1.45×10^{11}	1.7×10^{11}	1.15×10^{11}
Normalised emittance[mm.rad]	≈ 2.0	≈ 2.4	≈ 2.5	3.75
Peak luminosity[$cm^{-2}s^{-1}$]	2.1×10^{32}	3.7×10^{33}	3.7×10^{33}	1×10^{34}
Evts/bunch crossing	4	17	37	19
Stored Beam energy(MJ)	≈ 28	≈ 110	≈ 140	≈ 362
Int. Luminosity by CMS[pb^{-1}]				_
Circumference[km]	26.659	26.659	26.659	26.659
Dipole Magnet B[T]	8.33	8.33	8.33	8.33

Table 3.1: LHC operation parameter conditions during RUN 1, 2010-2013

3.2 Compact Muon Solenoid

3.2.1 Overview

The Compact Muon Solenoid (CMS) detector is located at Point 5 which is one of the *pp* collision points along the LHC ring. Its choice of design balances cost and robustness in the detection of many different particles. The detector has a simple cylindrical structure consisting of a barrel and two endcap detectors. It also has an extensive forward calorimetry detector providing an almost 4π solid angle coverage which assures good hermetic particle detection. The overall length of 21.6 m, a diameter of 14.6 m and weight of 12,500 tons define the size of the CMS detector. Figure 3.5 shows the CMS detector with its different sub-detectors and the type of material used in the construction.

The main feature of the CMS detector is the presence of a superconducting solenoid magnet of 6 m internal diameter. The magnet provides a strong magnetic field of 3.8 T which causes the bending of the tracks of charge particles as they travel across the detector. The particle's momentum is measured from the reconstructed track.

The magnetic field encloses an entirely silicon pixel and strip tracker detector which are used for vertex finding and reconstructing the tracks of charged particles, a lead-tungstate ($PbWO_4$) scintillating-crystal Electromagnetic Calorimeter (ECAL) and a brass and plastic scintillator sampling Hadron Calorimeter (HCAL). Very long lived particles like muons are detected using gas-ionization detectors embedded in the flux-return iron-yoke located at the outermost region of the detector called Muon Chambers.

The CMS experiment uses a coordinate system with the origin coinciding with the center of the detector where the *pp* or nominal collisions occur. This point is commonly referred to as the *interaction point* (IP). The directions of x, y, and z-axes are as shown in Figure 3.6. However, for particle identification, CMS uses a more convenient coordinate system based on the polar coordinates where the azimuthal angle, ϕ, is measured in the $x - y$ plane, with $\phi = 0$, being the x-axis and $\phi = \pi/2$, the y-axis. The radial distance in this plane is denoted R, and the polar angle θ, measured from the z-axis is related to *pseudo-rapidity*, η, through the relation: $\eta = -\ln\tan(\frac{\theta}{2})$. The coordinate system (η, ϕ), and its radial distance R, identifies a point in the cylindrical volume of the CMS detector. We will now describe the CMS subdetectors used in our analysis.

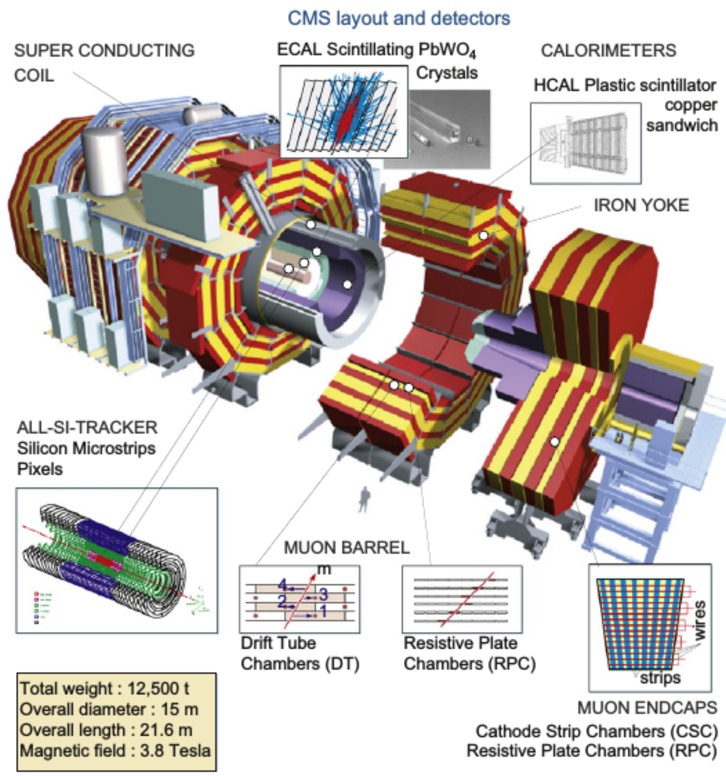

Figure 3.5: CMS Detector showing the different subdetectors and their material.

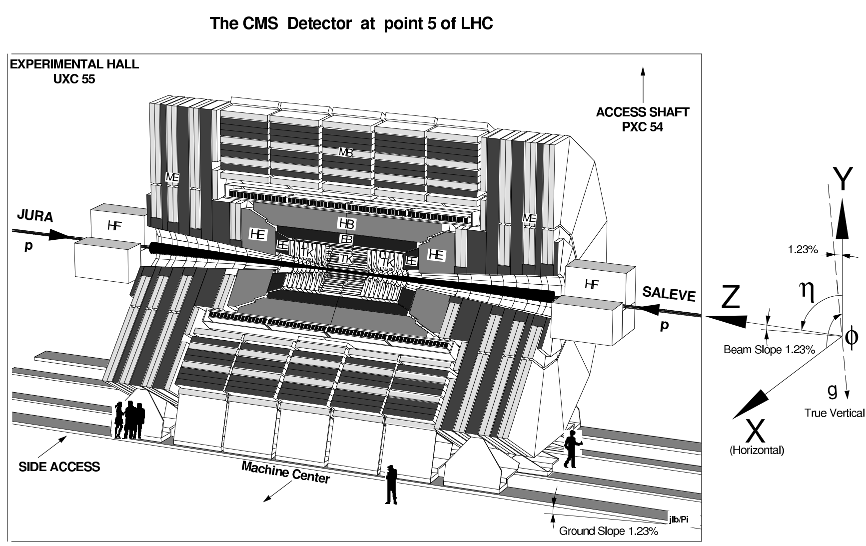

Figure 3.6: CMS detector schematic view with definition of $x - y - z$ coordinates.

3.2.2 Calorimeters

The calorimeter absorbs a good fraction of energy of an incident particle and produces a signal with an amplitude proportional to the absorbed energy. The energy absorption happens through the cascade production of secondary particles with the energy of the incident particle directly proportional to the number of secondary particles produced. The are two types of calorimetry choices used in the CMS detector: the *Electromagnetic Calorimeter* (ECAL) which is used for absorbing the energy of electromagnetic particles like photons and electrons and a *Hadronic Calorimeter* (HCAL) constructed with more than one type of material and is used for stopping and absorbing the energy of hadrons such as kaons and pions through strong interactions. The combined calorimeter subdetectors in CMS covers a region in $|\eta| < 5$, making it nearly hermetic which is needed for good missing transverse energy measurements. The ECAL and HCAL are arranged in a nested fashion shown in Figure 3.7 with the HCAL enclosing the ECAL so that electromagnetic particles can be distinguished from hadronic particles by comparing the depth of the particle shower penetration in both calorimeters.

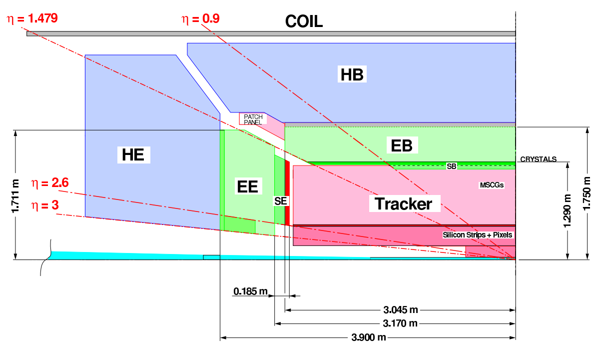

Figure 3.7: Schematic diagram of CMS calorimetry system with HCAL enclosing ECAL in the barrel and endcap regions.

Electromagnetic Calorimeter

The Electromagnetic Calorimeter (ECAL) detects photons and electrons through their interaction with the atoms of the lead tungstate ($PbWO_4$) crystals. During this interaction process which might happen through Coulomb scattering (electron-neutron scattering), Compton scattering (photon-electron scattering), photon emission (also known as *Bremsstrahlung*) and *electron-positron pair production*, the incoming photon or electron deposits practically almost all of its energy into the detecting medium. Electrons loss most of their energy, due to their small mass, through radiation (photon emission). High energy electrons and photons of several GeV deposit their energy to the $PbWO_4$ crystals through Bremsstrahlung and pair production processes producing electrons, positrons and photons in the process which subsequently produce more electrons, positrons and photons creating an avalanche of electrons, positrons and photons known as an *electromagnetic showers*. The process stops when the electron or photon energy becomes low. The probability of an electromagnetic particle with high energy to interact either through Bremsstrahlung or pair production with the detecting material is proportional to the nuclear charge, Z, of the material.

The choice of $PbWO_4$ crystals as the calorimetry material by CMS for operation in the LHC environment is because of the following reasons: $PbWO_4$ crystal is a high Z material with a density of 8.28 g/cm^3), has a short radiation length (X_0=0.89 cm) and a small Molière radius (22 cm). The dense nature of the $PbWO_4$ crystals allow for the electromagnetic shower to develop early and therefore likely to be fully contained within a compact detector like CMS. The short radiation length ensures that on average about 95 % of the electromagnetic shower energy produced by the photon or electron is contained within a crystal volume of about 9 crystals while the small Molière radius reduces the transverse spread of the electromagnetic cascade from multiple scattering of electrons and helps improve the estimation of the transverse position of impact of an incident particle. The arrangement of the $PbWO_4$ crystals also provide a fine granularity for measuring the particle's energy by providing fewer overlap of particle signals.
$PbWO_4$ crystal is also preferred to other crystal materials because of its high radiation resistance and fast scintillation decay time which is comparable to the LHC bunch crossing interval of 25 ns required for the high radiation dose and fast timing (25 ns proton bunch spacing) LHC environment. About 80% of the energy absorbed by the $PbWO_4$ crystal is emitted as light in less than 25 ns.

The ECAL has 75848 $PbWO_4$ crystals in total mounted in a cylindrical geometry, with a barrel (EB) and an endcap (EE) structure.
The EB region of the ECAL covers a pseudo-rapidity of $|\eta| < 1.479$. It has 61,200 crystals providing a granularity of 360 degree fold in ϕ and (2×85)-fold in η. The crystals are mounted in a quasi-projective geometry so that their axes make an angle of

3% with respect to a line vector from the nominal interaction vertex in η and ϕ directions. This is to avoid loss of energy into cracks aligned with a particle's trajectory. A crystal in EB is approximately 0.0174×0.0174 in (η, ϕ), $22 \times 22\,\mathrm{mm}^2$ at its front face and $26 \times 26\,\mathrm{mm}^2$ at its rear face. Each crystal is 230 mm long corresponding to about 25.8 X_0 radiation lengths. The crystal's radial distance measuring from the center of the face of the crystal to the beam line is 1.29 m. A number of crystals are placed in a thin-walled alveolar structure made with aluminum forming a *submodule*. Each submodule is arranged into 4 modules of different types according to their η position. There are about 400 to 500 crystals in each module and these 4 combined make one *supermodule* containing 1700 crystals.To reduce crystal reflective lost, the aluminum surface is coated to avoid oxidation leading to coloration. On the rear end of each EB crystal, two *Avalanche Photodiodes* (APD) is glued to collect the scintillating light from the crystals converting light into charge current which is further collected by the read-out electronics. The EE region covers a pseudo-rapidity region of $1.479 < |\eta| < 3.0$ with a *Preshower* (ES) detector made of silicon strip sensors interleaved with lead placed immediately in front of it. The purpose of the preshower is to identify photons from the decay of neutral pion, $\pi^0 \rightarrow \gamma\gamma$, and also to help separate photons producing electrons through pair production from photons not producing electrons before their arrival at the EE. The endcap located on the $+z$ side of the nominal interaction is denoted EE+ while the other located on the $-z$ side is denoted as EE−. The longitudinal distance between the IP and the center of the surface of the EE crystal is 3.154 m. Each endcap is divided into two halves called *Dees* with each Dee holding 3662 crystals. Crystals in EE with identical shape are grouped into 5×5 mechanical units called *supercrystals* (SC). The crystals in the SC form an $x - y$ grid. Each crystal is 220 mm (24.7 X_o) in length and has a front and rear face cross sections of $28.62 \times 28.62\,\mathrm{mm}^2$ and $30 \times 30\,\mathrm{mm}^2$, respectively. A *Vacuum Phototriode* (VPT) instead of an APD is glued on the rear face of each crystal for receiving and converting the scintillating light into electrical signals. The VPT is used in the EE because of its high resistance to radiation and smooth operation in a strong magnetic field environment. CMS uses APDs and VPTs because they are not affected by the high magnetic field and they have a high gain relative to regular photodiodes which have no gain. Although the light yield for $PbWO_4$ crystals is rather low ($\approx$ 70 photons/ MeV), these photo-detectors have internal gain (50 for

APDs and 10 for VPTs) and quantum efficiency of 75 % for APDs and 20 % for VPTs of the emission wavelength which makes it possible for detecting signals from incident particles with energies of a few to high GeV. The signals from the APDs and VPTs are amplified and digitized by voltage-sensitive analogue-to-digital converters and transported through optical fibres as light signals to the underground counting room which is located adjacent to the CMS experimental cavern.

The energy resolution and geometry structure of the ECAL ensures that the photon or electron's energy, arrival time, position and even the direction through the shape of its electromagnetic shower in the crystals is measured with good precision.

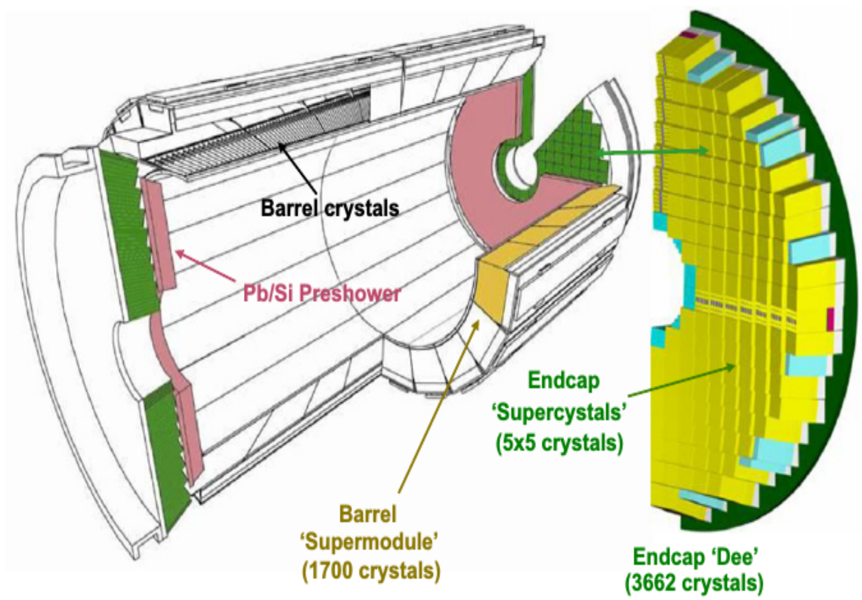

Figure 3.8: Layout of the CMS electromagnetic calorimeter showing the arrangement of crystal modules, supermodules in the barrel with the preshower infront of endcap with supercrystals.

ECAL Readout Electronics

The ECAL readout electronics is divided into an On-Detector or Front End (FE) board and an Off-Detector (OD) electronics. The FE board is installed inside the detector volume behind the crystals and infront of the hadron calorimeter and is made with radiation-hard electronics to withstand the high radiation dose. Data from the FE is transferred by radiation hard fibres to the OD electronics which is in the underground service cavern located approximately 80 m from the CMS detector.

A Clock and Control Unit (CCU) chip on each FE board communicates through bi-directional optical links with the Clock and Control System (CCS) board of the OD. These links carry clock and control signals and the trigger Level 1 accept (L1A) signal from the Timing, Trigger and Control (TTC) board and the Trigger Control System (TCS). A voltage controlled Quartz Phase-Lock Loop (QPLL) time jitter-filter and clock multiplier chip with an output clock jitter of 16 ps rms ensures that the LHC clock signal is transmitted to both the FE and OD electronics for synchronization.

Each FE board, shown in Figure 3.9, receives signals from a group of crystals typically forming a 5×5 crystal matrix and hosts five Very Front End (VFE) boards with each VFE board holding five analog channels. Each channel, shown in Figure 3.10, is carrying the signal from a single crystal and consists of a Multi-Gain Pre-Amplifier (MGPA) and three identical 12 bit Analog-to-Digital Converters (ADC), which are used to amplify, shape and digitize the signal coming from the Photo-Diode.

The MGPA chip has 3 gain ranges with gain ratios of 1, 6 and 12 to span the overall dynamic range of the signal which can go from 12 MeV up to 1.7 TeV. Equipped with a Capacitor-Resistor-Resistor-Capacitor (CR-RC) filter with a pulse shaping time of 40 ns and less than 1% of non-linearity, the MGPA ensures a uniform pulse shape matching and linearity across all 3 gain ranges allowing for precise pulse shape reconstruction.

The required readout and precision performance of the FE electronics demands a 12-bit ADC chip with a sampling frequency of 40 MHz to digitize the analog pulse signal of the highest unsaturated range into 10 discrete samples with an electronic noise of about 40 MeV. The FE card stores the digitized crystal data (ten 40 MHz discrete samples per channel) in 256-word-deep memories called *pipelines*. Five such pipelines and the logic to calculated the energy sum of 5 crystals once every LHC proton bunch crossing is integrated into a 0.25 μm technology FERNIX ASIC chip. Each VFE card is serviced by one such chip allowing for the energy to be summed in strips of 5 crystals along ϕ. In EE the five strip energy sums are transmitted to the Trigger Concentration Card (TCC) on the OD electronics, while for EB, a sixth chip sums the five strip energy sums and calculates the "fine-grain" electromagnetic bit which identifies the electromagnetic shower candidates on the basis of the energy profile of the 5×5 crystal matrix or *Trigger Tower* (TT). The TT energy sum and the fine grain bit are transmitted to the TCC at 800 Mbits/s. The corresponding crystal data (the ten 40 MHz discrete samples per crystal) upon receipt of a positive trigger L1A decision, is transmitted to the Data Concentration Card (DCC) also on the OD electronics system over a distance of approximately 80 m through optical fibres at a data transfer rate of 800 Mbits/s.

The OD electronics system, shown in Figure 3.11, hosts the DCC, TCC and CCS electronic boards. It serves both the Data Acquisition (DAQ) and trigger paths. In the DAQ path, the DCC collects the digitized crystal data from up to 68 FE boards and performs data verification and data reduction based on readout flags from the Selective Read-Out Processor (SRP) system, while in the trigger path, the TCC collects trigger data from up to 68 FE boards corresponding to a supermodule in the barrel and 48 FE boards corresponding to the inner and outer part of a 20^o in ϕ. The TCC completes a Trigger Primitive Generation (TPG) process started at the FE by computing *trigger primitives* and synchronized them by the Synchronization and Link mezzanine Board (SLB) before their eventual transmission to the Regional Calorimeter Trigger system at each LHC proton bunch crossing. Each Trigger Primitive (TP) consist of the summed transverse energy deposited in each TT and the fine-grain bit. The 24 bits TPs are stored in the TCC during a Level-1 trigger latency and multiplexed into an 8-bit word encoding the summed transverse energy in a tower and the fine-grain bit and finally transferred to the DCC at a rate of 1 word/25 ns.

The CCS is tasked primarily with distributing fast timing signals (LHC 40.08 MHz clock, L1A and control signals to the TCC, DCC and CCUs of the FE board. By interfacing the on- and off-detector electronics to the TCS and Trigger Throttling System (TTS), the CCS synchronizes all the activities of the OD and configures the on-detector electronics [36].

The 40.08 MHz LHC Bunch-Crossing (BX) clock and 11.246 KHz (88.9 μs) orbit signals from the RF generators of the LHC machine are broadcast over singlemode optical fibres from high power laser transmitters at the Prevessin Control Room (PCR) to the four LHC experiments. The combined signals are received at CMS by a TTC machine interface (TTCmi) minicrate carrying an LHC clock receiver (LHCrx) module and a TTC Clock fanout (TTCcf) module. Embedded in the TTCmi is a voltage controlled *Quartz Phase-Lock Loop* (QPLL) ASIC with a clock frequency or locking range of 40.0749 MHz to 40.0823 MHz. The QPLL acts as a jitter-filter and clock multiplier for clock signals operating at the LHC bunch-crossing frequency with and output clock time jitter up to 16 picoseconds (ps) in rms. The QPLL adjusts for any clock phase and then makes multiple copies of the LHC clock signals before distributing them to the local TTC transmitters. The local TTCcf distributes the low-jitter LHC clock signals to the TTC receiver (TTCrx) module of the TTC system which is eventually distributed through optical fibres to FE boards, trigger and OD readout electronics used for Level trigger accept, bunch counter reset, bunch crossing number event counter reset and event number and the millions of electronics channels. The TTCmi also has master phase adjustment for the orbit signal and facilitates monitoring of clock signal quality. The local TTC system is programmed to distribute to all the trigger synchronization circuits or Synchronization and Link mezzanine Board (SLB) the Bunch-Crossing zero (BC0) broadcast signal.

In the SLB of each TCC, the BC0 timing is synchronized [37] to match the arrival of the bunch zero or first bunch crossing TP data at the SLB. The synchronization circuits make use of FIFOs to archive the synchronization i.e. after a clear FIFO is executed during the LHC extraction gap of 127 missing proton bunches of the LHC orbit, the first data entering each FIFO must correspond to the bunch zero crossing. This synchronization is needed to account for the non-negligible and unpredictable phase on the trigger primitives arrival time to the processors introduced by different particle flight paths to different regions of the detector, different optical transmission fibre lengths and different phase lock delays in the electronic serializers and ensures that the electromagnetic and hadronic calorimeter trigger primitives in each TT is time aligned with respect to the "bunch 0 clock" which corresponds to the start of the LHC orbit. The synchronized trigger primitives are sent at 1.2 Gbits/s to the Regional Calorimeter Trigger through 10 m electrical cables where with HCAL trigger primitives, the electron/photon and jet candidates are computer together with their total transverse energy.

In the DCC the data integrity is verified and formatted together with the TCC information, the selective readout flags and the crystal data of the selected TT according to the selective readout processor flags. Words of 64 bits are formed and sent to the DAQ at L1A rate provided by the trigger system.

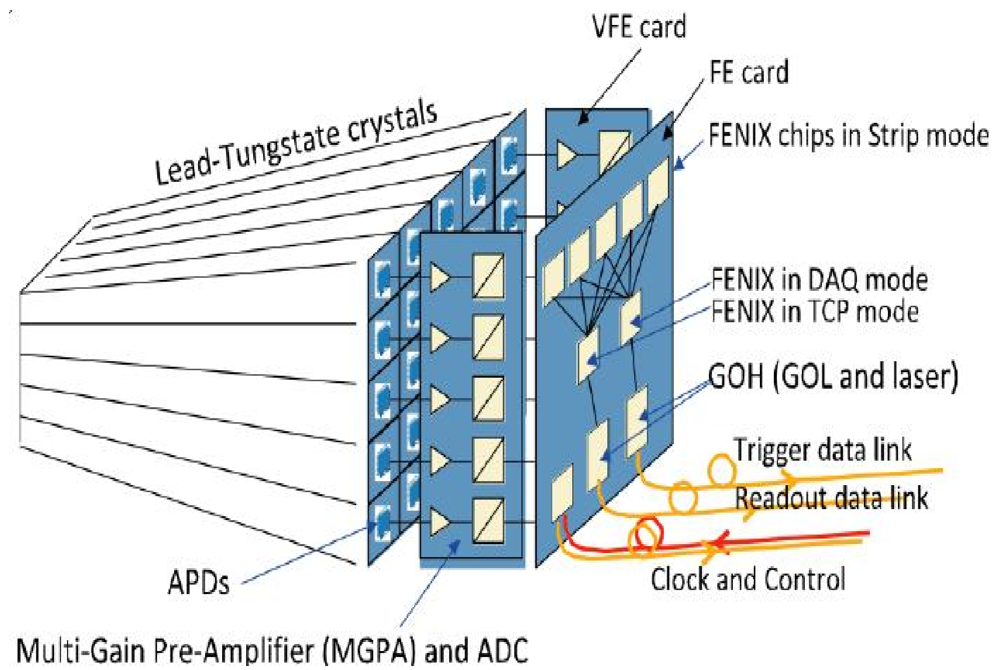

Figure 3.9: Schematic diagram of the ECAL electronics readout Trigger Tower (TT) or Front End (FE) board.

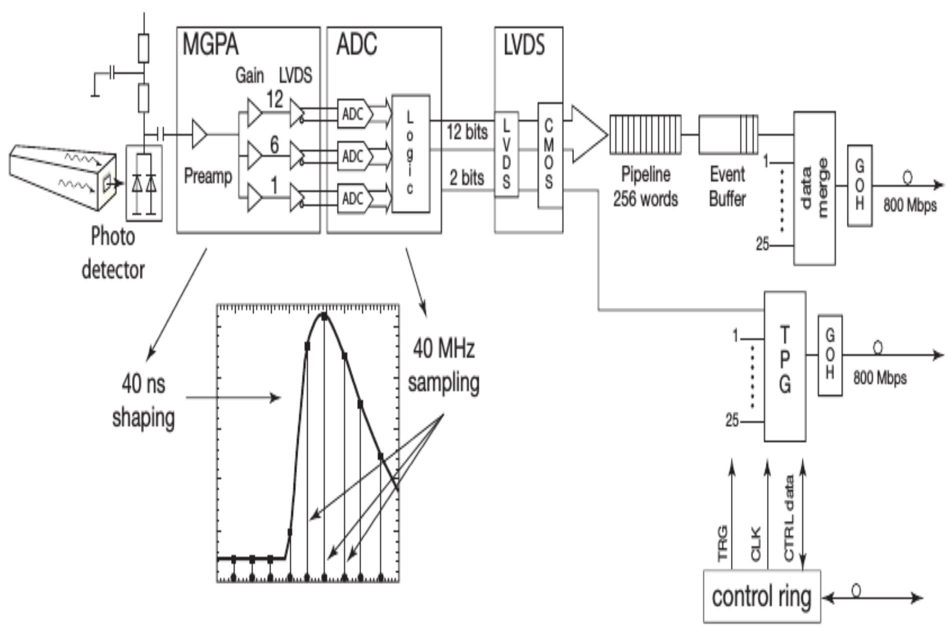

Figure 3.10: Schematic diagram of the ECAL electronics readout for a single crystal.

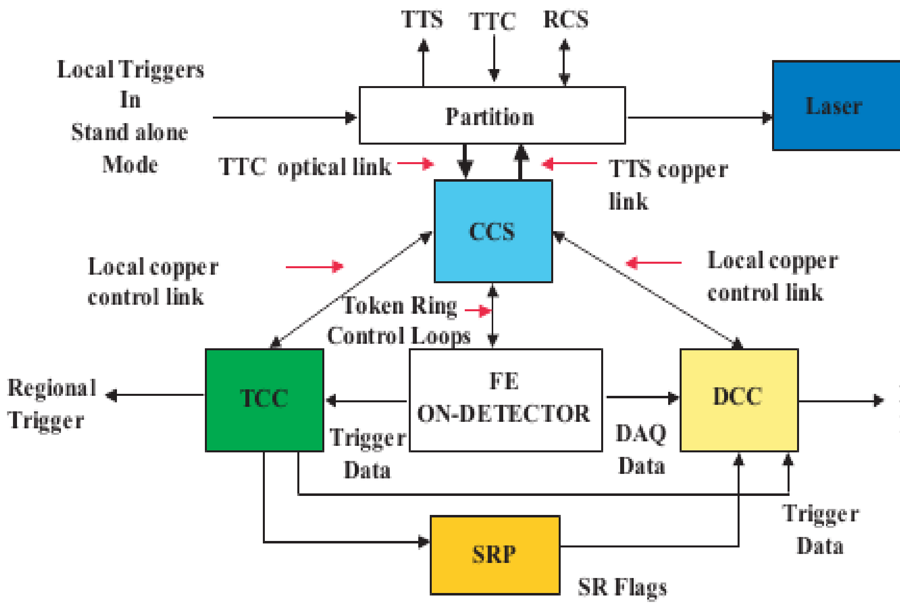

Figure 3.11: Schematic diagram of the ECAL Off-Detector and Readout Architecture.

Hadronic Calorimeter

The Hadron Calorimeter (HCAL) is important for the measurement of protons, pions, kaons, fragmenting quarks and gluons also known as *jets* with energies in the GeV- TeV range and neutrinos or exotic particles producing apparent missing transverse energy. High-energy hadrons traveling through a medium transfer their energy to the constituent atoms in the medium through ionization or excitation of atoms in the medium. This energy deposition is through the formation of ion-electron pairs (positive ion and electron) which ultimately leads to the production of *hadronic showers*. A hadronic shower has an *electromagnetic* (em) and a *non-electromagnetic* (non-em) components. The em component which has one to two thirds of the energy deposited by the high-energy hadron is measured in the same way as in ECAL using an active scintillating material while the non-em shower energy is deposited in an absorber material through the inelastic collision of the incident hadron with the nucleus of the non-active absorber material and does not contribute to the measured signal but rather in the production of secondary hadrons which travel through the next layers of the absorber material producing further hadrons and very densely ionizing particles. This combination of active and non-active material is the chosen design for high-energy hadron detection in HCAL and is the reason why the HCAL is referred to as a *Sampling Calorimeter*.

The HCAL is comprised of four distinct subdetectors: the Hadronic Barrel (HB), Endcap (HE), Outer Barrel (HO) and Forward (HF). Unlike the ECAL, the HB, HE and HO subdetectors are scintillator-sampling calorimeters using brass plates as the inactive absorber material and plastic scintillator tiles with embedded wavelength shifting fibers (WLS) to bring out the light as the active material. The brass plate is used for absorbing and so stopping the high-energy hadron producing hadronic showers with an em (particles like π^0, η and other mesons generated in the absorption process which decay to photons and develop electromagnetic shower) and non-em (mostly charged pions and kaons) components while the plastic scintillator with WLS is used for measuring the energy of the em component. The first active layer of the scintillating tiles is situated directly behind the ECAL in order to actively sample low energy showering particles from the support material between the ECAL and HCAL. The plastic scintilator, chosen for its long-term stability and moderate radiation hardness, is divided into 16 η sectors resulting in segmentation of $\Delta\eta \times \Delta\phi = 0.087 \times\ 0.087$. The scintillating light is collected and brought to Hybrid Photodiodes (HPDs) through the WLS in the HB and HE. HPDs have high electrical noise and was used during the CMS data recording of this thesis have been replaced with *silicon photon multipliers* (SiPM) which have low noise during the CMS detector upgrade in 2013-2014.

The HB, covering the region $|\eta| < 1.3$, is divided into two-half barrel (HB+ and HB-) sections with each composed of 18 identical 20^o wedges in ϕ. Each wedge is made of flat brass alloy and steel (only front and back plates) absorber plate. The HO is an extension of the HB outside the solenoid and utilizes the solenoid coil as an additional absorber. It is used to identify the starting shower and to measure the shower energy deposited after HB. For this reason the HO is also known as the *tail catcher*. The HE covers the region $1.3 < \eta < 3.1$, and has plastic scintillation tiles with granularity of $\Delta\eta \times \Delta\phi = 0.087 \times\ 0.087$ for $|\eta| < 1.6$ and $\Delta\eta \times \Delta\phi = 0.17 \times\ 0.17$ for $|\eta| > 1.6$. This granularity provides good measurement of forward moving particles through non-overlapping showers.

The HF occupies a pseudo-rapidity region of $3 < |\eta| < 5$. Its purpose is to provide a nearly 4π hermetic phase space coverage required for the measurements of missing transverse energy (MET). MET is the established signal for particles like neutrino and exotic particles such as supersymetric particles like gravitino which escape detection. The HF consists of radiation hard quartz fibres embedded in steel absorbers running parallel to the beam axis. The signal from Cherenkov light emitted in the quartz fibres in response to charged particles make it possible for the HF to detect all charge particles in the forward region. The HF calorimeter has long and short fibers for better sampling and to distinguish em showers from non-em showers. The choice of quartz fibers is because of its high resistance to the high radiation dose present in the more forward region of the CMS detector and for its fast production of light through the Chererenkov process.

For $|\eta| < 1.48$, the HCAL cells map on to 5×5 ECAL crystal matrix to form calorimeter towers projecting outwards from near the nominal interaction point. In each tower, the energy in ECAL and HCAL cells is summed to define the calorimeter energy tower. The energy ratio of an HCAL tower to an ECAL in a calorimeter energy tower can be used to improve photon and electron identification.

3.2.3 Muon Chambers

Muons unlike electrons and hadrons do not deposit most of their energy in the calorimeters. They are capable of traveling across the entire CMS detector into the muon chambers. Muons produce tracks which run across the CMS detector starting from the silicon pixel and strip subdetector closest to the pp interaction point (IP) called the *Tracker*, depositing very little fraction of their energy in the calorimeters, and unto the muon chambers. The muon chambers use the process of ionization and a 2 T magnetic field from the return iron yokes (bending the tracks of charge particles) to measure the momentum of charged particles. The three different types of muon chambers used in the CMS detector are: the Drift Tubes (DT) chambers in the barrel, Cathode Strip Chambers (CSC) in the endcaps and Resistive Plate Chambers (RPC) glued to the DT and CSC chambers. Four layers or stations of DT/RPC and CSC/RPC are embedded in an interleaved style with the iron yoke for track reconstruction and triggering. Figure 3.12 is a longitudinal view of the CMS detector showing the position of the muon stations. The DT and CSC record track segments characterized by the position of the track and the bending angle. This information is used to determine the precise transverse momentum and charge of the particle during event reconstruction. The RPCs(DTs and CSC will also be used after the current detector upgrade) are dedicated L1 trigger chambers used to determine the candidate muon's approximate transverse momentum and proton bunch crossing number. The RPC has a timing resolution of about 3 ns.

We summarize in Table 3.2 CMS detector performance and material type of each subdetector.

3.2.4 Event Triggering

Assigning particles to the correct *pp* collision and storing the partially reconstructed event in the DAQ before the next collision happens in 25 ns is a very challenging problem. In addition to this, we want to select only potentially interesting events i.e. events with large transverse energy or interesting particle combination, to reduce the event rate during read-out and since the full event information comes from millions of electronic channels of the CMS detector, the signals from every channel have to be synchronized with the 40.08 MHz LHC bunch crossing frequency. CMS solves these very challenging problems by using a Timing, Triger and Control system and two event selection triggers: a *Level*-1 (L1) and an *High Level Triggers* (HLT) trigger.

The L1 trigger consists of custom-designed programmable electronics system implemented in FPGA and ASIC technology and uses information from the calorimeter, muon and a global trigger board. The global trigger makes the final decision based on the decisions of the calorimeter and muon triggers to reject or keep an event for further processing at the HLT trigger. The L1 trigger is responsible for selecting the best 100,000 events/second from the initial 1 billions events/second produced from *pp* collisions. L1 trigger selection and synchronization starts with the Trigger Primitive Generators (TPGs) which are based on summed transverse energy deposits in the calorimeter trigger towers and track segments of hit patterns in the muon chambers, respectively. The TPG electronics is integrated with the calorimeter read-out electronics which we described in section 3.2.2.

The calorimeter TPGs generation and synchronization begins in the on-detector front-end electronics which receives ADC signals from 25 crystals also known as trigger towers at the trigger level. An off-detector Trigger and Concentration Card communicating with the Trigger, Timing and Control (TTC) system which distributes the LHC 40.08 MHz bunch crossing clock, collects trigger primitives (tranverse energy sums) from 68 front-end electronics boards in the barrel and 48 boards in the endcaps, finalize the TPG generation and store the trigger primitives during a L1 latency before transferring the trigger primitives to the regional calorimeter trigger (RCT) and finally the Global trigger upon receipt of a L1A trigger signal from the TTC system. In the RCT, Synchronization and Link Boards (SLB) carrying synchronization circuits synchronize the trigger data of each trigger tower. Each trigger tower is aligned with the bunch crossing zero signal by comparing it to histograms of the LHC bunch crossing profile. The aligned data is read by the data concentration card and after verification and reduction of event size if needed is sent to the DAQ.
In HCAL the energy values of the front and back towers are added to the trigger primitives and the bunch crossing number is assigned by a peak filtering algorithm. A schematic picture of the CMS Level-1 trgger architecture is shown in Figure 3.13.

The HLT is a software implementing a sequence of preliminary event selection algorithms and running on a farm of more than 1000 standard computers. These complex algorithms include instructions like, match tracks to hits from the muon chambers, select energy deposits above a certain threshold in the calorimeters with no tracks and more. The HLT begins the first step of event selection and just like the L1 trigger, the HLT uses assimilated and synchronized information from different parts of the CMS detector to create an entire event. By the time the HLT selection process is complete, there are now only 100 events/second with the remaining 99,900 thrown away. Considering an average event size is 1 Megabyte during stable and effective LHC *pp* collision period of a year (10^7 seconds), CMS produces about a Petabyte of data each year which is stored and used later for offline physics analysis.

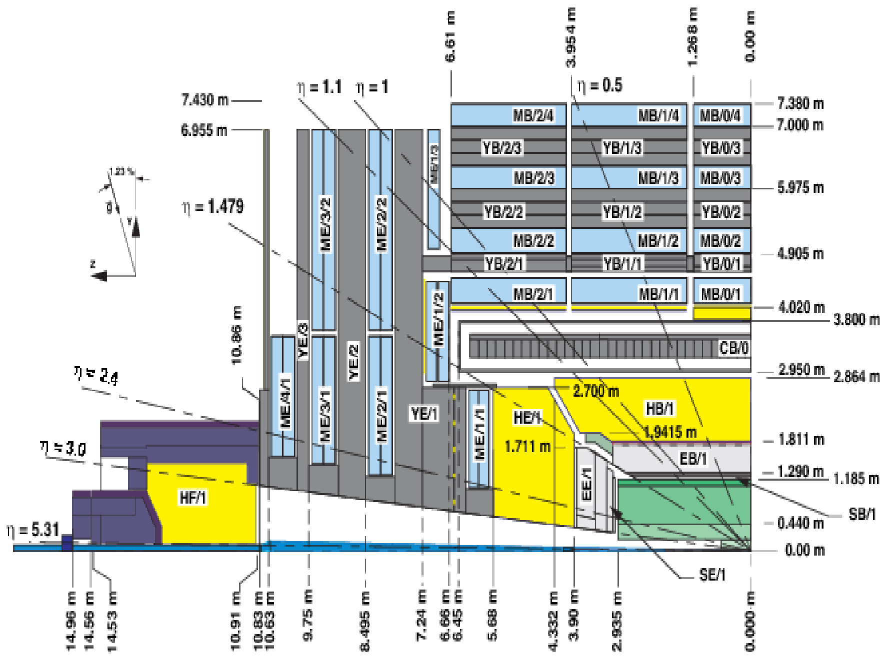

Figure 3.12: Cross section view showing the coverage range of CMS sub-detectors and their longitudinal distance from the IP.

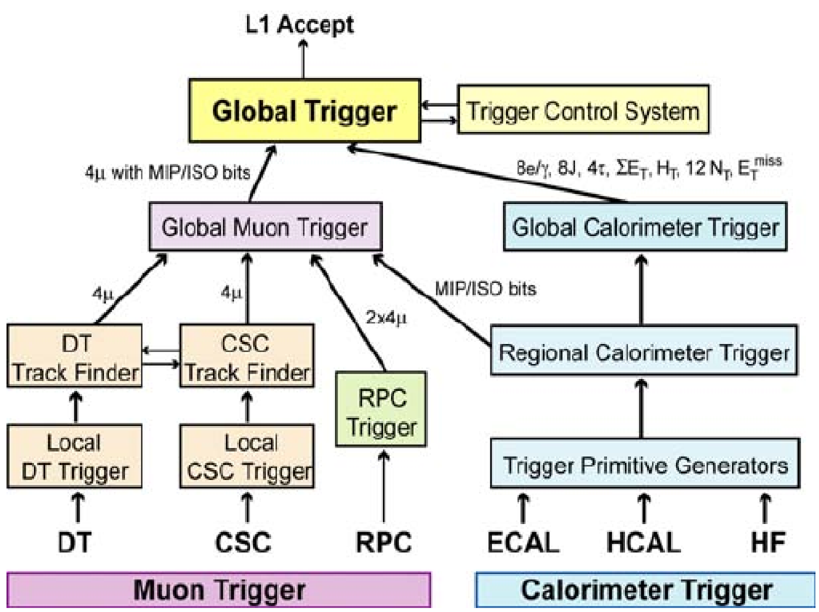

Figure 3.13: Level-1 trigger architecture of CMS.

CMS Detector Performance 2012

Subdetector	**Quantity**	**Resolution**	**Uses**
Tracker	Momentum[GeV/c]	$\sigma_T/p_T \approx 1.5 \times 10^{-4} p_T + 0.005$	Silicon Pixels and Strips
ECAL	Energy[GeV]	$\sigma/E \approx 3\%/E + 0.003$	$PbWO_4$ Crystals
ECAL	Time[ns]	$\sigma(\Delta t) = \frac{N}{A_{eff}/\sigma_n} \oplus \sqrt{2}\bar{C}$	$PbWO_4$ Crystals
HCAL	Energy[GeV]	$\sigma/E \approx 100\%/E + 0.05$	Brass + Scintilator
Muon Chambers	Momentum[GeV/c]	$\sigma_T/p_T \approx 1\%$ 50 GeV to 10% 1 TeV	inner tracker + Muon Systems
Magnetic field	B-field strength[T]	3.8 T + 2 T	Solenoid + Return Yoke
Triggers	On/Off-line	Levels	L1(On-line) +HLT(Off-line)(L2+L3)

Table 3.2: CMS detector performance for LHC RUN 1 [34].

Chapter 4

Time Reconstruction and Resolution

ECAL Time Overview

The Electromagnetic Calorimeter (ECAL) was designed to precisely measure the energy of electrons and photons with a target barrel resolution of 0.5% for photons with energy more than 50 GeV. In addition to energy measurements, the combination of fast scintillation for $PbWO_4$ crystals, the electronic pulse shaping and a digitization rate of 40 MHz allows for an excellent time measurement. The time of the signal measured by each crystal is reconstructed from 10 discrete samples of the digitized analog pulse height[35, 36, 38].

4.1 Time Reconstruction

An analog pulse shape from a single crystal is shown in Figure 4.1(a). Overlaying the pulse shape are typical 10 digitized samples in red. The first three samples are taken in the absence of a signal and correspond to the pedestal. The ADC chip responsible for the digitization, has a sampling frequency of 40 MHz, i.e. one sample is made every 25 ns, which is the same rate as the LHC proton-proton bunch collision frequency of one bunch crossing every 25 ns, and a total time of 250 ns corresponding to the 10 digitized samples is covered. In addition, the timing phase of sampling within the 25 ns interval is adjusted so that the maximum of the signal pulse shape corresponds to one of the digitized samples to within 1 ns. A time reconstruction algorithm uses the 10 digitized samples to measure the time of a single channel by finding the precise time, $\mathbf{T_{max}}$, corresponding to the maximum of the pulse shape [39, 40].

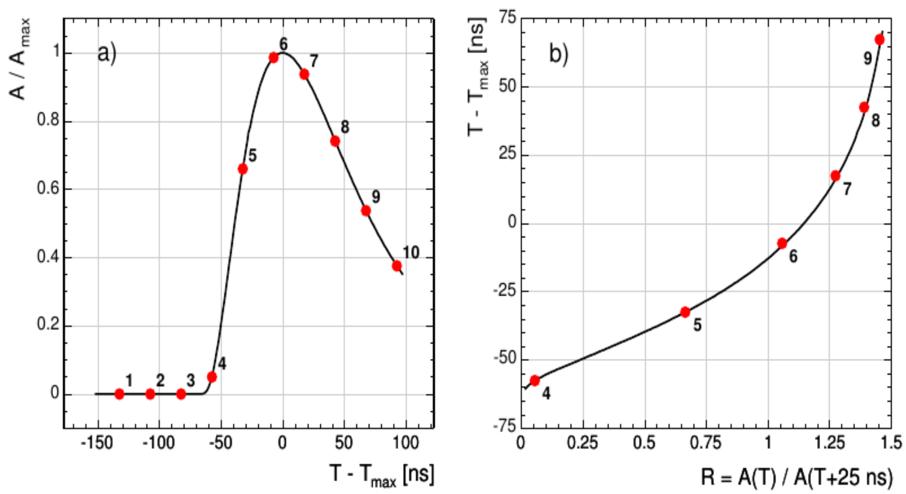

Figure 4.1: (a) A measured ECAL pulse shape for a single channel. (b) $\mathbf{T} - \mathbf{T_{max}}$ Vs $R(T)$ relationship whose inverse is $T(R)$. Solid line is pulse shape from test beam while dots are typical 10 discrete samples corresponding to signal from proton-proton collision.

The pulse shape is used to determine $\mathbf{T_{max}}$ in the following way. The height ratio

$$R_i = A(T_i)/A(T_{i+1}), \tag{4.1}$$

where T_i is the time when the i^{th} pulse height sample is taken, is uniquely determined from the pulse shape. The pulse height ratio, $R_i(T_i - T_{max})$, shown in Figure 4.1(b), is a function of the time that the pulse height of the first of a pair of samples is taken relative to the time of the maximum pulse height, $\mathbf{T_i} - \mathbf{T_{max}}$. From the inverse of this function, $T(R)$, we obtain $\mathbf{T_{max}} = T_i - T(R_i)$ and the uncertainty, σ_i, for each R_i point. The uncertainty on each measurement is a product of the derivative of the function, $T(R)$, and the uncertainty on the value of R_i which itself depends on three separate uncertainties: the noise fluctuation (σ_n) of each sample, the uncertainty in the estimation of the pedestal value, which is always subtracted from the measured value, and the truncation during 12-bit digitization.

A precise value for $\mathbf{T_{max}}$ is, most of the time, obtained using the ratios R_4 through R_7. The other ratios, R_8 and R_9 are not used for the estimation of T_{max} because their associated uncertainties are large due to the large slope of the $T(R)$ function. A weighted average of each $T_{max,i}$, and σ_i, obtained from ratios R_4 through R_7 is given as

$$\mathbf{T_{max}} = \frac{\sum \frac{T_{max,i}}{\sigma_i^2}}{\sum \frac{1}{\sigma_i^2}} \quad , \qquad \frac{1}{\sigma_T^2} = \sum \frac{1}{\sigma_i^2} \tag{4.2}$$

where the sum is from $i = 4, \cdots, 7$, gives the best estimate of $\mathbf{T_{max}}$ and uncertainty.

4.2 ECAL Time Performance from Test Beam

4.2.1 ECAL Time Resolution

The intrinsic time resolution of ECAL, measured during test a beam study, can be parametrized using the standard deviation of a Gaussian distribution. It consists of three main contributions which can be summed in quadrature since they are uncorrelated. These three contributions are the noise, stochastic and constant terms. The *Noise* (N) term arises from the electronic noise, coherent movement of the baseline and effects of overlapping hits. The *Stochastic* term (S) arises from fluctuations in the number of photons collected during the sample times. Lastly, the *Constant* term (C), whose contribution is independent of the energy deposited and arises from both variations in the point of shower initiation within the crystal, variations in the pulse shape for each channel and calibration effects. The full parametrization of the time resolution with all three contributions is given as

$$\sigma^2(t) = \left(\frac{N}{A/\sigma_n}\right)^2 + \left(\frac{S}{\sqrt{A}}\right)^2 + C^2, \tag{4.3}$$

where A is the measured amplitude in ADC counts corresponding to the energy deposited and σ_n is the intrinsic noise in the amplitude for an individual channel. σ_n has a value of 42 MeV and 140 MeV in the barrel and endcap, respectively. $N = 33$ ns has been estimated from Monte Carlo (MC) simulation studies and the contribution from the stochastic term, (S) is small, with a value of $S < 7.9$ ns$\cdot$ MeV$^{1/2}$.

The measured timing resolution was obtained from the Gaussian distribution of the difference in the time of two crystals sharing energy and belonging to the same electromagnetic shower, after about 25% of the barrel and endcap crystals were exposed to electron beams with energy between 15 GeV and 250 GeV at H2 and H4 test beam facilities at CERN. This method of measuring $\sigma(t)$ using the time difference of two crystals reduces the contribution to the constant term arising from crystal-to-crystal synchronization. And since the stochastic term is small, the parametrization of the time resolution expressed in Equation 4.3 can be reduced to

$$\sigma^2(t_1 - t_2) = \left(\frac{N}{A_{eff}/\sigma_n}\right)^2 + 2\bar{C}^2 \tag{4.4}$$

where $A_{eff} = A_1 A_2 / \sqrt{A_1^2 + A_2^2}$, while $t_{1,2}$ and $A_{1,2}$ are the times and amplitudes of the two crystals. $\bar{C}$ is their residual constant term contribution.

In practice, the time resolution is measured from the standard deviation of a Gaussian fit to the time distribution from each slice of A_{eff}/σ_n of the A_{eff}/σ_n distribution. The resulting distribution of $\sigma(t_1 - t_2)$ of these standard deviations plotted against A_{eff}/σ_n is used to extract the noise and residual constant terms. The result presented in Figure 4.2, of the test beam study gives a noise factor $N = (35.1 \pm 0.2)$ ns which agrees with our Monte Carlo estimate to within 6%.

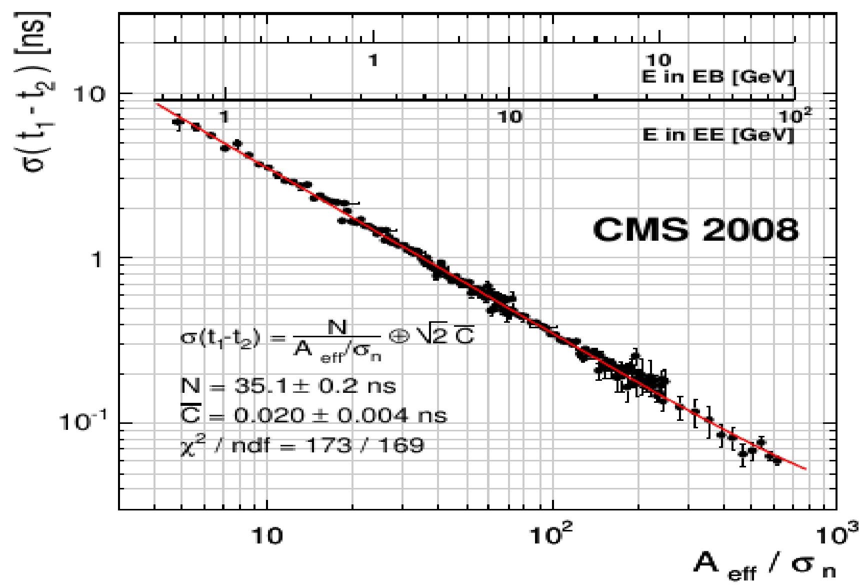

Figure 4.2: Difference in the time measurements as a function of A_{eff}/σ_n of two crystals sharing an energy and belonging to the same electromagnetic shower obtained during electron test beam measurements. The single crystal energy scales for barrel (EB) and endcap (EE) is overlaid. The fitted results give $N = (35.1 \pm 0.2)$ ns and $\bar{C} = (20 \pm 4)$ ns.

Knowing that it takes on average 4.3 ns for a photon to reach the ECAL surface produced from the proton-proton interaction point, this demonstrates an intrinsic time resolution of 2% for photons with energy $E > 20\,\text{GeV}$ in the barrel.

4.3 ECAL Time Performance from Collision

The time resolution during LHC proton-proton (pp) collisions is expected to be worse than what the test beam study show since the conditions during test beam are not the same as during LHC pp collisions. Effects like LHC clock time variations over extended periods, time bias with energy due to gain transitions in the front-end electronics and loss in crystal transparency due to radiation could affect the pulse shape which will ultimately worsen the ECAL time resolution. The impact of some of these effects can be minimized if all the crystals in ECAL are synchronize using events from pp.

4.3.1 Crystal Time Synchronization

The cause of crystal time variations may be either due to differences in pulse shape or LHC clock drift over time or time shifts introduced during CMS detector repairs. These variations of about 1 to 3 ns on average can be removed by time aligning or synchronizing all 75,848 $PbWO_4$ crystals in ECAL as the need arises. This synchronization ensures optimal timing resolution throughout the LHC stable beam collision period and continues to maintain the uniform response by all the crystals in measuring the times of electromagnetic particles produced from pp collisions. It also guarantees that the particles belonging to a given event are always assigned to the correct LHC proton bunch crossing.

Photons produced from pp collisions at the interaction point (IP), traveling along a straight path with nearly the speed of light and impinging on the front face of the crystals in ECAL are used to define the absolute zero or reference time.

The synchronization is performed at two levels. The first is by adjusting in steps of 1.04 ns the time delay of the LHC clock signal of a 5×5 crystal matrix at the front-end electronics which make up the Clock and Control Unit (CCU). This is called *Hardware Synchronization.* The second is by adjusting the time of the individual crystals to correct for the presence of the "T_{max} Phase", the difference in pulse shape and the different intrinsic delays in each channel. The crystal time is adjusted during event reconstruction to ensure the best timing reconstruction of each crystal and the process is called *Offline Crystal Synchronization.*

Offline Crystal Synchronization

The purpose of offline crystal synchronization is to compute time constants needed for the synchronization of all the crystals. Since the crystals are well synchronized if their measured average time over many events for photons produced from pp collisions at the interaction point (IP), traveling along a straight path with nearly the speed of light and impinging on the front face of the crystals is zero, this means the time constant of each crystal is taken to be the reverse sign of the mean average time measured by the crystal. To validate the crystal time constant, we expect the sum of its measured mean time and the time constant to be zero when averaged over many events. The average time and time constant are computed using the reconstructed energy deposits (rechits) by the photon on the crystal. The time constants are produced in sets and have an *interval of validity* (IOV) which is defined by the a pp collision running period of the LHC. A total of 17 IOV sets of time constants were produced for the entire LHC run in 2011 and 44 IOV sets for 2012. Presented in Figure 4.3 and 4.4 are maps showing the average time for the 61,200 crystals in EB (top plots) and 14648 crystals in EE (bottom plots). The maps in Figure 4.3 show the average time of each crystal before synchronization. A few crystals in EB can be seen having an average time as large as -1.0 ns while many in EE have average times varying from -1.0 to $+1.0$ ns, especially those in the high-η region. The few white spots on the maps are crystals which were masked during data recording by ECAL. The mean time of the average time for all the crystals in EB is -0.113 ns with an average of 205 number of rechits per crystal and -0.337 ns (-0.346 ns) with the number of rechits per crystal of 333 (342) for EE$-$ (EE+). The standard deviation of the mean time for all the crystals in EB is 0.119 ns and 0.282 ns (0.256 ns) for EE$-$ (EE+).

Figure 4.4 show the average time of the same ECAL crystals after synchronization. Most of the crystals have a mean average time of approximately 0 ns, indicating the accuracy of the time constants and performance of the synchronization. The improvement can be see in the mean time of the average time for all the crystals in EB is now -0.014 ns and -0.003 ns (-0.004 ns) for EE$-$ (EE+) for the same number of rechits per crystal as before synchronization. The standard deviation of the mean time for all the crystals in EB is 0.021 ns and 0.002 ns (0.021 ns) for EE$-$ (EE+).

The details of the procedure for performing the synchronization and the results obtain for all the IOVs produced in the entire LHC Run 1 can be found in [41].

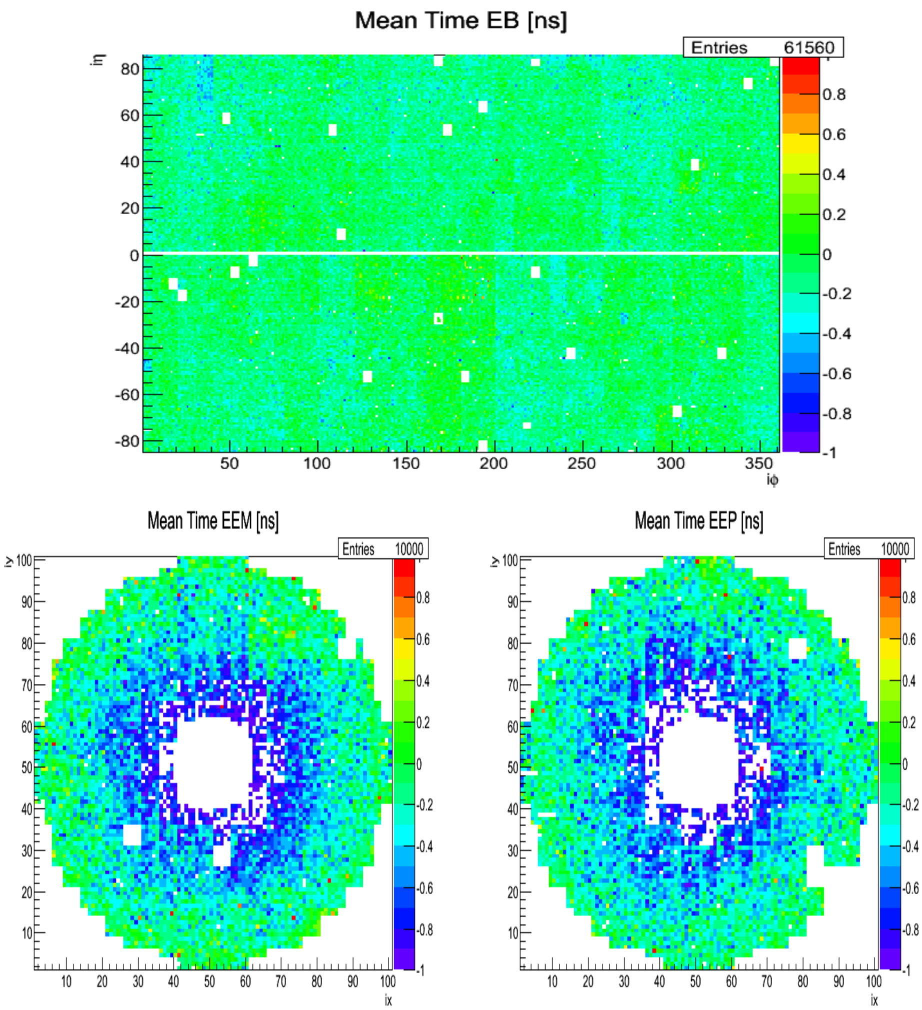

Figure 4.3: Timing maps showing the distribution of average (mean) time for each $PbWO_4$ crystal in EB (top) and EE (below: EE−(left), EE+(right)) before crystal synchronization.

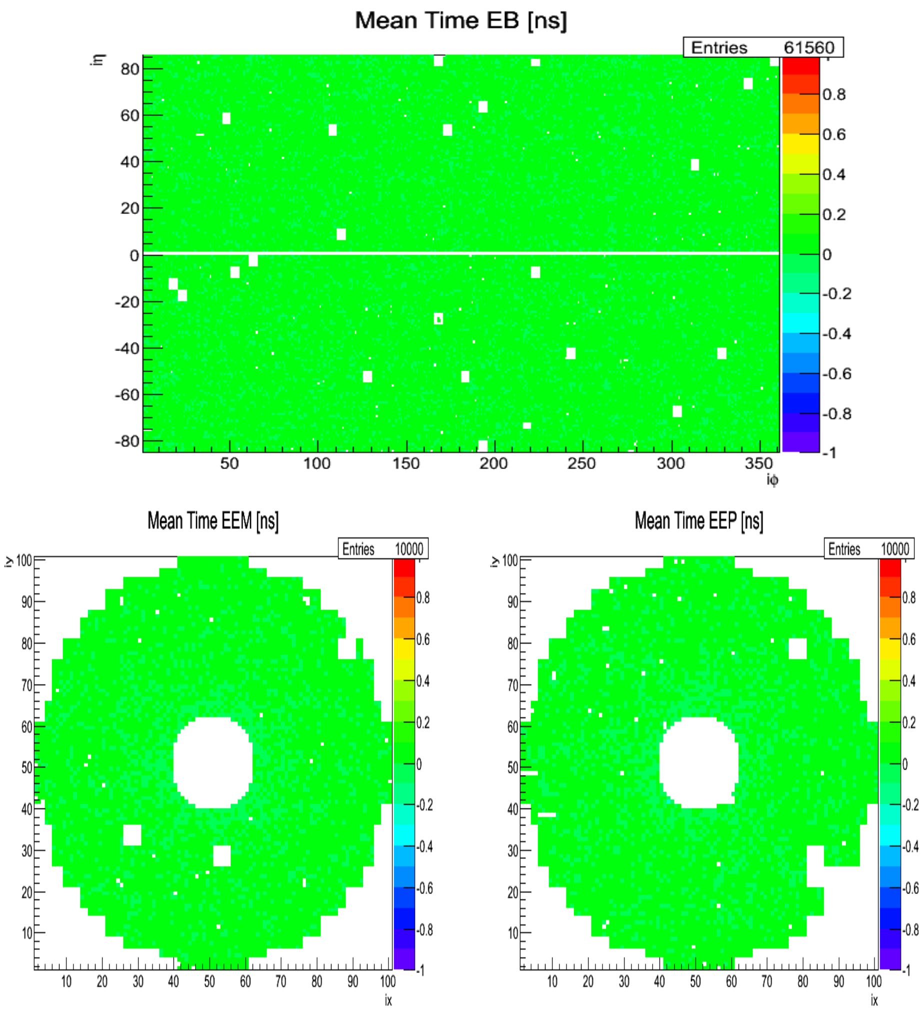

Figure 4.4: Timing maps showing the distribution of average time of each crystal after synchronization with most crystals having an average time of zero indicating the success of the crystal synchronization process and validity of the time constants.

Hardware Synchronization

We synchronize the CCUs using histograms of the trigger tower timing from Data Quality Monitoring (DQM) services of events from *pp* collisions. The synchronization is often done during LHC stable proton beams and guarantees that trigger primitives are assigned to correct LHC proton bunch crossing. It is also possible to synchronize the CCUs using crystal transparency monitoring with lasers.

Hardware Synchronization With Collision

The CCU average time is computed for events produced from *pp* collision and the sign of the time constants is chosen to be opposite to the offset observed from the LHC Clock drift so that their difference for each CCU is zero. During the process of synchronization, the CMS experiment experiences interruption of its data recording process during stable beams. The reason for the interruption is to update the CCUs with the new time constants before the next stable proton beams arrive. Since the CMS experiment wants to eliminate such interruptions, an alternative approach to synchronizing the CCUs is needed. This new approach, which is yet to be validated, is a laser based approach and does not require any interruption of the CMS experiment during stable beams.

Hardware Synchronization With Laser

The ECAL laser system comprise of two lasers, a 440 nm wavelength (close to peak emission for $PbWO_4$ crystals) laser used for monitoring crystal transparency losses and a 796 nm wavelength laser for monitoring the readout electronics chain from photodetectors to the electronics (i.e. APDs to ADCs). The timing information from the laser can be used for monitoring the Clock and Control Unit (CCU) time with the time of each crystal from laser averaged over 600 event pulses to minimize the effect of the jitter which is less than 4 ns. This crystal time is denoted as $\mathbf{T^{APD}_{MAX}}$. The laser system is also equipped with a fast acquisition card called MATACQ which also records the time for each crystal denoted as $\mathbf{T_{MATACQ}}$. This time is equally averaged over 600 event pulses. The difference, $\mathbf{T^{APD}_{MAX}} - \mathbf{T_{MATACQ}}$, of the two times, averaged over the 25 crystals of each CCU is used as the time for each CCU, i.e. $\mathbf{t_{CCU}} \equiv \left\langle \mathbf{T^{APD}_{MAX}} - \mathbf{T_{MATACQ}} \right\rangle_{25}$. To extract the time shift for each CCU, we study the change in $\mathbf{t_{CCU}}$ before ($\mathbf{t^{B}_{CCU}}$) and after ($\mathbf{t^{A}_{CCU}}$) a hardware intervention during CMS machine repairs. The time difference, $\mathbf{\Delta t_{CCU}} = \mathbf{t^{A}_{CCU}} - \mathbf{t^{B}_{CCU}}$, averaged over the 25 crystals, i.e. $\langle \mathbf{\Delta t_{CCU}} \rangle_{25}$, gives the time shift, and the time constant for the CCU is the opposite sign of $\langle \mathbf{\Delta t_{CCU}} \rangle_{25}$, so that the sum of the CCU time shift and its time constant is on average zero. The CCU synchronization is done for all the 68 CCUs in a given supermodule (SM) or front-end-detector (FED). The effect of any global time shift of a given FED caused by the non-homogeneous laser light distribution on all the CCUs is also taken into account in the synchronization process if present. Each FED has 1,700 $PbWO_4$ crystals, thus 68 timing constants are needed per FED. Detail information on hardware synchronization using laser monitoring can be obtained from here [42].

4.3.2 Time Bias

The time reconstruction algorithm assumes the reconstructed time does not depend on the energy of the incident particle. However, it was observed during CMS data recording in LHC Run 1 that for very energetic particles (energy above 130 GeV in EB and 250 GeV in EE, an inherent bias in the time is introduced by the multi-gain pre-amplifier electronics at gain transition points due to not-quite-high-enough slew rate of the amplifiers. The time bias was also observed for very low energy values of less than 2 GeV. The first gain transition from gain-12 to gain-6 of the multi-gain pre-amplifier occurs near 159.744 GeV in EB and 258.048 GeV in EE. The next gain transition is from gain-6 to gain-1 and occur at energies of about TeV.

We correct the energy dependence timing bias on a rechit energy basis during event reconstruction. The corrections were applied depending on a CMS event reconstruction software (CMSSW) release version to account for different CMS data recording and event reconstruction conditions. In Figure 4.5 we show a comparison of the performance of the time bias corrections on the average time against rechit energy during the reconstruction of rechits between two CMS event reconstruction software releases. In CMSSW44X (left plot), the time bias corrections made previously did not perform as expected while in CMSSW53X (right plot) after the second set of time bias corrections were made, the average time is flat with energy. This flatness is seen even for the different modules 1 through 4 (modules contain crystals for different regions in EB) in the barrel.

The the standard deviation on the time against rechit energy in plots CMSSW44X (left) and CMSSW53X (right) of Figure 4.6, show that despite the timing bias corrections, the standard deviation does not change in both CMSSW software releases. This is as expected since the ability to measure the arrival time should not depend on the choice of the reference time.

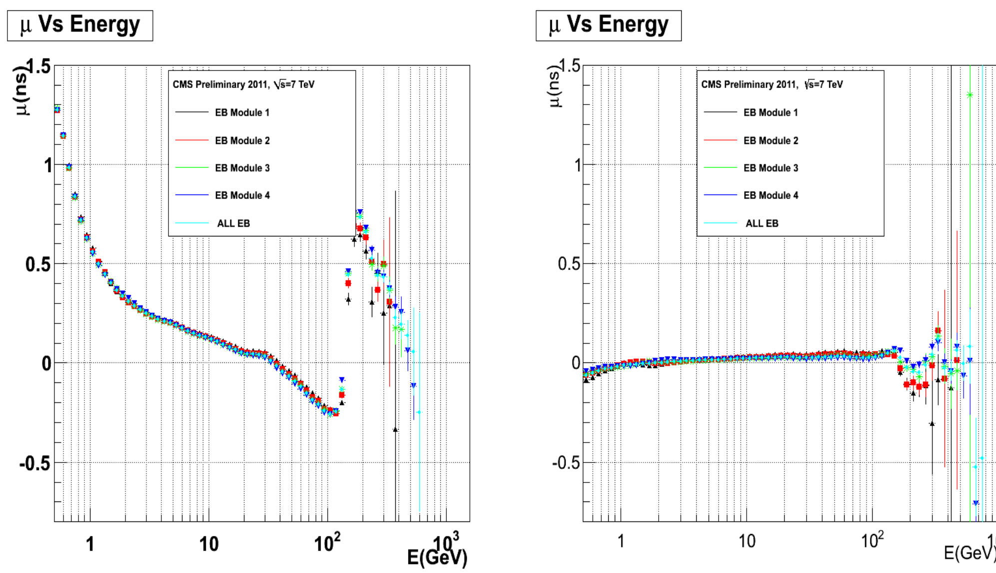

Figure 4.5: Average time (μ) against rechit energy for EB. The first gain transitions (gain-12 to 6) happens at about 130 GeV and time bias on energy is seen in CMSSW44X (left) and very little in CMSSW53X (right) where the corrections have been applied during rechit reconstruction.

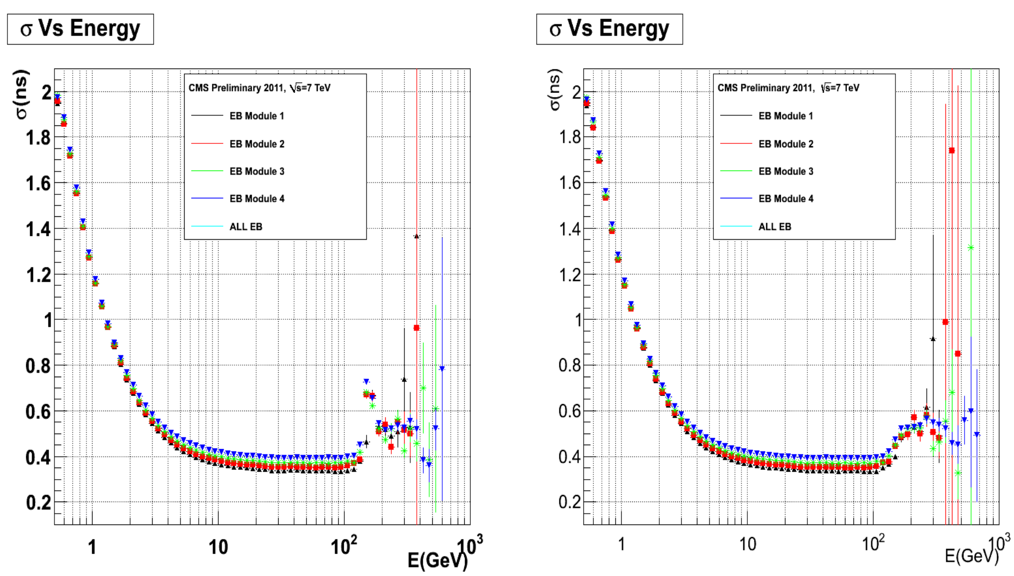

Figure 4.6: The standard deviation against rechit energy for EB in CMSSW44X (left) and CMSSW53X (right). The time bias corrections don't affect the standard deviation on the time.

4.4 ECAL Time Performance With Z Bosons

We evaluate the precision of ECAL timing measurements, during pp collisions, by studying the electron time measurements of events with the decay of the Z boson, i.e. $Z \rightarrow e^-e^+$. The selection for Z candidate events require that each electron have transverse energy above 10 GeV and the reconstructed Z mass is within, $60\,\mathrm{GeV}/c^2 < m_{e_1,e_2} < 120\,\mathrm{GeV}/c^2$, to ensure that the sample contains mostly good Z candidates.

We use the standard deviation, σ_{eff}, of the difference in arrival time of the two electrons to evaluate ECAL timing performance. This standard deviation is obtained from the difference in the seed time, t_{seed}, of each electron's electromagnetic shower after correcting for the extra time due to the bending of the electron's travel path inside the CMS magnetic field of 3.8 T. Figure 4.7 shows the distribution of the time difference, $t_{electron1} - t_{electron2} \equiv t_{seed1} - t_{seed2}$, and the value of the time resolution ($\sigma_{eff}(t_1 - t_2)$) of both electrons after adjusting the time due to its non-straight time of flight path, and in Figure 4.8, we show the *absolute time resolution* ($\sigma_{eff}(t_{seed})$), obtained from the time distribution of a single electron's seed crystal time after adjusting for the time due to the bending of the electron's flight path.

A time resolution of 0.232 ns in EB and 0.384 ns in EE is measured with a *single crystal precision resolution* ($\sigma_{eff}(t_1 - t_2)/\sqrt{2}$) of 0.164 ns in EB and 0.272 ns in EE presented in Table 4.1.

The absolute time resolution, $\sigma_{eff}(t_{seed})$, for a single crystal is measured to be 0.386 ns for EB and 0.388 ns for EE. However, if we remove the contribution from the spread in time, $\sigma(t_{colision})$, due to the finite time it takes for the two proton bunches of length 5.5 cm to collide; which is about $\sigma(t_{colision}) = \sigma(t_Z) = 0.183$ ns, we get an improvement in absolute time resolution which is 0.340 ns in EB and 0.342 ns in EE.

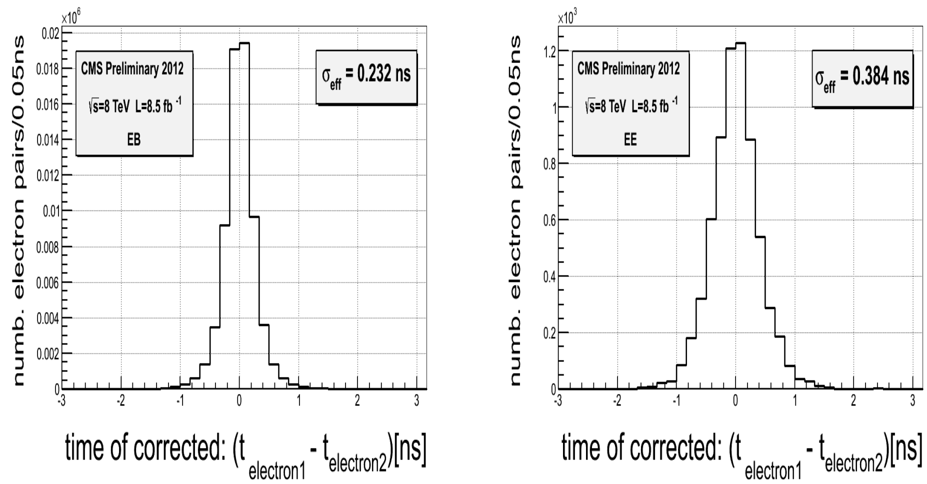

Figure 4.7: Time difference between the two reconstructed electrons in $Z \rightarrow e^{-}e^{+}$ decay. The electron time is the seed (crystal with highest energy deposit) time with additional correction due to the time of flight of the electron in EB and EE.

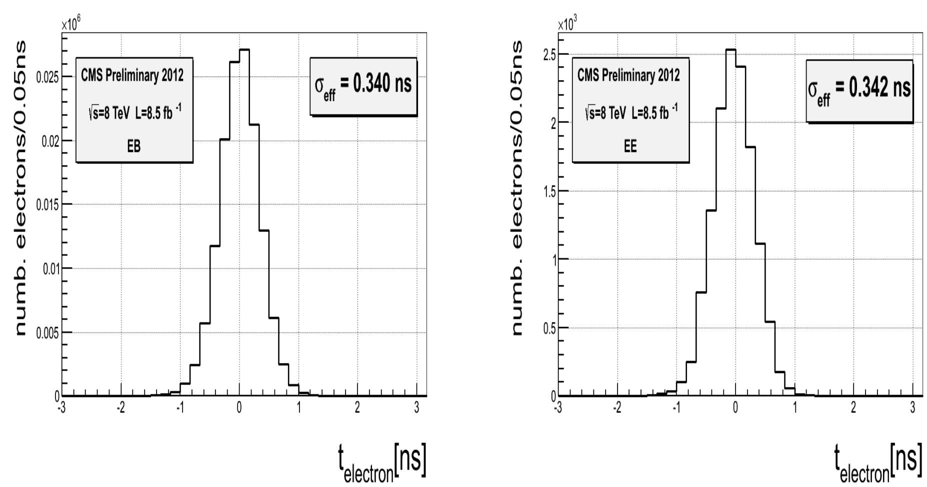

Figure 4.8: Absolute time of a single reconstructed electron in $Z \rightarrow e^{-}e^{+}$ decay. The electron time is the seed (crystal with highest energy deposit) time of the electron in EB and EE.

We also investigate the timing bias attributed to the FE electronics using events with $Z \rightarrow e^{-}e^{+}$ decay. Figure 4.9 (left) show the time resolution measured in the case where the seed crystal time is reconstructed from the same FE electronics compared to the other case, shown in Figure 4.9 (right), where the seed crystal time is reconstructed from different FE electronics. The Constant term, C, for the same FE electronics is about 0.067 ns while that for different FE electronics is 0.130 ns, which indicates that the differences in electronic readout de-synchronization among different FE contributes to the worsening of the time resolution [43, 44, 45, 46, 47].

The ECAL time resolution for the entire LHC Run 1 of 2011 and 2012, comparing the absolute and single precision time measurements is summarized in Table 4.1. However, the source of approximately 0.400 ns limit in the improvement of the time resolution remains to be understood. We can only speculate that a combination of effects like pulse shape differences caused by loss of crystal transparency, fluctuations in the shower development in the crystals especially for energetic electromagnetic particles, about 0.100 ns differences arising from the differences in FE electronics de-synchronization among different electronics and phase shifts in the LHC clock phase lock by the QPLL. Additional studies are needed to fully understand and quantify the contributions from each of these sources.

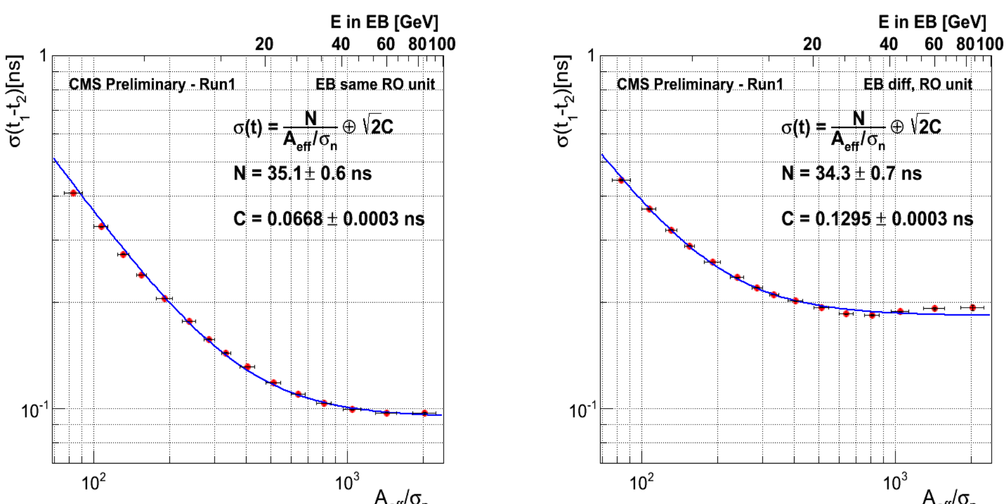

Figure 4.9: Timing resolution from: *left*: Two most energetic crystals in the same FE electronics, *right*: Two most energetic crystals belonging to different FE electronics, as a function of effective amplitude($A_{eff} = A_1A_2/\sqrt{A_1^2 + A_2^2}$) normalized to noise in EB. Both crystals are from reconstructed electrons in $Z \to e^-e^+$ events.

ECAL Timing Resolution

2011		
	Absolute Time $\sigma_{eff}(t_{seed})$[ps]	**Single Precision** $\sigma_{eff}(t_{e1} - t_{e2})$[ps]
EB	376	190
EE	356	282
2012		
	Absolute Time $\sigma_{eff}(t_{seed})$[ps]	**Single Precision** $\sigma_{eff}(t_{e1} - t_{e2})$[ps]
EB	340	164
EE	342	272

Table 4.1: ECAL timing resolution absolute time and single precision for 2011 and 2012 of LHC Run 1.

Chapter 5

Event Reconstruction

5.1 Event Reconstruction Overview

Event reconstruction is the process of reconstructing particles and their four momenta using raw data read from the electronics of the different CMS subdetectors. Event reconstruction is archived in CMS using the *Particle Flow* (PF) algorithm which reconstructs all the particles in an event, individually, using information from all CMS subdetectors. It is also possible to reconstruct particles without using the PF algorithm.

5.2 Supercluster Reconstruction

A clustering algorithm groups energy deposits from individual crystals to form clusters which are eventually grouped together forming clusters of clusters known as *superclusters*. A cluster is either a 3×3 or 5×5 crystals energy matrix. About 94% (97%) of the incident photon or electron energy is deposited in the 3×3 (5×5) crystal matrix in (η, ϕ) directions in the barrel and (x, y) directions in the endcaps.
The 3.8 T magnetic field and material in front of the calorimeter causes electrons and photons radiating off electrons to deposit their energy in a cluster of crystals spread in ϕ and because of the spread in ϕ, the clustering algorithms starts building clusters with a seed crystal (crystal with the maximum energy) and continues within a narrow window in η by summing the crystal energies along ϕ, which is the direction of the energy spread due to the magnetic field. Figure 5.1 is a schematic picture showing the direction (left

Figure) of the clustering process in (η, ϕ) directions in the barrel and the fraction (right Figure) of electromagnetic energy in a typical cluster.

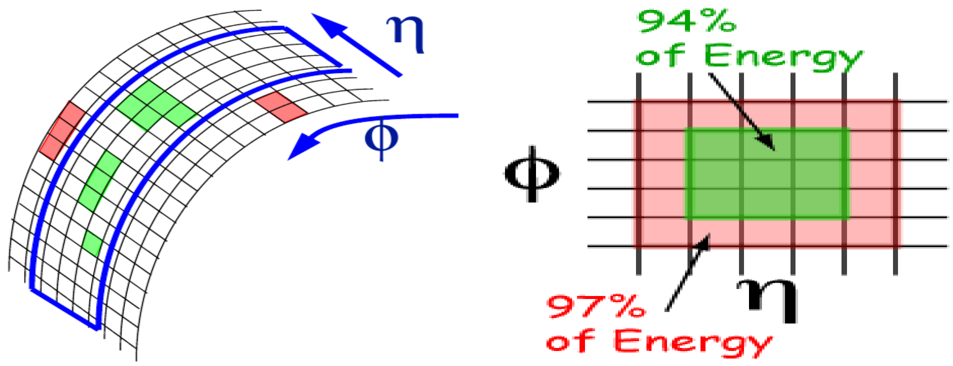

Figure 5.1: Superclustering algorithm direction (left) in the (η, ϕ) plane in EB and fraction (right) of electromagnetic shower energy coverage in a crystal energy matrix.

Two major clustering algorithms are used in ECAL: the *hybrid* (EB) and *island* (EE) algorithms.

- **Hybrid Supercluster Algorithm:** This algorithm is used for making super clusters in the barrel (EB). It takes advantage of the $\eta - \phi$ geometry of barrel crystals by taking a fixed 3 or 5 crystals in η and dynamically search and sum separate crystals energy along ϕ. The Hybrid algorithm takes advantage of the knowledge of the lateral shower shape along the η direction. The supercluster consists of basic clusters which are usually 3×3 crystals energy matrix.

- **Island Supercluster Algorithm:** This algorithm is used for making clusters in the endcap (EE). It begins by finding the seed crystal of the electromagnetic shower with maximum energy above a certain energy threshold. Using the seed crystal position, adjacent crystals are examined and added to a cluster until a rise in energy where a crystal belonging to another cluster or crystal that has no energy hit is reached. For each crystal to be added to the cluster, its energy read must be positive, it must not have been assigned to another cluster and the previous crystal added in the same direction must have a higher energy. These non-overlapping clusters (usually a 5×5 crystals energy matrix) finally form a supercluster.

5.3 Track and Vertex Reconstruction

The track of a charge particle is reconstructed using *hits* which are themselves reconstructed from the ionization left in silicon by the passage of the charge particle. The particle's helical trajectory or track, reconstructed from these hits, is used to measure the it's momentum and direction.

Track reconstruction uses several algorithms with the main algorithm used for reconstructing the tracks of charge particles produced from pp collisions called the *Combinatorial Track Finder* (CTF). The CTF integrates track fitting and pattern recognition, building tracks from an initial trajectory or seed while taking into account the energy loss and multiple-scattering between the tracker detector layers. It proceeds in three stages: seeding, finding and fitting.

During the seeding, initial trajectories (seeds) made of a pair of pixel hits that are compatible with the beam spot and have a lower p_{T} limit are used as possible candidates of the charge tracks. Pixel hits are the best track seeds while in the more forward region of the tracker detector, $2 < |\eta| < 2.5$, silicon pixel and inner strips hits are used for better track seeding.

The track finding stage uses a *Kalman Filter* pattern recognition approach (since the tracks can be described as a discrete dynamic *track state*, characterized by some given set of parameters and uncertainties, which is recursively updated one hit at a time on each layer) where, starting with the track parameters determined by the seeds, the track trajectory is extrapolated to outer neighboring tracker layers and compatible hits are assigned to the track.

In the fitting stage, the Kalman Filter algorithm (because the position information of the hit is updated to estimate the track parameters and uncertainties and the fitting process is repetitive) is again applied where each candidate track is fitted using least-squares fitting in two stages. The first stage avoids possible bias on the track parameters from the initial trajectories used in the seeding stage while the next stage yields the best estimates of the track parameters and uncertainties at the original vertex.

Other algorithms like the *iterative tracking algorithm* which is a general purpose tracking algorithm is used in association with customized CTF tracking algorithm to reconstruct the tracks of non-collisions events like cosmic and beam halo.

Similar to track reconstruction, vertex reconstruction involves two stages: vertex finding and vertex fitting. During vertex finding, a set of valid tracks from track reconstruction, represented by a list of track parameter vectors, is fed into a vertex finding algorithm which classifies the tracks into vertex candidates. The type of vertex finding algorithm used depends on whether it is finding a primary vertex (vertex where the particles are produced from the collision of the two proton beams) or secondary vertex (vertex where the particles are produced from the decay of an unstable particle) or the reconstruction of an exclusive particle decay.
The classified vertex candidates from vertex finding are fed into the vertex fitting algorithm. The output of the vertex fitting is a list of vertices, with each vertex having an estimated vertex position and a set of updated track parameter vectors. In vertex fitting, the best estimates of the vertex parameter, co-variance matrix, track parameter and the fit quality (chi-square, number of degrees of freedom, track weights) are used in distinguishing among a given set of tracks and their vertices.

5.4 Photon and Electron Reconstruction

Photons are reconstructed using superclusters and since they are neutral and do not leave tracks in the tracker, they are identified as superclusters in ECAL not associated to any tracks or reconstructed hits in the pixel tracker. The photon identification, beyond simply using the ECAL supercluster, is improved through several selection requirements using information from the tracker, ECAL, HCAL and the ratio of the photon candidate's energy deposited in HCAL to ECAL. Photons are supposed to deposit very little or no energy in HCAL and this is one of the main selection requirements to help distinguish photons from hadronic jets with high electromagnetic energy fraction which can easily be misidentified as photons.

For electron reconstruction, electron candidates are found when a supercluster is associated to a track reconstructed in the silicon tracker detector and in particular, its inner most layers (pixel hits). Electron reconstruction begins with a seeding approach which is either driven by ECAL or by the tracker. The ECAL driven seeding approach is very efficient for electrons with $p_{\mathrm{T}} > 10\,\mathrm{GeV}/c$. The track driven seeding approach uses a boosted decision tree to perform a pre-selection of the tracker clusters, in order to reduce fake electrons which are light hadrons with many hits in the tracker. Low-p_{T} electrons and non-isolated electrons (electrons embedded in jets) are reconstructed efficiently using the tracker driven seeded approach, since most of their energy is deposited in the tracker and very little in the ECAL, as they lose most of their energy through multiple scattering before they reach ECAL. When fitting the electron tracks, we must account for the different energy loss mechanisms of the electron compared to other charged particles. Since electrons lose most of their energy by radiating photons (*bremsstrahlung*, which is non-Gaussian in nature, the *Gaussian Sum Filter* algorithm (combination of several Gaussians) is used to provide good estimate of the track momentum both at the ECAL surface and at the interaction point.

5.5 Muon Reconstruction

Muon tracks are reconstructed using the all-silicon inner tracker (tracker tracks) and the muon system (standalone tracks). The standalone tracks are reconstructed using reconstructed positions (hits) in the muon system consisting of the Drift Tubes (DT) in the barrel ($|\eta| < 0.9$), Cathode Strip Chambers (CSC) in the endcaps ($1.2 < |\eta| < 2.4$) and Resistive Plate Chambers (RPC) in the overlap region ($0.9 < |\eta| < 1.2$). There are two independent muon reconstruction approaches: *Global muon reconstruction (Outside-in)* and *Tracker muon reconstruction (Inside-out)*. For Global muon reconstruction, each standalone-muon track is matched to a tracker track by comparing the parameters of the two tracks propagated to a common surface. The global muon track is fitted combining hits from the tracker track and standalone-muon track using the Kalman-filter algorithm. For the tracker muon reconstruction, all tracks with $p_{\mathrm{T}} > 0.5\,\mathrm{GeV}/c$ and total momentum $p > 2.5\,\mathrm{GeV}/c$ are considered as possible muon candidates and are extrapolated to the muon system taking into consideration the magnetic fields, the average expected energy loss in the calorimeters and multiple Coulomb scattering in the detector material to locally reconstruct segments in the muon system. A combination of different muon algorithms depending on the muon p_{T}, provides a robust and efficient muon identification.

Using the beam spot as constraint for the muon's vertex, we can distinguish between muons produced from pp collisions from *cosmic muons* and *beam halo muons* (muons produced from the interaction of the proton beam with the gas in the beam pipe). Figure 5.2 show an illustration of the trajectories of different muon sources interacting with the CMS detector.

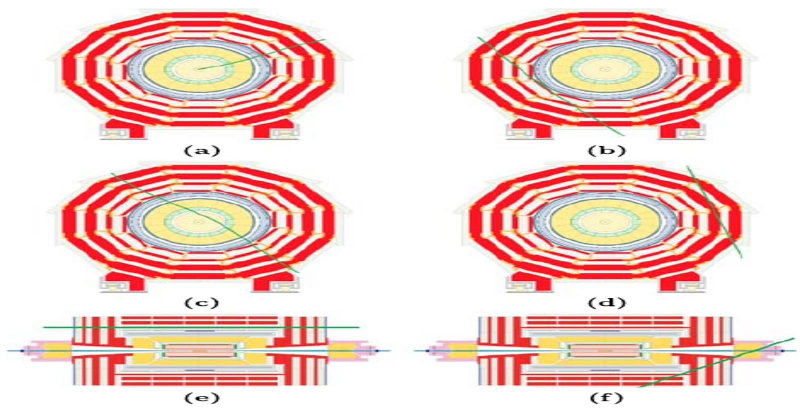

Figure 5.2: Illustration of muons from proton-proton collision, cosmic rays and beam halo. (a) Muons from collision propagating from the center and moving outwards, (b) Cosmic muons traveling through the detector leaving signals in opposite hemispheres of the muon system, (c) Cosmic muons leaving signals in the tracker and opposite hemispheres, (d) cosmic muons entering and leaving the detector without passing through the muon detector layers, (e) beam halo muons penetrating the detector and leaving signals in the endcaps and (f) Cosmic muons entering the detector through the endcap (EE) and leaving through the barrel (EB). This can happen in the reverse way; EB to EE.

5.6 Particle Flow Algorithm

The *Particle Flow* (PF) algorithm is an algorithm for reconstructing particles using detector information from the tracker, ECAL, HCAL and muon chambers of the CMS detector [48, 49]. It uses a combination of different algorithms comprising of calorimeter clustering, tracking and extrapolation to calorimeters, muon identification, electron pre-identification and linking local reconstructed elements, for reconstructing a list of particles which include photons, charge hadrons, neutral hadrons, muons and electrons. The same list of particles is subsequently used to reconstruct composite “particles” like jets, $E_{\mathrm{T}}^{\mathrm{miss}}$ and taus. The versatility of the PF algorithm is the reason why it was introduced for reconstructing Jets and missing transverse energy ($E_{\mathrm{T}}^{\mathrm{miss}}$), where complete information of the event content from every subdetector is needed for best performance.

The PF algorithm uses tracks, electron energy seeds, 4-momentum, super cluster energy calibration, bremsstrahlung tracks for electron and photon reconstruction making it extremely efficient at minimizing electron and photon misidentification. For $E_{\mathrm{T}}^{\mathrm{miss}}$ reconstruction where full reconstruction of all the particles belonging to an event is necessary, the PF algorithm is very reliable.

5.7 Jet Reconstruction

A jet is a spray of particles arising from the hadronization of colored particles. Because jets are made of many particles like hadrons and photons from π^0 decay, they are best reconstructed using the particle flow algorithm. Jets reconstructed using the PF algorithm are called *PF-Jets*.

Using calorimeter towers as input, jets can be reconstructed using the Anti-k_T clustering algorithm which combines four vectors according to their relative transverse momentum (p_{T}) within a standard cone size of $\Delta R = 0.5$ in the (η, ϕ) plane, where, $\Delta R = \sqrt{\Delta\eta^2 + \Delta\phi^2}$.

The quality of a reconstructed jet depends on a set of selection variables collectively referred to as the *JetID*. The JetID consist of variables which selects on jets candidate base on the composition of the jets. The jet composition can be described using the following quantities: electromagnetic energy fraction (EMF), the charge hadron fraction (CHF), the neutral hadron fraction (NHF), the charge electromagnetic fraction (CEF), neutral electromagnetic fraction (NEF) the number of calorimeter cells containing more than 90% of jet energy (N_{jet}^{90}), the fraction of jet energy in the hottest Hybrid photodetector (HPD) unit in HCAL readout within a jet (f_{HPD}) and the η region of the jet. The selection threshold and combination of jetID variables used will depend on a specific analysis and the type of jets involved. In general, jet candidates are required to have an electromagnetic energy fraction (EMF) more than 10% i.e. $EMF > 0.01$, must be within the ECAL fiducial region of $|\eta| < 2.6$, the number of calorimeter cells containing more than 90% of jet energy (N_{jet}^{90}) must be > 1, the fraction of jet energy in the hottest Hybrid photodetector (HPD) unit in HCAL readout within a jet (f_{HPD}) must be > 0.98, the charge hadron fraction (CHF)> 0.0 if within $|\eta| < 2.4$, the neutral hadron fraction (NHF)< 1.0 , the charge electromagnetic fraction (CEF) < 1.0, and neutral electromagnetic fraction (NEF) < 1.0. These jetID selection requirements have been shown to remove mis-reconstructed jets arising from spurious energy deposition in subdetectors with good efficiency [50].

The jet energy is often mis-measured due to non-linear responses in the calorimeters as the hadronic shower develops, cracks in the detector and additional energy from events with PU. The jet energy is corrected for contributions from the above sources through *Jet Energy Corrections* (JEC) measurements [51]. Applying these corrections during reconstruction guarantee a reliable measurement of the jet energy , however, JEC is one of the sources of uncertainties in most analysis which involve jets.

5.8 Missing Transverse Energy Reconstruction

Missing Transverse Energy is defined as the negative vector sum of the transverse energy deposits of all the particle candidates in an event, including the JEC. Its magnitude, $E_{\mathrm{T}}^{\mathrm{miss}}$ is given as

$$E_{\mathrm{T}}^{\mathrm{miss}} = |-\sum_{n}(E_n \sin\theta_n \cos\theta_n \hat{\mathbf{i}} + E_n \sin\theta_n \sin\theta_n \hat{\mathbf{j}})| = |\not{E}_{\mathrm{T}}^{x}\hat{\mathbf{i}} + \not{E}_{\mathrm{T}}^{y}\hat{\mathbf{j}}| \tag{5.1}$$

Where, n is the sum over all calorimeter energy deposits including energy deposits in towers, reconstructed energies (hits) or generator level particle energies. $E_{\mathrm{T}}^{\mathrm{miss}}$ is use to infer the presence of a particle which escaped the CMS detector like neutrinos (ν), neutralinos ($\widetilde{\chi}_1^0$) and gravitino ($\tilde{G}$).

In order to measure $E_{\mathrm{T}}^{\mathrm{miss}}$ accurately, a particle detector should be nearly hemetic i.e. have a 4π solid angle coverage, to allow for complete measurement of the transverse momentum of all the particles belonging to an event. The hadronic forward (HF) subdetector of the CMS detector, with little space allowing for the passage of the proton beams, provide this near 4π solid angle.

Measuring $E_{\mathrm{T}}^{\mathrm{miss}}$ is always challenging and is a source of uncertainty in most analysis which involve $E_{\mathrm{T}}^{\mathrm{miss}}$ as machine induced background processes, mis-measured energy of and from mis-reconstructed particles and anomalous signals like spike can contribute to the measurement of $E_{\mathrm{T}}^{\mathrm{miss}}$. By minimizing the contributions from these processes we can measure $E_{\mathrm{T}}^{\mathrm{miss}}$ better [52, 53].

The use of $E_{\mathrm{T}}^{\mathrm{miss}}$ in event selection is common in most analysis which involves the search for new phenomena which is a common prediction in models Beyond Standard Model (BSM) like *supersymmetry*. The presence of large $E_{\mathrm{T}}^{\mathrm{miss}}$ in an event indicates the presence of a new particle not described by standard model interactions which usually have small $E_{\mathrm{T}}^{\mathrm{miss}}$ as in the case of the neutrino in the W boson decay, $\mathrm{W} \rightarrow \mathrm{e} + \overline{\nu}$.

5.9 Anomalous Signals

Sometimes anomalously large signals called "*spikes*" are produced when neutrons or charged hadrons like protons strike directly, ionizing the silicon of the photodiode producing an electronic signal even in the absence of any crystal scintillation.
Because spike signals are not produced through the crystal scintillation process, which takes about 10 ns, their measured arrival time is early and negative. Energy deposits from spikes range from a few GeV to the saturation energy of ECAL which is about 1.7 TeV. Since they are not due to showering particles, most often only one isolated crystal sees such energy. Spikes may occasionally have positive time, appearing late or delayed in their arrival time at ECAL, and populating the tails of the photon's rechit time distribution. The late arrival time may be due to the slow propagation (takes an indirect route) of neutrons through the CMS detector.

Numerous test beam, collision data and simulation studies [54, 55], have been carried out towards understanding the properties of events with spikes and how they can be tagged and removed. These studies reveal that most spikes can be identified using a topological energy sharing variable called "*Swiss-Cross*" (SX) constructed as $1 - \frac{E_4}{E_1}$. E_1 is the energy deposit of the central (highest energy) crystal and E_4 is the sum total of the energy of the neighboring four crystals in the (η, ϕ) plane. A selection cut SX > 0.95 rejects more than 99% of isolated spikes with transverse energy greater than 10 GeV with very little impact on the efficiency of selecting electromagnetic (EM) showers. Other topological energy sharing variables like $1 - \frac{E_6}{E_2}$ and $1 - \frac{E_9}{E_2}$, where E_2 is the sum of the energy of two crystals sharing the energy deposited from simultaneous spikes and $E_6(E_9)$ is the sum of the neighboring 6(pairs-of)(9) crystals in the (η, ϕ) plane. The $1 - \frac{E_6}{E_2}$ variable is used to identify isolated spikes whose energy deposit spread in two adjacent crystals while the $1 - \frac{E_2}{E_9}$ is used to identify non-isolated spikes i.e. spikes which are found embedded in a supercluster.

It has also been shown that applying selection cuts on the rechit time of ± 3 ns leads to more than 90% efficiency for rejecting spikes. However, in this thesis, we do not require such selection cuts on the rechit time as these rechits include rechits of possible delayed electromagnetic particles produced during *pp* collisions with arrival time beyond 3 ns.

Chapter 6

Search for Long-Lived Neutral Particles

6.1 Analysis Strategy

A search for events with at least a single late arrival time photon at the Electromagnetic Calorimeter (ECAL) and large missing transverse energy ($E_{\mathrm{T}}^{\mathrm{miss}}$) is described. The search uses a counting method, in which an excess number of events with photon time above a timing threshold to the expected number of background events, hint at the presence of a new physics phenomena. Such a phenomena is expressed through the decay of a Long-Lived Neutral Particle (LLNP) into a late photon and large $E_{\mathrm{T}}^{\mathrm{miss}}$, which is not common with standard model interactions. We expect most of the background events to arise from non-collision rather than proton-proton (pp) collision events.

6.1.1 Signal and Background Events

The late photon (γ) and large missing transverse momentum ($E_{\mathrm{T}}^{\mathrm{miss}}$) are from the decay of the lightest neutralino ($\widetilde{\chi}_1^0$), i.e. $\widetilde{\chi}_1^0 \to \gamma + \tilde{G}$, which serves as the LLNP. Because the $\widetilde{\chi}_1^0$ is produced indirectly through the the cascade decay of heavier sypersymmetric particles like gluino ($\widetilde{\mathrm{g}}$) or squark ($\widetilde{q}$), i.e. gg $\to \widetilde{\mathrm{g}}\widetilde{\mathrm{g}} \to q\overline{q}q\overline{q}\widetilde{\chi}_1^0\widetilde{\chi}_1^0$ or $q\overline{q} \to \widetilde{q}\overline{\widetilde{q}} \to \overline{q}q\widetilde{\chi}_1^0\widetilde{\chi}_1^0$, in addition to the late photon and large $E_{\mathrm{T}}^{\mathrm{miss}}$, the signal event topology includes multiple hiph-p_{T} jets. The large $E_{\mathrm{T}}^{\mathrm{miss}}$ is due to the undetected gravitino ($\tilde{G}$) at the CMS detector. We, thus expect a typical signal event to comprise of at least one late high-p_{T} photon, large $E_{\mathrm{T}}^{\mathrm{miss}}$ and multiple high-p_{T} jets. Such an event composition is not expected of standard model events. The multiple high-p_{T} jets also provide an added handle in the event selection to help suppress background events with no jets.

Our background events are events from either pp collisions or non-collisions which mimic the late photon, large $E_{\mathrm{T}}^{\mathrm{miss}}$ and multiple jets signal.
The non-collision background events include the so-called *Beam Induced Backgrounds* or beam halo, cosmic rays and spikes. Most of these events have a late high-p_{T} photon and large $E_{\mathrm{T}}^{\mathrm{miss}}$.
Collision background events can mimic the $\widetilde{\chi}_1^0$ decay signal producing late photons and large $E_{\mathrm{T}}^{\mathrm{miss}}$ in cases where the photon time and/or $E_{\mathrm{T}}^{\mathrm{miss}}$ are mis-measured. Other collision events might have real $E_{\mathrm{T}}^{\mathrm{miss}}$ and a misidentified photon object. For example, inclusive Z+jets/W+jets events, inclusive top-anti-top ($t\bar{t}$)+jets events and inclusive ZZ/WW/WZ+jets events can have true $E_{\mathrm{T}}^{\mathrm{miss}}$ through the $\mathrm{Z} \rightarrow \nu\bar{\nu}$ and $\mathrm{W} \rightarrow \mathrm{e}\bar{\nu}_{\mathrm{e}}$ decays, where the undetected neutrino (ν) give rise to $E_{\mathrm{T}}^{\mathrm{miss}}$. Multijets and QCD events, on the other hand, give rise to fake $E_{\mathrm{T}}^{\mathrm{miss}}$ (instrumental $E_{\mathrm{T}}^{\mathrm{miss}}$), where there is no undetected particle pertaining to the event but rather $E_{\mathrm{T}}^{\mathrm{miss}}$ arising because of poor reconstruction of the energy of particles. The late photon arises when one of the jets or an electron is misidentified as a photon and it's ECAL time is mis-measured. The other jets in the event satisfy the high-p_{T} multiple jets requirement.

6.1.2 Samples

Datasets

The data sample we use for this search contain events passing the HLT trigger with at least one photon. These events were produced during LHC Run 1 in 2012 of pp collisions at the center of mass energy, $\sqrt{S} = 8\,\mathrm{TeV}$. The data is equivalent to a total integrated luminosity of 19.1 fb^{-1} recorded by the CMS detector.

Monte Carlo Samples

The MC samples were produced with *Summer 2012* prescription of the calibration and alignment status of the CMS detector and pile up conditions at 8 TeV.

The GMSB SPS8 signal samples have 50,000 events for each mean lifetime ($c\tau$) and effective SUSY breaking scale ($\mathbf{\Lambda}$) or mass of $\widetilde{\chi}_1^0$ ($m_{\widetilde{\chi}_1^0}$). These samples are produced for different $c\tau$ ranging from 50 cm to 1000 cm for each $\mathbf{\Lambda}$ or $m_{\widetilde{\chi}_1^0}$ point. We vary $\mathbf{\Lambda}$ from 100 TeV to 220 TeV which is equivalent to $m_{\widetilde{\chi}_1^0}$ ranging from 139 GeV/c^2 to 314 GeV/c^2. Table 6.1 shows a summary of our signal MC samples used in this analysis. For each sample, the number of events, cross-section and branching ratio for $\widetilde{\chi}_1^0$ production and decay to γ and $\tilde{G}$ for each SUSY breaking scale is also given.

The γ+jet MC samples were generated for different momentum of the photon with respect to the colliding partons and normalized to the 19.1 fb^{-1} of integrated luminosity. The cross-sections, p_{T} of the photon ($\hat{p_{\mathrm{T}}}$) radiated by the colliding parton and the number of events in each sample is summarized in Table 6.2. The $\hat{p_{\mathrm{T}}}$ range is from 50 GeV/c to 800 GeV/c.

Λ [TeV]	$c\tau$ (mm)	σ_{LO} (pb)	**Number of Events**	**Branching Ratio**
100	500-10,000	0.368	50,000	0.9444
120	500-10,000	0.133	50,000	0.9042
140	500-10,000	0.0574	50,000	0.8711
160	500-10,000	0.0277	50,000	0.8464
180	500-10,000	0.0145	50,000	0.8282
220	500-10,000	0.0044	50,000	0.8282

Table 6.1: Signal GMSB SPS8 Monte Carlo samples for different $\mathbf{\Lambda}$ with 50 cm $<$ $c\tau <$ 1000 cm and Branching Ratios (BR).

$\hat{p_{\mathrm{T}}}$	σ_{LO} (pb)	**Number of Events**
$50 \sim 80$	3322.3	1995062
$80 \sim 120$	558.3	1992627
$120 \sim 170$	108.0	2000043
$170 \sim 300$	30.1	2000069
$300 \sim 470$	2.1	2000130
$470 \sim 800$	0.212	1975231

Table 6.2: The $\gamma+$ jets samples for $\hat{p_{\mathrm{T}}}$ from 50 GeV/c to 800 GeV/c

6.2 ECAL Timing

In this section, we describe how the photon arrival time is measured and the adjustments we made on the MC time so that it captures the same conditions as data. We discuss the ghost/satellite proton bunches and argue that they are a possible background source to late photons.

6.2.1 Photon Time Measurement

The electromagnetic shower of a photon spreads across several crystals, and as a result, the photon's energy and time measurements are read from several crystals belonging to the photon's supercluster, which contains all of its energy. The presence of anomalous signals from spikes, noisy crystals and pile-up events, demand a robust method for measuring the photon arrival time at ECAL, and since the photon's ECAL time is our main observable for distinguishing background from signal events, we employ a method, which is capable of reducing timing bias that could arise from such anomalous signals, for measuring the photon's arrival time.

Using the photon's supercluster, the photon's arrival time at ECAL can be defined using either the reconstructed time (t_{reco}) of a single crystal which is the *seed crystal* (crystal with the highest energy deposit), or a weighted average time calculated using the reconstructed time and its uncertainty, of each crystal of the photon's supercluster. We write, t_{seed}, for the seed time and, t_{Ave}, for the average time defined as

$$t_{Ave} = \frac{\sum_{i=1}^{N} \frac{t_{reco}^{i}}{\sigma_i^2}}{\sum_{i=1}^{N} \frac{1}{\sigma_i^2}}, \tag{6.1}$$

where, N is the total number of crystals of the supercluster, $t_{reco,i}$ and σ_i are the time and uncertainty on the reconstructed time of each crystal, respectively. Figure 6.1 shows a comparison of the seed time, t_{seed}, and the average time, t_{Ave}, to be the photon ECAL time. Both distributions are normalized to total number of events.

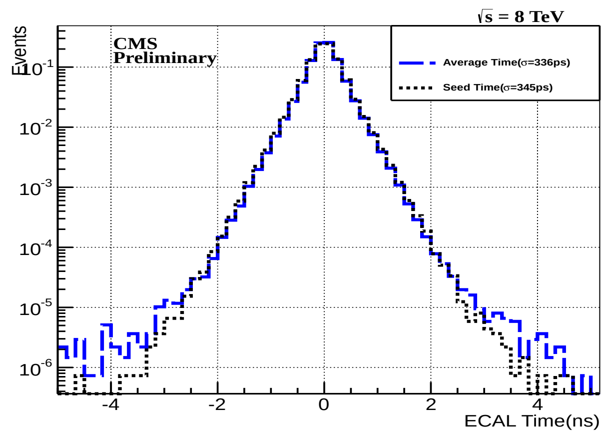

Figure 6.1: Seed (black) and Average (blue) times as the measured photon time.

The width (σ) of both Gaussian distributions are similar. We observed $\sigma = 345$ ps for the seed time compared to $\sigma = 336$ ps for the average time. The average time is susceptible to timing bias. For example, if one or more of the crystals in the supercluster is poorly time calibrated or embedded with a spike, the photon time, because of the spike or mismeasured time from a single crystal, can be very biased.
In this analysis, we use the seed time for the photon's arrival time in ECAL and also use the χ^2 computed using the average time to identify photons with anomalous signals like spikes.

The χ^2 on the average time is computed as

$$\chi^2 = \sum_{i=0}^{N} \frac{(t^i_{reco} - t_{Ave})^2}{\sigma_i^2} \tag{6.2}$$

where, N is the number of crystals in the photon supercluster, t^i_{reco} and σ_i, are the time and uncertainty for each crystal, and t_{Ave}, is the mean time defined in Equation 6.1. The χ^2 can be used to distinguish spikes from true photons. A distribution of the normalized χ^2 against the photon ECAL time is shown in Figure 6.2. Spikes misidentified as photons have large values of χ^2 and usually have large negative ECAl time.

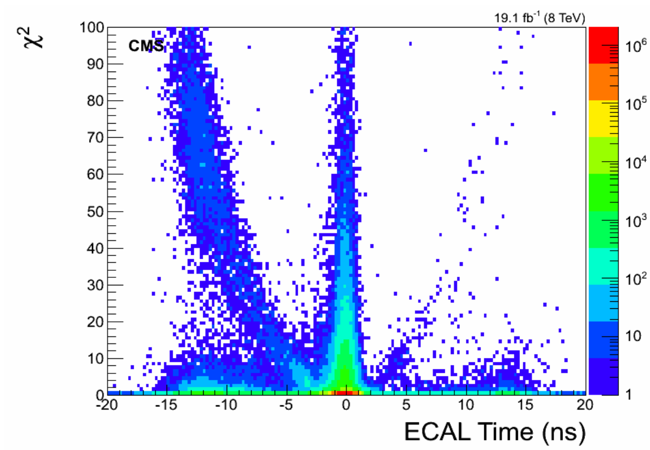

Figure 6.2: The χ^2 Vs photon ECAL time plot showing spikes misidentified as photons have very large χ^2 and negative ECAL time. The region of $\chi^2 > 4$ is mostly dominated by spikes events.

From the χ^2 Vs ECAL time plot (Figure 6.2), we observe that, most of the true photons have ECAL time around zero, but, there are many photons with large ECAL time which equally have large normalized χ^2 values. We expect large χ^2 values in cases where the time measurements from non-seeded crystals is inconsistent with the time measurement from the seed crystal. We also observe that, a cut in $\chi^2 < 4$, can reduce with 99.2% efficiency, photon contributions from spikes (where a neutron, embedded in a jet, hits directly the photo-detectors and produces a spike) and photons with mis-measured ECAL time.

Monte Carlo Time

It is challenging to properly simulate ECAL time for MC events so that it captures the conditions of the ECAL detector during data recording. As a result, the mean time and root mean squared (RMS) from MC events does not agree with those in data. We account for this disagreement by shifting the mean time and smearing the RMS, by an additional Gaussian convolution, on the photon time of MC events so that it matches the mean time and RMS of data. The amount of shifting and smearing required is obtained using selected 1 or 2 jets events. To ensure that true photon events are used, we select 1 or 2 jets events with in-time photons, $|t_\gamma| < 2$ ns, with photon $p_{\mathrm{T}} > 80\,\mathrm{GeV}$, for both data and MC γ+jets samples. Shown in Figure 6.3, is the in-time photon time distributions for data and MC γ+jets samples before (left plot) and after (right plot) the mean time shifting and RMS smearing were done on the photon time of MC γ+jets events. We see good agreement in MC and data photon time after the mean time shifting and RMS smearing on the MC is done.

6.2.2 Satellite Bunches

Ghost/Satellite proton bunches trail the main proton bunche at the LHC with a time spacing of 2.5 ns. These ghost/satellite bunches are the source of Beam halo-induced photons produced observed in ECAL. Figure 6.4 shows the photon time for photons with $p_{\mathrm{T}} > 50\,\mathrm{GeV}/c$ in ECAL. The 2.5 ns discrete pattern in the photon ECAL time confirm the presence of ghost/satellite beam halo-induce photons. Because of the beam intensity, most of these out-of-time photons are in the endcap ($1.47 < \eta < 3.0$) with a few in the barrel ($|\eta| < 1.47$). We consider halo-induced photons a major background to late photons.

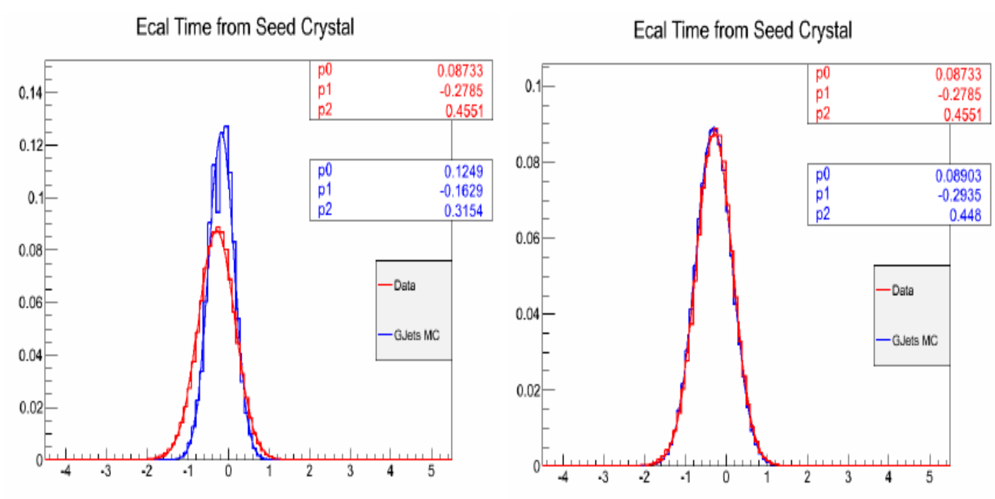

Figure 6.3: ECAL time distributions of in-time photons from MC $\gamma+$ jets (blue) and data (red) samples before (left) and after (right) we adjusted the photon time from MC.

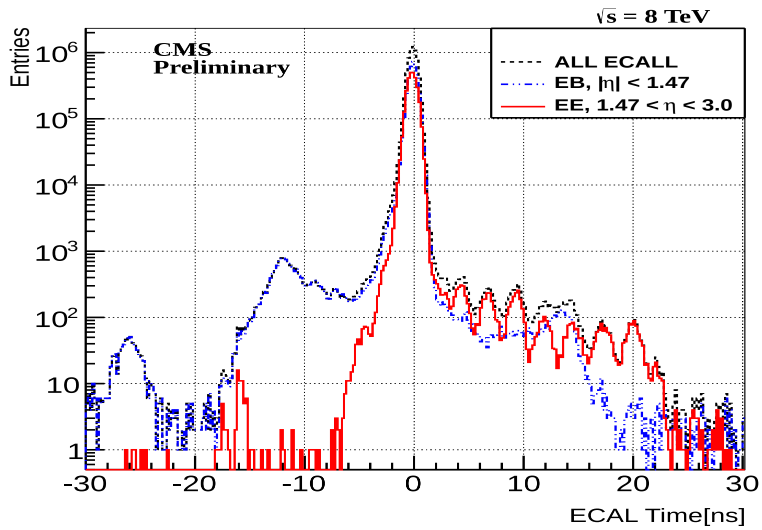

Figure 6.4: ECAL timing distribution of photons in barrel (EB), endcap (EE) and all of ECAL (ALL ECAL) with $p_T > 50$ GeV from data. A 2.5 ns delay timing structure is observed in endcaps.

6.2.3 E_T^{miss} Adjustments

In the formation of energy clusters, which are used for event reconstruction by the particle flow (PF) algorithm, "out-of-time" energy deposits in ECAL are excluded. The reason is because, the PF algorithm avoids energy deposits from particles which are not produced from the main proton-proton bunch collisions, like cosmic muons and machine-induced backgrounds, as these are normally out-of-time. Because of the exclusion, the out-of-time photon's transverse energy, E_T, is not included in the calculation of missing transverse energy or $\not{E}_T$ (from now on, we will be using for convenience, $\not{E}_T$ instead of E_T^{miss} as the symbol for missing transverse energy) of the event. This exclusion introduces some differences in the calculation of $\not{E}_T$ for in-time ($|t_\gamma| < 3.0$ ns) and for out-of-time photon events.

Since the energy deposits from events with out-of-time photons could be from a possible signal event, and we are searching for events with late arrival time photons, we correct for the E_T exclusion, by adding back the out-of-time photon's E_T vector to the particle flow reconstructed $\not{E}_T$ (PF-MET) vector, for events with out-of-time photons. We avoid any bias in our event selection, particularly for events with out-of-time photons, by introducing an additional missing transverse energy variable defined as $\vec{\not\!\!E}^{\gamma}_{\mathrm{T}} = \vec{\not\!\!E}_{\mathrm{T}} + \vec{E}_{\mathrm{T}}$, which we use in our final event selection.

6.3 Event Selection

Our event selection happens in two stages. The first stage, consisting of L1 trigger at online and an HLT software trigger of multiple selection modules, selects only triggered single photon events. The second stage happens offline, where, our signal-like event selection requirements are applied.

The offline event selection criteria is designed to select signal-like events whose event topology comprise of at least a single photon, multiple jets and large $\not\!\!E_{\mathrm{T}}$. The multiple jets arise from the cascade decay of gluino or squark to other quarks or gluons, in addition to the lightest neutralino. We require multiple jets in our event selection as part of the signal event topology, but, also as a way of suppressing non-collision background events like cosmic and beam halo muons, which are usually not associated with jets.

Collision background events like multijets and QCD events, where a jet can be misidentified as a photon, are equally suppressed by selecting purely hadronic jets i.e. jets containing a greater portion of hadronic energy fraction from pions and kaons.

The single late photon and large $\not\!\!E_{\mathrm{T}}$ is from $\widetilde{\chi}^0_1 \to \gamma + \tilde{G}$ decay and we select only photons in the barrel ($|\eta_\gamma| < 1.479$) with high transverse momentum. This suppresses out-of-time photons from the so-called halo-induced photons produced by ghost/satellite proton bunches. The high-p_{T} photon requirement also helps suppress out-of-time photons due to timing mismeasurements of photons from QCD and multiple jets events.

The large $\not\!\!E_{\mathrm{T}}$ requirement is useful for suppressing γ+jets and QCD events with apparent $\not\!\!E_{\mathrm{T}}$ or *fake* $\not\!\!E_{\mathrm{T}}$ which arise from energy misreconstruction and cracks in the detector. Out-of-time photon contribution from spikes is also reduced by applying electromagnetic shower shape selection on S_{Minor} at the HLT trigger level.

6.3.1 Trigger Selection

During the online event selection, only events passing our online higher level trigger (HLT): `HLT_DisplacedPhoton65_CaloIdVL_IsoL_PFMET25`, which is seeded by a L1 trigger: HLT_L1SingleEG12, are accepted. The HLT trigger is a combination of selection modules triggering events with at least one calorimeter identification standards of a very loose isolated photon with p_{T} of atleast $65\,\mathrm{GeV}/c$ and $\not\!\!E_{\mathrm{T}}$ (without any out-of-time energy deposit bias) above $25\,\mathrm{GeV}$. The minor axis of the photon electromagnetic shower must not spread across many crystals in any direction. This is implemented as $0.1 < S_{Minor} < 0.4$ of the photon.

We study the HLT trigger efficiency and turn-on (efficiency becomes nearly 100%) curve separately for the photon p_{T} and event $\not\!\!E_{\mathrm{T}}$, using, as the denominator of the event ratio events with at least one jet and a photon also triggered by the HLT trigger: HLT_Photon50_CaloIdVL_IsoL. This trigger selects events with photon candidates also satisfying the calorimeter identification standards of a very loose isolated photon with p_{T} of at least $50\,\mathrm{GeV}/c$. The HLT event selection efficiency in p_{T} is defined as the fraction of events passing our HLT trigger to events with at least one jet and a photon triggered by the HLT_Photon50_CaloIdVL_IsoL trigger within $\Delta R < 0.5$, while the efficiency in $\not\!\!E_{\mathrm{T}}$ is defined as the ratio of events passing our HLT trigger (HLT_DisplacedPhoton65_CaloIdVL_IsoL_PFMET25) over events with at least one jet and a photon passing the HLT_Photon50_CaloIdVL_IsoL trigger, with no $\not\!\!E_{\mathrm{T}}$ selection cut applied. Photons selected by both triggers must also satisfy the loose selection cuts, excluding the photon p_{T} and $\not\!\!E_{\mathrm{T}}$ selection cuts, of our offline photon selection requirement summarized in Table 6.3.

The results of the trigger efficiency measurements in photon p_{T} and event $\not\!\!E_{\mathrm{T}}$ shown in Figure 6.5, indicate that the event selection efficiency is 100% for events with photon $p_{\mathrm{T}} > 80\,\mathrm{GeV}/c$ and $\not\!\!E_{\mathrm{T}} > 60\,\mathrm{GeV}$. The slight difference between the γ+jets (black) and the GMSB (red) MC samples is because the events in γ+jets samples have no real $\not\!\!E_{\mathrm{T}}$, and it is difficult to simulate apparent or fake ($\not\!\!E_{\mathrm{T}}$ from detector crack and unclustered energy deposits) $\not\!\!E_{\mathrm{T}}$ in MC simulation.

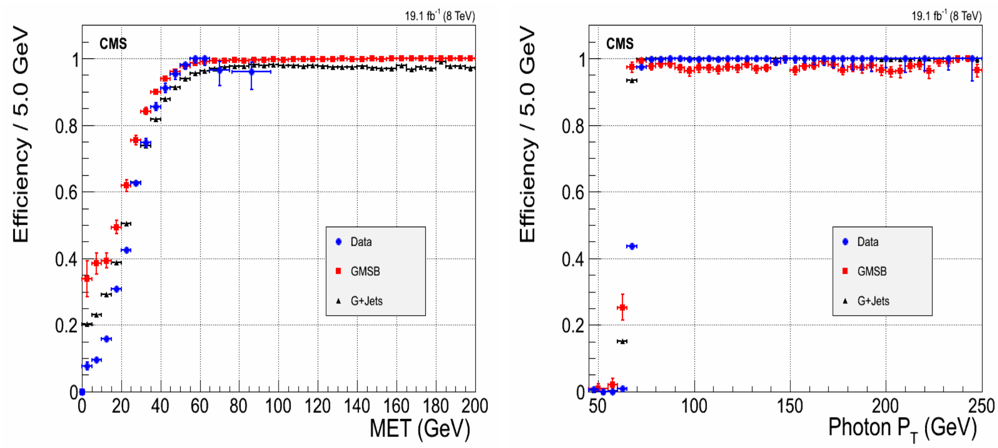

Figure 6.5: Our HLT trigger efficiency turn-on curves in event $\not{E}_{\mathrm{T}}$ (left) and photon p_{T} (right).The γ+jets samples require photon $p_{\mathrm{T}} > 170$ GeV/c.

6.3.2 Offline Selection

Our offline event selection, applied on the HLT triggered single photon events, require that the leading photon have $p_{\mathrm{T}} > 80\,\mathrm{GeV}/c$ and if the event has more than one photon, the sub-leading photon have $p_{\mathrm{T}} > 45\,\mathrm{GeV}/c$. Electromagnetic showers initiated by charged hadrons are rejected by requiring $E^{\mathrm{HCAL}}/E^{\gamma} < 0.05$, where E^{HCAL}, is the sum of the energy in the HCAL towers directly behind the ECAL photon supercluster within a $\Delta R < 0.15$, with $\Delta R = \sqrt{(\eta - \eta^{\gamma})^2 + (\phi - \phi^{\gamma})^2}$, and E^{γ} is the photon energy in ECAL.

Electrons are rejected by requiring the absence of hits in the first two layers of the pixel detector that is consistent with an electron track matching the observed location and energy of the photon candidate (this is known as pixel veto requirement).

The photon candidates must satisfy three *isolation* requirements that reject photons produced in hadronic decays:(1) $Iso_{\mathrm{TRK}} < 0.2\,\mathrm{GeV}$, where Iso_{TRK}, is the sum of the p_{T} of tracks compatible with the primary event vertex in an annulus $0.015 < \Delta R < 0.40$, excluding a strip half η width of 0.015 and the additional inner cone of size 0.04, optimized to exclude reconstructed tracks from $\mathrm{Z} \to e^{+}e^{-}$ events, centered around the line of vertex pointing to the photon supercluster. The exclusion is to remove the photon's own energy if it converts into an $e^{+}e^{-}$ pair; (2) $Iso_{\mathrm{ECAL}} < 4.5\,\mathrm{GeV}$, where Iso_{ECAL}, is the transverse energy deposited in ECAL in an annulus $0.045 < \Delta R < 0.4$, centered around the photon ECAL supercluster, excluding the strip half η width of 0.02 and the additional inner cone of size 0.045 centered around the ECAL supercluster position; (3) $Iso_{\mathrm{HCAL}} < 4.0\,\mathrm{GeV}$, where Iso_{HCAL} , is the transverse energy of HCAL tower in an annulus of $0.15 < \Delta R < 0.40$, centered about the ECAL supercluster position. If the photon is very closed to a track within a range in $\Delta R(\gamma, track) < 0.6$, it is rejected. This is to avoid misidentifying charge particles as photons and to prevent double counting jets with high electromagnetic energy component as photons. The photon must also be isolated from any other particle in a cone size of $\Delta R(\gamma, \mathrm{particle}) < 0.4$. The size of the photon electromagnetic shower along the minor axis (S_{Minor}) must be be within 0.12 to suppress photons embedded in hadronic jets.

Only photons belonging to the barrel (EB) region i.e. $|\eta_\gamma| < 1.479$, are accepted, to avoid many out-of-time halo-induced photon candidates from ghost/satellite proton bunches, which belong to the endcap (EE) shown in Figure 6.4, and also since not many signal out-of-time photons go into the endcap.

Topological selection cuts, $1 - E_6/E_2 < 0.98$ and $1 - E_4/E_1 < 0.98$, on the photon energy deposit, help suppress spikes which are caused by the direct interaction of the ECAL APDs by charged particles and neutrons producing anomalous photon signal. A summary of our full photon selection criteria is presented in Table 6.3.

For jets, we select jets with $\eta_{jet} < 2.4$, and require that the leading jet in the event has a $p_{\mathrm{T}} > 35\,\mathrm{GeV}/c$ with the event having at least 1 jet. This helps suppress non-collision background events without jets. The jets are reconstructed using the PF algorithm and identified based on the identification selection criteria summarized in Table 6.4, where a jet candidate must satisfy the following: the Charge Electromagnetic Fraction (CHF) and the Neutral Electromagnetic Fraction (NEF) must make up a greater portion of the jet sub-structure ($> 99\%$), the Neutral Energy Fraction (NEF) must smaller than 99%, in order that the jet is not easily misidentified as a photon. A jet near a photon object within a cone of 0.3 is rejected.

From our HLT trigger event selection efficiency plot in Missing Transverse Energy (MET) shown in Figure 6.5, and in order to suppress most of the background events with out-of-time photons, we observed that a missing transverse energy of at least $60\,\mathrm{GeV}$ for $\not{E}_{\mathrm{T}}$ and $\not{E}_{\mathrm{T}}^{\gamma}$ is enough to suppress γ+jets and QCD events with apparent missing transverse energy.

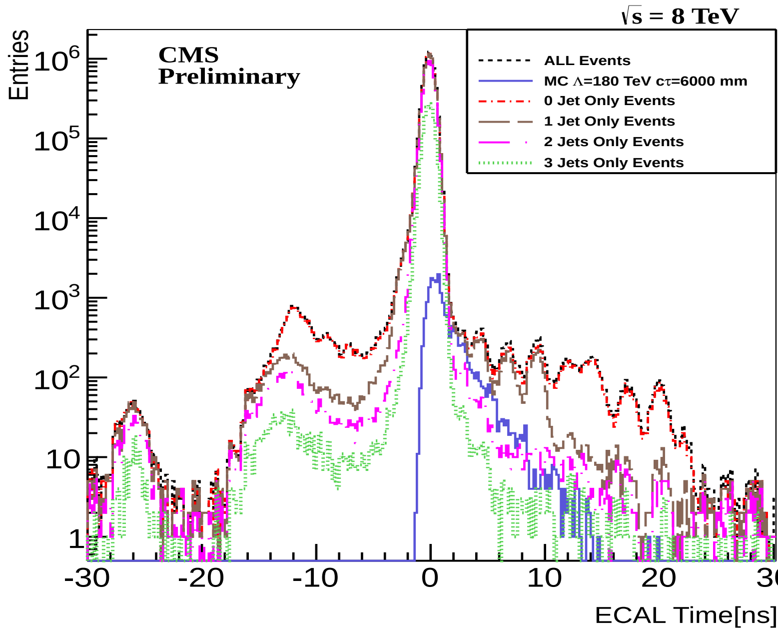

Figure 6.6: Comparing ECAL time distribution of events with different jet multiplicity from small sample of data and a single GMSB $\Lambda = 180$ TeV and $c\tau = 6000$ mm sample. Accepted photons must have $p_{\mathrm{T}} > 60$ GeV and belong to barrel and encaps.

Photon Selection Criteria	
Criteria	**Requirement**
`Event leading photon must have` $p_{\mathrm{T}}(\gamma^{1})$	> 80 GeV
`Other photons in event must have` $p_{\mathrm{T}}(\gamma^{2,3,\cdots})$	> 45 GeV
$\lvert\eta_{\gamma}\rvert$,(`Barrel Only`),	< 3.0 (< 1.5)
S_{Minor}	$0.12 \leq S_{Minor} \leq 0.38$
$E^{\mathrm{HCAL}}/E^{\gamma}$	< 0.05
$\Delta R(\gamma, track)$	> 0.6
Iso_{HCAL}, Iso_{ECAL}, Iso_{TRK}	$< 4.0\,\mathrm{GeV}$, $< 4.5\,\mathrm{GeV}$, $< 0.2\,\mathrm{GeV}$
Photon Isolation cone size $\Delta R(\gamma, \mathrm{particle})$	< 0.4
Topological Spike cuts	$1 - E_6/E_2 < 0.98$, $1 - E_4/E_1 < 0.98$

Table 6.3: The photon identification and selection criteria used in this analysis

Jet PF identification selection criteria	
Criteria	**Requirement**
`Jet` p_{T}	$> 35\,\mathrm{GeV}$
`Number of Jet constituents`	> 1
`Charge EM energy fraction (CEF)`	> 0.99
`Neutral Hadron energy fraction (NHF)`	< 0.99
`Neutral EM energy fraction (NEF)`	< 0.99
`If` $\lvert\eta\rvert$ `of jet is` > 2.4, `Charge Hadron energy fraction (CHF)`	> 0
`If` $\lvert\eta\rvert$ `of jet is` > 2.4, `Charge multiplicity (NCH)`	> 0
$\Delta R(\gamma, jet) = \sqrt{(\phi_{\gamma} - \phi_{jet})^2 + (\eta_{\gamma} - \eta_{jet})^2}$	> 0.3
$\not{E}_{\mathrm{T}}$, $\not{E}_{\mathrm{T}}^{\gamma}$	$> 60\,\mathrm{GeV}$

Table 6.4: The Jet ID and MET selection used in this analysis

In Figure 6.6, we observed that most of our background events with out-of-time beam halo-induced photons are mostly zero and one jet events. As a result, we use these zero and one jet events as a control sample only to study our background events, while our signal-like events are events with the following topology: $\geq 1\ \gamma + \geq 2\ jets + \not{E}_{\mathrm{T}} > 60\,\mathrm{GeV} + \not{E}_{\mathrm{T}}^{\gamma} > 60\,\mathrm{GeV}$.

6.4 Background Estimation

Most of our background events with out-of-time photons are non-collision events produced from different sources. In order to qualify and quantify these different sources, we compare in-time ($|t_\gamma| < 2$ ns) photon candidates to out-of-time ($t_\gamma < -3$ ns and $t_\gamma > 3$ ns) photon candidates. By also comparing photons from events with different number of jets, we were able to uncover the different background sources and better quantify the contribution from each source. In Figure 6.7, we present scatter plots of the photon's ECAL time against η (left) and against ϕ (right) for events with $\not{E}_{\mathrm{T}} > 25\,\mathrm{GeV}$ and photon $p_{\mathrm{T}} > 60\,\mathrm{GeV}$, belonging to the barrel and endcap regions.

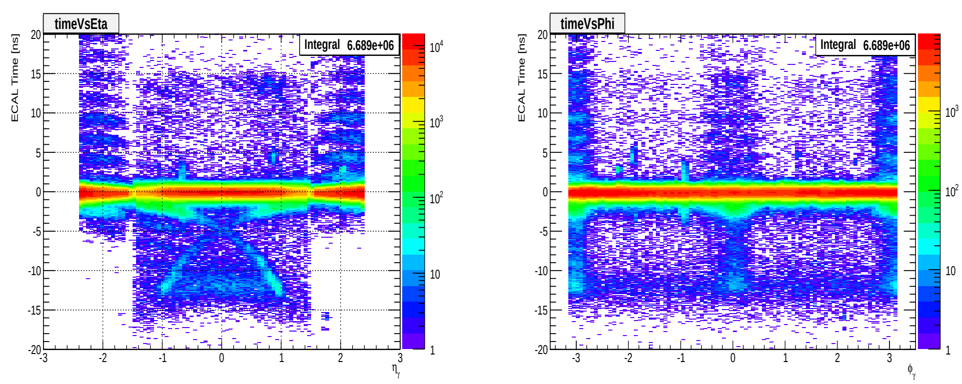

Figure 6.7: ECAL time against η (left) and ECAL time against ϕ (right) for photons with $p_{\mathrm{T}} > 60\,\mathrm{GeV}$ from data.

These scatter plots show that a good number of photons that are out-of-time belong to very different sources. For example, the "cross-like" feature seen on the left plot, is particular to photons with earlier time and in combination with the time-discrete

pattern, prominent in the endcaps ($1.479 < \eta_\gamma < 3$) regions and the high concentration at $\phi = 0 \pm \pi$ on the plot on the right, can be interpreted as photons produced by the same so-called proton beam halo. We argue the background out-of-time photon candidates can be split into 4 major categories: (1) Halo-induced photons from main and ghost/satellite beam halo muons, because they have early arrival times, creates the cross-like feature and time-discrete pattern and are also highly concentrated at $\phi = 0, \pm\pi$, (2) Cosmic-induced photons produced from cosmic muons, due to the random distribution of out-of-time photons throughout ECAL, (3) Spikes, due to the high concentration of photons with time of about -12.5 ns and Finally, (4) QCD or collision background events with photons with mis-measured ECAL time.
Since spikes are notoriously difficult to identified and eliminate, to reduce their contribution to out-of-time photons, we restrict our event selection to photons with time $2.0 < t_\gamma < 13.0$ ns and $-10.0 < t_\gamma < -3$ ns. This reduces our signal search window for events with late photon time to events with photon time between $2.0 < t_\gamma < 13.0$ ns.

We split the background events into Collision and Non-Collision event categories and study each category separately. We first identify and reject photon candidates from beam halo, cosmic muons and spikes and then estimate the residual non-collision and collision background photon candidates using the **ABCD** background estimation technique.

6.4.1 Collision Background

QCD Photons

Events from satellite/ghost proton bunches described in section 3.1.4, produce out-of-time photons which can be present in the barrel. We refer to the events from collisions with out-of-time photons, including QCD events with photons which have mis-measured time, as our *QCD background* events. It is challenging to define a strategy for rejecting this background events. Our approach, after rejecting non-collision events, is to estimate their contribution to signal using the ABCD background estimation method. We also perform a separate background estimation using a control sample of Z events, and show that, these events with out-of-time photons from collisions, are mostly QCD events with photon candidates with time mis-measurements.

6.4.2 Non-Collision Background

Halo-induced Photons

Protons in the main and sometimes ghost/satellite bunches can, through inelastic scattering with residual gas molecules like H_2 and CO_2 in beam pipe, produce pions which later decay into muons traveling with energy of a few TeV, called *Beam Halo* muons. These energetic muons radiate energetic photons, called *Halo-induced photons*, in the calorimeter through a process called *bremsstrahlung*. Some of the beam halo muons are produced when protons scatter off Tertiary Collimators (TCT), $50\,\mathrm{m} < z < 148\,\mathrm{m}$, away from the center of the CMS detector. These halo muons can travel nearly parallel to the main proton bunch but often stir outward from the nominal orbit due to betatron oscillations, in the transverse direction spreading mostly in the horizontal plane, with respect to the CMS detector coordinates. Despite beam cleaning, a sizable population of beam halo muons remains and eventually produce energetic photons in the calorimeters. A scatter plot of the photon ECAL time against ϕ shown earlier in the right plot of Figure 6.7, show that most of these beam halo muons enter the ECAL in the horizontal plane at $\phi = 0, \pm\pi$. The rate of halo-induced photons depend on the beam intensity, beam current and the operational conditions of the LHC, like, the machine optics, collimator settings, residual gas densities and LHC proton filling scheme.

The halo muons before entry into ECAL, produce tracks hits which can be reconstructed into muon tracks using segments in the Cathode Strip Chambers (CSC) Endcap muon detectors. The reconstructed tracks hits in the CSC segments can be associated with a halo-induce photon supercluster in ECAL within some narrow opening angle in ϕ.

Due to the beam intensity, most of the halo muons end up in the endcaps, but, some can also end up in the barrel. The resulting halo-induced photons are usually out-of-time compared to photons produced directly from nominal *pp* collisions. All of halo-induced photons have early arrival time, since the beam halo muons arrive at the crystals in ECAL before those photons produced at the interaction point in *pp* collisions. The halo-induced photon's arrival time can be estimated from the unique flight path of the beam halo muons, with respect to the arrival time of photons from *pp* collisions, as

$$t_{\mathrm{ECAL}}^{\mathrm{expected}} = -1/c\left(\pm Z_{\mathrm{cluster}} + \sqrt{Z_{\mathrm{cluster}}^2 + R_{\mathrm{cluster}}^2}\right), \tag{6.3}$$

where, Z_{cluster} is the point where the halo muon hits ECAL or the longitudinal distance along z-axis of the halo-induced photon supercluster position measured from the nominal interaction point, R is the radial distance of the supercluster from the beam line, which is equal to 1.29 m in the barrel, and c is the speed of light in vacuum. The estimated halo-induced photon arrival time can be re-arranged to become

$$t_{\text{ECAL}}^{\text{expected}} = -\frac{R}{2c} \exp^{(-\eta)} \tag{6.4}$$

showing the direct dependence on η. In Figure 6.8, the halo-induced photon estimated time is shown as the two red lines, agreeing well with with observation from data. This give us confidence that we understand the source of halo-induced photons and can develop a method of identifying events with halo-induced photons.

By matching halo muon hit positions in CSC segments to photon supercluster positions in the ECAL in ϕ, since halo muons spread mostly in the horizontal plane, we are able to match halo muons to their corresponding halo-induced photons. We use the quantity, $\Delta\phi(\text{CSC Seg}, \gamma)$, which is defined as the difference in ϕ between the CSC segment and the photon supercluster position in ECAL, to express this matching. A plot of $\Delta\phi(\text{CSC Seg}, \gamma)$ for in-time and out-of-time photons is shown in the left plot of Figure 6.8. We find that out-of-time photons often have small $\Delta\phi(\text{CSC Seg}, \gamma)$, further confirming that some out-of-time photons are produced by beam halo muons.

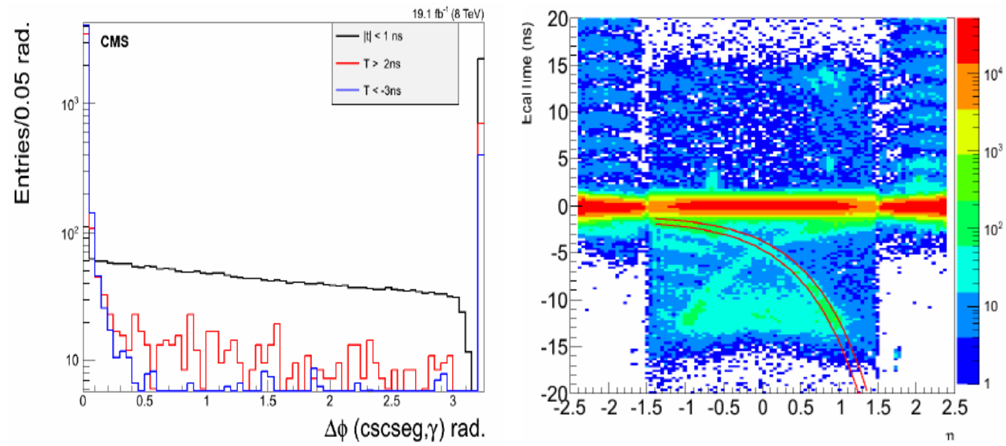

Figure 6.8: ECAL time vs $\Delta\phi(\text{CSC Seg}, \gamma)$ (left) for in time (black) and out-of-time (red and blue) photons. Photon ECAL time $V.s$ η (right), expected halo-induced photon time is shown as two red lines.

Cosmic-induced Photons

Muons produced in cosmic rays with sufficient energy, traveling through the CMS detector, will radiate (bremsstrahlung) photons in ECAL. We refer to these photons as *cosmic-induced photons*. Unlike halo muons, muons from cosmic rays can arrive at ECAL from any direction at any time. We expect the cosmic-induced photons in the barrel to leave track hits, produced by the associated muons from cosmic, in the Drift Tubes (DT) segments found in the muon barrel behind the calorimeters.

Using DT segments and photon supercluster position, in $\eta - \phi$ directions, in ECAL, we can match cosmic muon track hits in DT segments to ECAL photon superclusters within a narrow window in $\Delta\eta$ and $\Delta\phi$. The DT position, used in the calculation of $\Delta\eta$ and $\Delta\phi$, is a projection of the muon trajectory, using the direction of the DT segment, to the outer surface of ECAL; because of the large space between the muon barrel and the ECAL. A scatter plot for $\Delta\eta(\text{DT Seg}, \gamma)$ and $\Delta\phi(\text{DT Seg}, \gamma)$ of the matching, for events with out-of-time photons; $t_\gamma > 2$ ns and $t_\gamma < -3$ ns, is shown on the right plot of Figure 6.9. We compare these scatter plots of $\Delta\eta(\text{DT Seg}, \gamma)$ and $\Delta\phi(\text{DT Seg}, \gamma)$ to the scatter plots for in-time ($|t_\gamma| < 1$ ns), shown on the left plot, of the same Figure 6.9, and find that most out-of-time photons have a small $\Delta\eta$ and $\Delta\phi$.

If we compare these scatter plots of $\Delta\eta$ and $\Delta\phi$, for these out-of-time photons, to the scatter plots for cosmic-induced photons from a pure cosmic muons sample (data recorded by the CMS detector without proton-proton collisions happening), shown in Figure 6.10, we find a similar small $\Delta\eta$ and $\Delta\phi$ occupancy for the true cosmic muons events from the pure cosmic sample. We conclude that, it is possible to use small $\Delta\eta(\text{DT Seg}, \gamma)$ and $\Delta\phi(\text{DT Seg}, \gamma)$, to tag and reject events with cosmic-induced photons.

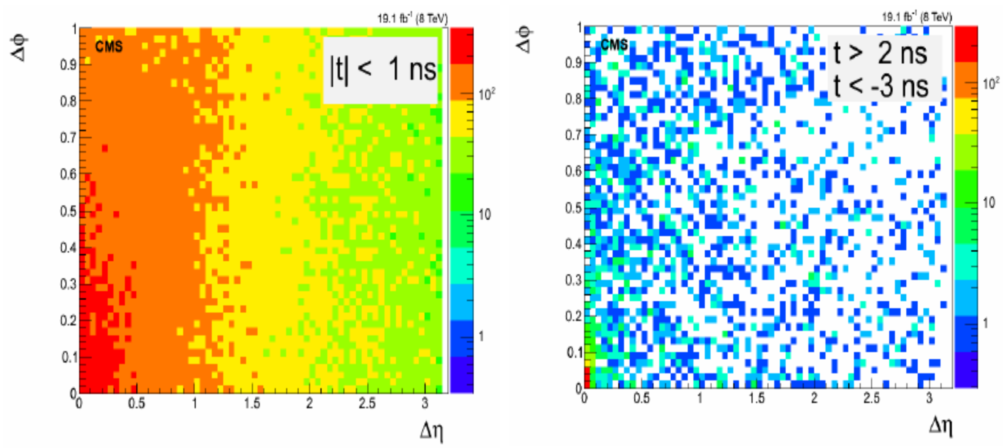

Figure 6.9: Scatter plot showing $\Delta\eta(\text{DT Seg}, \gamma)$ against $\Delta\phi(\text{DT Seg}, \gamma)$ for out-of-time ($t_\gamma > 2$ ns and $t_\gamma < -3$ ns) photons (right) compared to in-time($|t_\gamma| < 1$ ns) photons (left). Cosmic photon candidates have small $\Delta\eta$ and $\Delta\phi$.

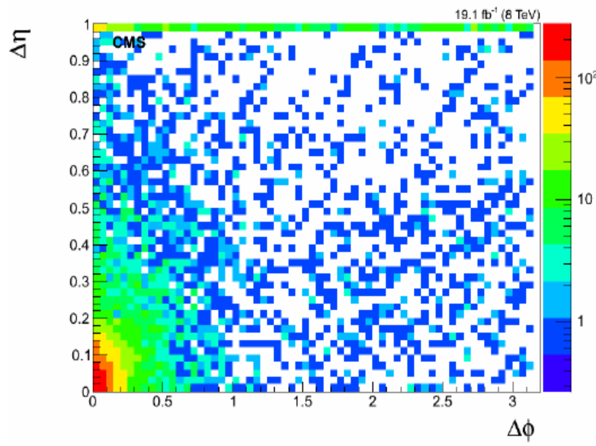

Figure 6.10: Scatter plot of $\Delta\eta(\text{DT Seg}, \gamma)$ against $\Delta\phi(\text{DT Seg}, \gamma)$ for photons from pure cosmic muon data. Small $\Delta\eta$ and $\Delta\phi$ are cosmic photons.

Spike-Seeded Photons

Neutrons and charge hadrons can at times deposit their energy directly on the APDs in addition to going through the crystal scintillation process. Such signals, read from the APDs, are *anomalous* and referred to as *spike-seeded photons* or simply *spikes.* Spikes produced from pp collisions and passing our photon selection requirements, can easily be identified as good photon candidates. A spike supercluster consist of very few crystals; most often one or two crystals. Because spikes occupy few crystals, they can overlapped with good photon candidates, embedded in the photon's supercluster, or buried inside jets. Such embedded spikes cannot be easily identified.

The arrival time of spikes is much earlier (negative), usually about $t = -12.0$ ns, than for photons produced in nominal pp collisions and depositing their energy, through crystal scintillation, on the APDs. This is because for spikes, there is the absence of the crystal scintillation process; which takes on average 10 ns. The few crystals holding the spike energy deposits, make it possible for spikes to be identified using a energy topological selection quantity, know as *swiss-cross* and defined as $1 - \frac{E_4}{E_1}$. A distribution of swiss-cross for in-time photon events, compare to events from a spike sample (events with photon time $t = -12$ ns) is shown on the right plot of Figure 6.11. We find that most spikes have about 98% of their energy deposited in a single crystal.

Using the number of crystals in a photon supercluster and comparing the number of crystals belonging to in-time photons, halo-induced photons and spike-seeded photons (photons with $1 - \frac{E_4}{E_1} > 0.98$), shown on the left plot of Figure 6.11, we conclude that most spikes, including spikes embedded in photon candidates, have less than 7 crystals belonging to their supercluster. A combination of the swiss-cross, number of crystals belonging to the supercluster, calculated χ^2 (defined in Equation 6.2) of ECAL time, and S_{Minor} (S_{Minor} describes the spread in width, in terms of number of crystals, of the photon electromagnetic shower), is useful for identifying and rejecting events with spike-seeded photons.

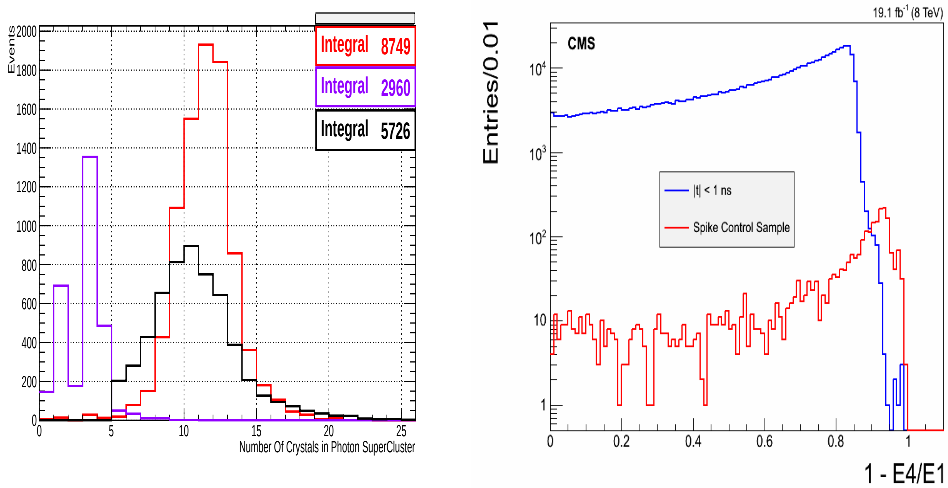

Figure 6.11: *Number of crystals* belonging to a photon supercluster (left) plot for in-time photon candidates (black), spike-seeded photon candidates (magenta) and halo-induced photon candidates (red). The spike-seeded photon candidates are selected using a swiss-cross variable $(1 - E_4/E_1)$ (right), shown comparing in-time photons ($|t_\gamma| < 1.0$) to spike candidate sample selected using S_{Minor}.

6.4.3 Event Vetoing

We tag and veto events with halo-induced, cosmic-induced and spike-seeded photons as follows:

- An event with a halo-induced photon is tagged and vetoed, if a CSC segment for $|\eta| > 1.6$, is found within 0.05 radian of angle ϕ, with the photon supercluster, i.e. a photon found within $\Delta\phi(\text{CSC Seg}, \gamma) < 0.05$, is vetoed.
- An event with cosmic-induced photon is tagged and vetoed, if the photon can be matched to a DT segment within $\Delta\eta(\text{DT Seg}, \gamma) < 0.1$, and $\Delta\phi(\text{DT Seg}, \gamma) < 0.1$.
- An event with spike-seeded photon is vetoed, if the photon has ECAL time $\chi^2 > 4$, number of crystals < 7, $1 - E_4/E_1 > 0.98$, and $S_{Minor} < 0.17$.

The result of the event tagging is shown in Figure 6.12. We observe that most of the non-collision background events are events with halo-induced photons. Very few late arrival time photons are produced from spikes. There is also some significant contribution from cosmic-induced photons. The most interesting observation is the residual out-of-time background (in red) which could not be tagged.

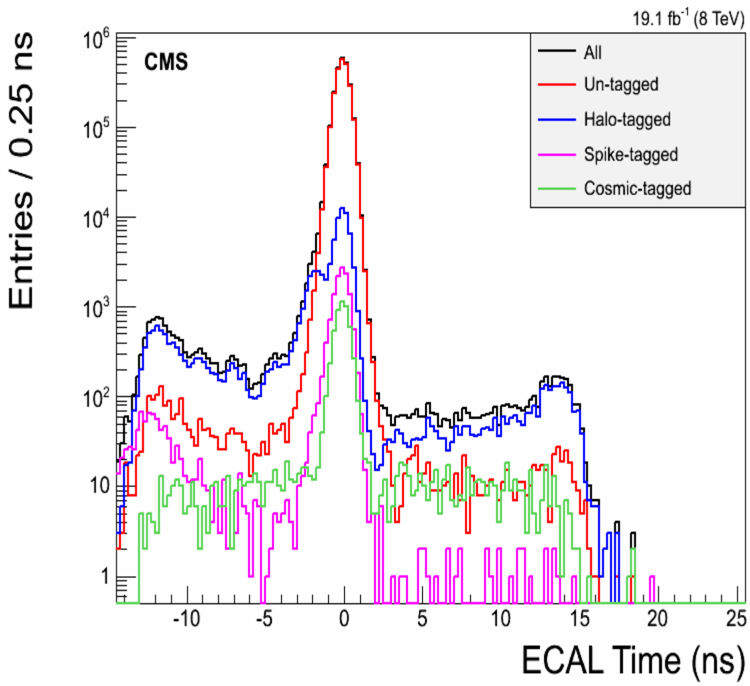

Figure 6.12: Photon ECAL time, for a data sample of 0 and 1-jet events, showing our tagging performance for non-collision background events.

These residual untagged events comprise of some non-collision events, since the tagging and vetoing are not 100% efficient, and mostly collision events with mis-measured time photons. In order to quantify our estimates of these different sources contributing to the untagged background events, we use control samples defined with $\not\!\!E_T^{\gamma}$ and $\not\!\!E_T$.

We expect signal events, because of the undetected gravitino from the decay of $\widetilde{\chi}_1^0$, to have large $\not\!\!E_T^{\gamma}$ and $\not\!\!E_T$; by large, we mean above 60 GeV. The non-collision (cosmic-induced, halo-induced, spike-seeded photons) and collision (ghost/satellite and QCD) background events can be categorized into high-p_T and low-p_T events. For high-p_T non-collision events, we expect these events to have large $\not\!\!E_T$, due to the exclusion of the energy deposits from the out-of-time photons in the missing transverse energy reconstruction, and small $\not\!\!E_T^{\gamma}$, when the large transverse energy contribution from the energy deposits, of the out-of-time photons, is re-introduced, while for low-p_T non-collision events, we expect these events to have both $\not\!\!E_T^{\gamma}$ and $\not\!\!E_T$ small, since the out-of-time photon transverse energy, which was excluded, was in the first place small.

For high-p_{T} out-of-time collision events, which under normal circumstances should have large missing transverse energy, we expect their $\not\!\!E_{\mathrm{T}}$ to be large and after re-introducing the energy deposits from out-of-time high-p_{T} photons, we expect their $\not\!\!E_{\mathrm{T}}^{\gamma}$ to be small, while, using the same argument made for low-p_{T} non-collision events, we expect low-p_{T} collision events to have both small $\not\!\!E_{\mathrm{T}}^{\gamma}$ and $\not\!\!E_{\mathrm{T}}$. A summary of our expectations for $\not\!\!E_{\mathrm{T}}^{\gamma}$ and $\not\!\!E_{\mathrm{T}}$ for the different expected background events sources, with possible contribution to the residual untagged events with out-of-time photon, is presented in Table 6.5.

Event Sample	$\not\!\!E_{\mathrm{T}}$	$\not\!\!E_{\mathrm{T}}^{\gamma}$
Signal Events	Large	Large
High-p_{T} Non-Collision(Mostly Beam Halo) Events	Large	Small
Low-p_{T} Non-Collision Events	Small	Small
High-p_{T} Collision(QCD/Ghost) Events	Large	Small
Low-p_{T} Collision Events	Small	Small

Table 6.5: Summary of missing transverse expectation for events with out-of-time photons.

Using control samples defined using $\not\!\!E_{\mathrm{T}}$ and $\not\!\!E_{\mathrm{T}}^{\gamma}$ for events with in-time ($|t_{\gamma}| < 2.0$ ns) photons, events with out-of-time photons, $t_{\gamma} > 3.0$ ns and $t_{\gamma} < -3.0$ ns, where each control sample is defined purposely to enhance the contribution of either collision or non-collision background events in the control sample, and simultaneously suppressing contributions from the other, we perform a background estimation in the signal sample ($t_{\gamma} > 3.0$ ns, $\not\!\!E_{\mathrm{T}}^{\gamma} > 60\,\mathrm{GeV}$ and $\not\!\!E_{\mathrm{T}} > 60\,\mathrm{GeV}$), using the so-called ABCD background estimation method and verify that the background estimation method is performing as expected using a data sample of zero and one jet events.

6.4.4 Background Estimation with ABDC Method

Since we expect most of our background events to come from non-collision events, we estimate the number of events we expect from non-collision events in the signal control sample using the ABCD technique. We also estimate the possible contamination, we expect from collision events, to the control samples used in the ABCD method.

Non-Collision Background Estimation

To estimate the number of background events from non-collision events, we define regions labeled as ABCD, in photon ECAL time and $\not\!\!E_{\mathrm{T}}$, for selected events with $\not\!\!E_{\mathrm{T}}^{\gamma} > 60\,\mathrm{GeV}$. Events with $\not\!\!E_{\mathrm{T}}^{\gamma} > 60\,\mathrm{GeV}$, defines a Control Sample (CS) in which the contribution from collision (QCD) background events is suppressed, since most collision background events have small $\not\!\!E_{\mathrm{T}}^{\gamma}$, as we saw in Table 6.5. The regions: A and B, shown in Table 6.6, contain events with, respectively, $\not\!\!E_{\mathrm{T}} < 60\,\mathrm{GeV}$ and $\not\!\!E_{\mathrm{T}} > 60\,\mathrm{GeV}$, and photon ECAL time, $-10.0 < t_{\gamma} < -3.0$ ns, and region C, contain events with $\not\!\!E_{\mathrm{T}} < 60\,\mathrm{GeV}$ and photon ECAL time, $3.0 < t_{\gamma} < 13.0$ ns.

Non-Collision	$\not\!\!E_{\mathrm{T}} < 60\,\mathrm{GeV}$	$\not\!\!E_{\mathrm{T}} > 60\,\mathrm{GeV}$
$3.0 < t_{\gamma} < 13.0$ ns.	C	D
$-10.0 < t_{\gamma} < -3.0$ ns	A	B

Table 6.6: Definition of ABCD regions used for estimating non-collision background events in the signal region D. Events must satisfy the $\not\!\!E_{\mathrm{T}}^{\gamma} > 60\,\mathrm{GeV}$ selection requirement, which reduces collision background events significantly.

The remaining collision background events, which may have some contribution in the B and D regions, are estimated in the next section and also corrected for.

Since the arrival time of photons is independent of the missing transverse energy in the event and since we are selecting events with out-of-time photons (where the definition of $\not\!\!E_{\mathrm{T}}$, is the same for all events) in defining the ABCD regions, we expect the ratio in the number of events with high-$\not\!\!E_{\mathrm{T}}$ and low-$\not\!\!E_{\mathrm{T}}$, for both out-of-time regions, to be the same, provided the contribution from collision events with mis-measured photon time is not large, i.e. $\frac{N_D}{N_C} = \frac{N_B}{N_A}$. With this, the number of non-collision background events, with out-of-time photons, expected in the signal region D, is given as

$$N_D^{non-col} = \left(\frac{N_B}{N_A}\right) \cdot N_C, \tag{6.5}$$

where, N_B, N_A and N_C, are the number of events observed in B, A and C regions, in that order, and $N_D^{non-col}$, is the number of non-collision background events we expect in the signal region D.

Collision Background Estimation

We want to estimate the contribution from collision background events to regions B and D of Table 6.6. Using the ABCD technique again, we define regions in photon ECAL time and $\not\!\!E_{\mathrm{T}}^{\gamma}$, for selected events with $\not\!\!E_{\mathrm{T}} > 60\,\mathrm{GeV}$. The events with $\not\!\!E_{\mathrm{T}} > 60\,\mathrm{GeV}$ define a control sample, where the contribution from collision events is dominant, as seen in Table 6.5. Since most collision events have in-time ($|t_\gamma| < 2$ ns) photons, the few collision events with out-of-time photons contributing to the B and D regions, because the photon time is mis-measured, can be estimated using regions with in-time photons. The definition of each region used in the ABCD method, to estimate the out-of-time photon collision background, is given in Table 6.7.

Collision	$\not\!\!E_{\mathrm{T}}^{\gamma} < 60\,\mathrm{GeV}$	$\not\!\!E_{\mathrm{T}}^{\gamma} > 60\,\mathrm{GeV}$
$3.0 < t_\gamma < 13.0$ ns.	C	D
$-2.0 < t_\gamma < 2.0$ ns	E	F
$-10.0 < t_\gamma < -3.0$ ns	A	B

Table 6.7: A,B,C,D,E,F regions used for estimating collision background events with out-of-time photons contamination the regions B and D of Table 6.6. Here, events must satisfy $\not\!\!E_{\mathrm{T}} > 60\,\mathrm{GeV}$, selection requirement.

Using a similar argument that the photon arrival time is independent of the missing transverse energy, the number of collision events contributing to the region B, N_B^{col}, is estimated as

$$N_B^{col} = N_B = \left(\frac{F}{E}\right) \cdot N_A, \tag{6.6}$$

and the number of events contributing to the signal region D, N_D^{col}, is estimated as

$$N_D^{col} = N_D = \left(\frac{F}{E}\right) \cdot N_C, \tag{6.7}$$

where, N_i, is the number of events in each region, $i =$ A,B,C,D,E,F.

Combined Background Estimation

Now that we have estimates for both collision and non-collision event contributions, we can estimate the total number of background events expected in the signal region D (Events with $\not\!\!E_{\mathrm{T}} > 60\,\mathrm{GeV}$, $\not\!\!E_{\mathrm{T}}^{\gamma} > 60\,\mathrm{GeV}$ and $3.0 < t_\gamma < 13.0$ ns), as

$$N_D^{Total} = \left(\frac{N_B - N_B^{col}}{N_A}\right) \cdot N_C + N_D^{col} = N_D^{non-col} + N_D^{col} \tag{6.8}$$

where, $N_D^{Total} = N_D^{non-col} + N_D^{col}$, is the total background events estimated in our signal region D from non-collision and collision background events.

Background Estimation Method Validation

We verify that our background estimation method performs as expected using a data sample of 0 and 1-jet events. We do not expect signal events in this sample. A statistical agreement between the expected number of background events, obtained using our background estimation method, and the number of events observed in our signal region D, affirms that the method is reliable. The accepted 0 and 1-jet events used must pass the same event selection requirements as potential signal events described in Tables 6.3 and 6.4, in addition to vetoing non-collision background events. The event yields in each control sample including tagged events with halo-induced, cosmic-induced and spike-seeded photons is shown in Table 6.8.

Control Sample	Yield	Beam Halo	Cosmic	Spike
A	851	5075	237	65
B	38	300	17	1
C	359	1508	368	9
D	10	22	30	0
A	8	1	1	0
C	2	0	0	0
F	35271	-	-	-
E	1445254	-	-	
B	-	-	-	-
D	-	-	-	-

Table 6.8: Event yields used in validating the ABCD background estimation method using 0 and 1-jet events sample. Halo/cosmic/spikes yields are obtained from tagged events. All events must pass photon, jet and $E_{\mathrm{T}}^{\mathrm{miss}}$ selection requirements.

Using the event yields in Table 6.8 for each region, and Equations 6.6, 6.7 and 6.8, we obtain the following estimates for the expected number of events in signal region D:

$$
\begin{aligned}
N_B^{col} &= \frac{35271}{1445254} \times 8 = 0.64^{+0.35}_{-0.34},\\
N_D^{col} &= \frac{35271}{1445254} \times 2 = 0.46^{+0.11}_{-0.09},\\
N_D^{Total} &= \left(\frac{38 - 0.64}{851} \times 359\right) + 0.46 = 16.41^{+3.00}_{-2.59}.
\end{aligned}
$$

The uncertainty are statistical uncertainties based on the event statistics in each region. Our expected number of background events in signal region D is $16.41^{+3.00}_{-2.59}$, which is, within the statistical uncertainties, agreeable with the 10 events we observe, satisfying all our event selection requirements, in the signal region D. This give us confidence in our background estimation method and the impetus to use the method in our background estimation of signal events.

6.4.5 Background Estimation Cross Check

Another method for estimating our background events with out-of-time electromagnetic particles from collision, is using Z $\rightarrow e^+e^-$ events, since we expect the electron candidates from Z decay to be in-time because of the prompt nature of the decay of Z bosons. We use events with electron candidates from a `SingleElectron` (single electron triggered events) and `DoubleElectron` (double electron triggered events) data samples, where we expect contributions from non-collision events to be very small. These events are selected such that out-of-time energy deposits in ECAL, from electron candidates, are accepted. The background events to the Z-boson events are events with candidate electrons from collision with mis-measured electron time. An out-of-time electron can be randomly matched with another candidate electron to give a di-electron mass which is of the order of the mass of Z. These background events also include events with poorly reconstructed out-of-time energy deposits in ECAL.

To reduce any out-of-time event from beam halo and cosmic events, occurring simultaneously with true pp collision events, we accept only events satisfying the following event selection requirements: the two electron candidates for the Z boson must each have a $p_{\mathrm{T}} > 30\,\mathrm{GeV}/c$, the di-electron mass, $|m_{e^+e^-} - 91| > 61\,\mathrm{GeV}/c^2$, both electrons must be in the barrel, i.e. $|\eta_{e^-}| < 1.479$ and $|\eta_{e^+}| < 1.479$ and the electron ECAL arrival time

$\chi^2 < 4$. The electron's arrival time is taken to be the seed crystal time, and corrected to account for the electron's time of flight, which is different from photons. The chosen seed crystal must satisfy the recommended crystal (reconstructed hit) cleaning criteria; which requires that the seed crystal is not a spike, is not noisy and has been properly time calibrated.

From the accepted events with Z candidates, we define a signal event sample for which the di-electron mass is between 76 and 100 GeV/c^2, i.e. $76\,\text{GeV}/c^2 < |m_{e^+e^-}| < 100\ GeV/c^2$, and a background or sideband event sample where the di-electron mass is either between $50\,\text{GeV}/c^2 < m_{e^+e^-} < 76\,\text{GeV}/c^2$ or $100\,\text{GeV}/c^2 < m_{e^+e^-} < 130\,\text{GeV}/c^2$. The di-electron mass (left plot) and electron arrival time (right plot) of both electron candidates of the Z boson (signal (blue)) together with the total Z boson candidates is shown in Figure 6.13.

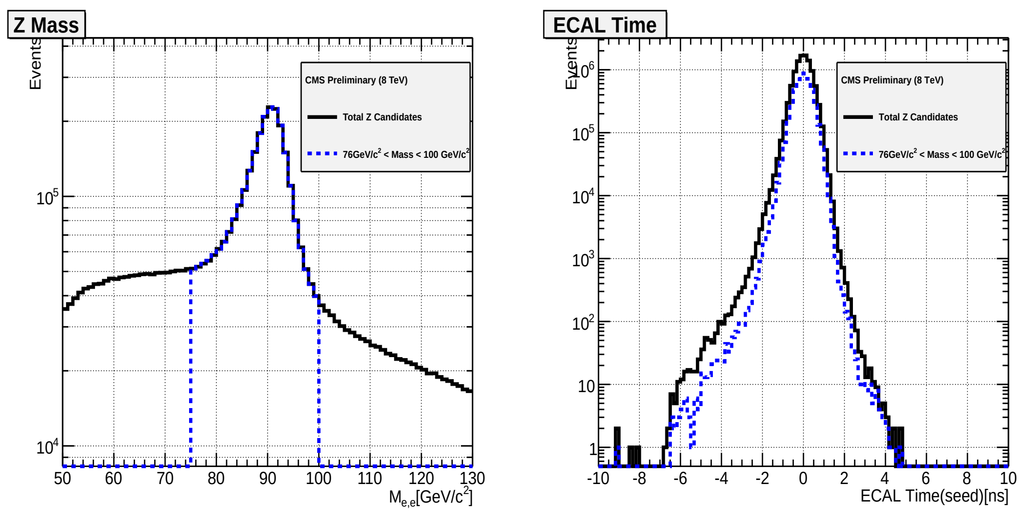

Figure 6.13: Di-electron mass distribution (left) and the time (right) of the two electron candidates for the signal, $76 < m_{e^+e^-} < 100\,\text{GeV}/c^2$, of Z boson sample. Events are from the `Single/DoubleElectron` data sample.

A scatter plot of the arrival ECAL time against η (top right plot) and ϕ (bottom right plots) of both electrons of the Z is shown in Figure 6.14. A clear difference in the scatter plots is seen comparing events from the `Single/DoubleElectron` data sample (plots on the right), which do not have the familiar beam halo features (the "cross-shape" and high event concentration at $\phi = 0, \pm\pi$), to events from `SinglePhoton` data sample (plots on the left). We conclude that, the candidate Z event sample is free from contamination from non-collision events and is useful for estimating out-of-time background events from collisions.

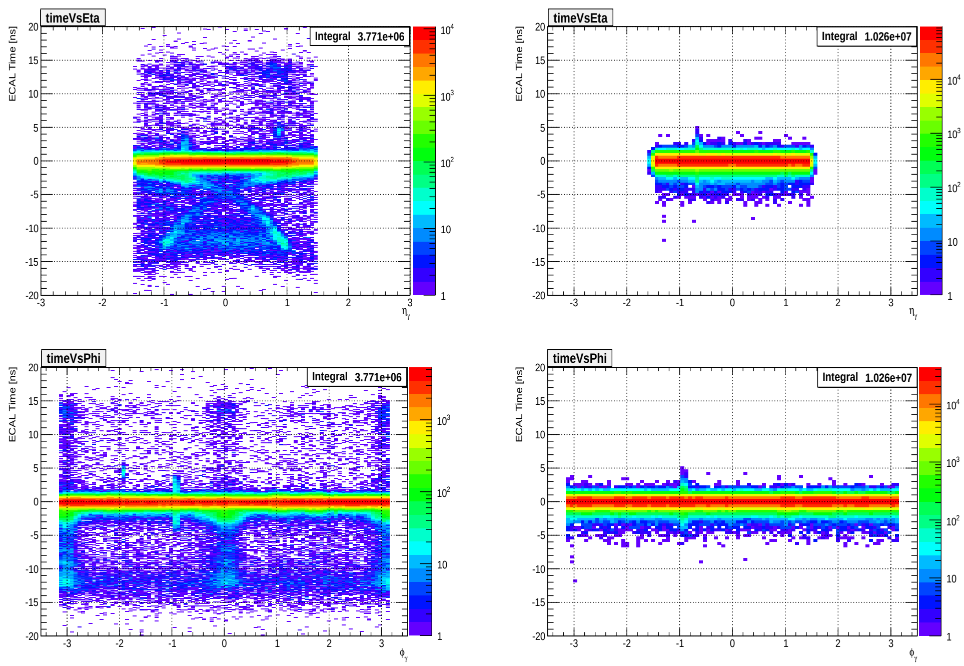

Figure 6.14: ECAL time $Vs\ \eta$ (top plots) and $Vs\ \phi$ (bottom plots) for electromagnetic particle candidates from `SinglePhoton` data sample (left) compared to electromagnetic particle candidates from the `Single/DoubleElectron` data sample (right). All electromagnetic particle candidates are in barrel. Most of the electromagnetic particles with "cross-shape" and at $\phi = 0, \pm\pi$, are halo-induced photons.

In order to estimate the out-of-time background events from collision, we estimate the probability for an in-time ($|t| < 2$ ns) event to become out-of-time ($t < -3$ ns or $t > 3$ ns) because of the mis-measurement of the time of the electron candidates.
We estimate this probability by dividing the Z candidate events according to their arrival time as follows:

- In-time Z boson events: Both electrons of the Z boson candidate have arrival time, $|t| < 2$ ns. Their di-electron mass is shown on the top right plot of Figure 6.15,

- Early time Z boson events: Both electrons of the Z boson candidate have arrival time, $t < -3$ ns. Di-electron mass shown in the bottom left plot of Figure 6.15,
- Late time Z boson events: At least one of the electrons of the Z boson candidate have arrival time, $t > 3$ ns. The di-electron mass is shown in the bottom right plot of Figure 6.15.

The true Z boson events in each of the three Z boson event samples, defined above, is estimated as follows: we first fit, with a polynomial function, a sideband ($50 < m_{e^+e^-} < 76\,\mathrm{GeV}/c^2$ and $100 < m_{e^+e^-} < 130\,\mathrm{GeV}/c^2$) of the di-electron mass distribution (see top left plot of Figure 6.15). Using the side band fit function, we subtract the integral of the fit function from the total number of Z boson candidates in the Z boson mass peak ($76 < m_{e^+e^-} < 100\,\mathrm{GeV}/c^2$) in each of the three samples. The result of the subtraction gives an estimate of the true Z boson events in the in-time and out-of-time Z boson event samples.
Table 6.9 show the resulting number of Z boson events.

Event Sample	**Early Time** ($t < -3$ ns)	**In-time** ($\lvert t \rvert < 2$ ns)	**Late Time** ($t > 3$ ns)
Total	378	2349187.0	41.0
Estimated Z boson Background	329	996803.6	8.6
Estimated signal Z bosons	49	1352383.4	32.4

Table 6.9: Number of Z boson events with di-electron invariant mass, $76 < m_{e^+e^-} < 100\,\mathrm{GeV}/c^2$) in the in-time and out-of-time Z boson samples.

The 32.4 events for the late time Z boson events consist of 3 Z events with both electrons with time, $t > 3$ ns. These 3 Z events could be attributed as produced from ghost/satellite bunch collisions since the ratio of these 3 events to in-time Z events (1.35 million) from main proton bunch collisions is of the order 10^{-6}, which is consistent expected luminosity at collision for ghost/satellite bunches. The intensity of ghost/satellite proton bunch is about 10^3 less than that for the main proton bunch [32, 33].
The probability for in-time events becoming out-of-time for proton bunch collision is P_1, and can be estimated as $29.4/1352383.4 = 1.09^{+0.28}_{-0.23} \times 10^{-5}$, while the probability

for in-time events becoming out-of-time for ghost/satellite bunch collisions is P_2, and can be estimated as $3/1352383.4 = 2.22^{+1.7}_{-0.96} \times 10^{-6}$.

Using these probabilities we can predict the number of collision background events in out analysis, which have late time ($t > 3.0$), as

$$N = n_1 \times P_1 + n_2 \times (2P_1(1 - P_1) + P_1^2) + n_1 \times P_2 + n_2 \times P_2 \tag{6.9}$$

where n_1 is the number of in-time one photon events (28208) and n_2 is the number of two photon in-time events (38) taken from the F region of the final results of our background estimation, shown in Table 6.11.

The estimated the number of background events from collisions in the signal region D, $N_D^{col} = 0.370^{+0.092}_{-0.072}$, events. Comparing this to the estimated background from collision, using the ABCD method, which is $28283/1446522 = 0.093^{+0.093}_{-0.047}$, events, we find that the two methods of estimating the number of background events from collision are not exactly equal. However, both method agree that the background contribution from collision events with out-of-time electromagnetic particles is almost negligible (less than a single event) such that the uncertainties on the ratio of out-of-time to in-time events used in our ABCD collision background estimation does not affect the final results.

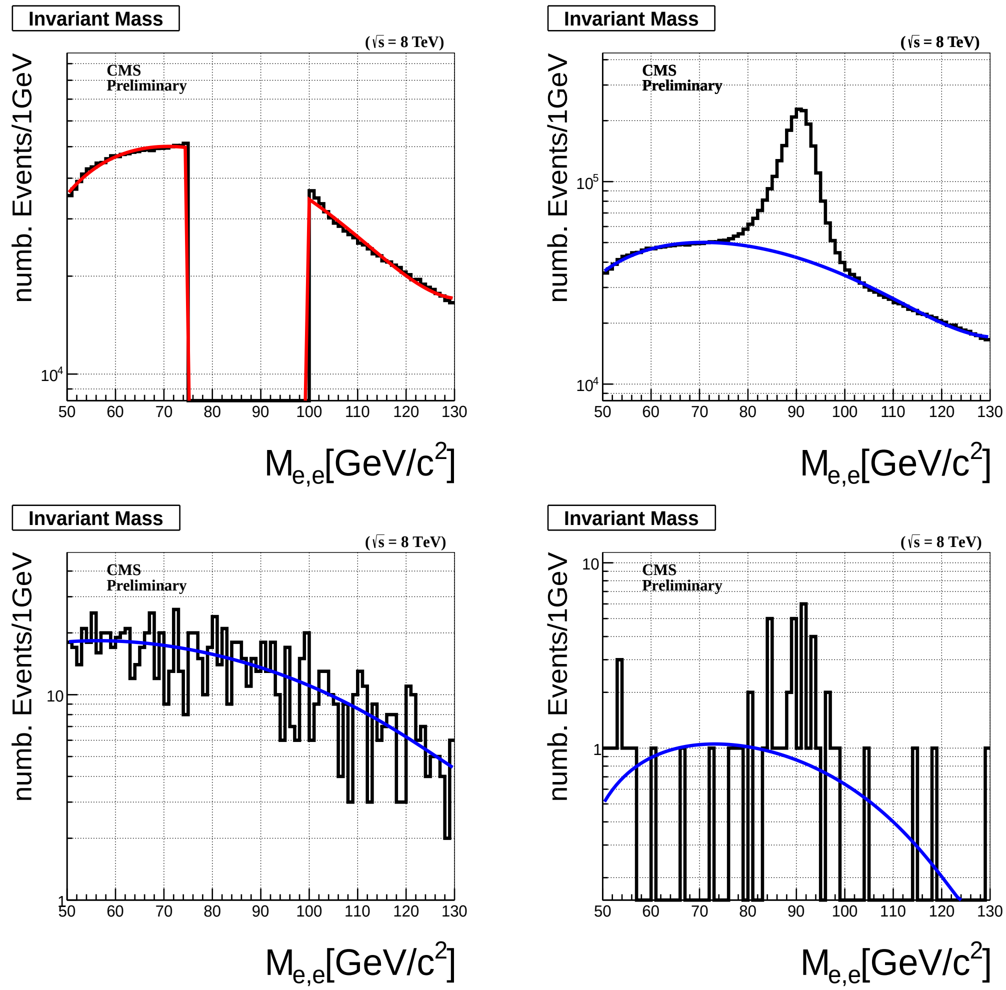

Figure 6.15: Di-electron invariant mass and polynomial fit (red) for sideband sample ($50 < m_{e^+e^-} < 76\,\mathrm{GeV}/c^2$ and $100 < m_{e^+e^-} < 130\,\mathrm{GeV}/c^2$). Di-electron invariant mass and polynomial fit (blue) for in-time ($|t| < 2$ ns) Z candidates (*top right*). Di-election invariant mass and polynomial fit for out-of-time ($t < -3$ ns) Z candidates (*bottom left*). Di-election invariant mass and polynomial fit for out-of-time ($t > 3$ ns) Z candidates (*bottom right*). The fits are used to estimated the number of true Z bosons in the int-time and out-of-time Z candidate samples.

6.5 Systematic Studies

We have required in our event selection that the photon p_{T} is greater than 80 GeV/c, the jet p_{T} is greater than 35 GeV/c and the missing energy is greater than 60 GeV. The same selection requirements applied to our MC signal event sample should guarantee a good event selection efficiency estimate. Any difference in the photon p_{T}, jet p_{T} and missing transverse energy between MC and data, will be a source of systematic uncertainties on the efficiency of selecting signal events. These uncertainties can come from quantities like jet energy scale (JES), jet energy resolution (JER), electron-photon energy scale, instrumentation related and energy deposits not clustered during missing transverse energy reconstruction, photon ECAL arrival time bias and ECAL time resolution.

Table 6.10 presents the sources of uncertainties considered in this analysis. These uncertainties are computed by varying the nominal values of each quantity, while keeping the others fixed, by 1σ deviation and counting the number of events passing our event selection requirements. ECAL timing bias which has to do with the absolute reference time (zero ns) of the ECAL timing, is the source of our largest uncertainty. The photon arrival time is measured with respect to this reference time. This ECAL time uncertainty has the largest impact on our analysis, since our analysis is based on counting the number of events with photon ECAL time above 3 ns. The next largest uncertainties are from energy deposits missed by the clustering algorithm. This affects the photon energy scale, missing energy scale, jet energy scale and resolution. The uncertainty on the photon energy scale in the barrel was estimated to be 4.0% which is based on measuring the photon energy of events with $Z \to \mu\mu\gamma$ decay, where the muon radiates a photon in a process known as the final-state radiation (FSR) [57].

The uncertainty on the $E_{\mathrm{T}}^{\mathrm{miss}}$ resolution uses a conservative estimate from $E_{\mathrm{T}}^{\mathrm{miss}}$ measurements in QCD events [58], where the $E_{\mathrm{T}}^{\mathrm{miss}}$ uncertainty is calculated using the fraction of events passing an event selection based on $E_{\mathrm{T}}^{\mathrm{miss}}$ for varying thresholds of $E_{\mathrm{T}}^{\mathrm{miss}}$.

The uncertainty on the ECAL time resolution was obtained by comparing the mean time of photons of events from $\gamma+$ jet MC sample to events from data with photon ECAL time, $|t_{\gamma}| < 2$ ns. The difference is found to be of the order of 200 ps per event.

Meanwhile, the systematic uncertainty on luminosity measurement has the recommended value of 2.2% provided by CMS and LHC luminosity measurements while the uncertainty from Parton Density Functions (PDF) is evaluated using the re-weighting technique which uses the Master Equation of CTEQ65 model set described in [59].
Since our background estimation is data-driven, the systematic uncertainties do not impact our results in a significant way. The statistical uncertainty in the ABCD background estimation method is our largest source of uncertainty in this analysis and we estimate it to vary upward by 223% and downward by 51%. This large background statistical uncertainty is because of the very low event yields. Our final result is affected by the signal selection efficiency only, despite the large background estimation uncertainty. These signal selection uncertainties are used as nuissance parameters in the calculation of the upper limit on the observed signal cross section (σ_{UL}).

Source	**Uncertainty(%)**
`ECAL absolute time` (0.0 ns)	$< 10.0\%$
`ECAL time resolution` (0.5 ns)	$< 5.0\%$
`Unclustered energy deposits`	$< 9.0\%$
`Photon energy scale`	$< 4.0\%$
`Jet energy scale` (JES)	$< 9.0\%$
`Jet energy resolution` (JER)	$< 9.0\%$
$E_{\mathrm{T}}^{\mathtt{miss}}$ `resolution`	$< 2.8\%$
`PDF uncertainty`	$< 1.70\%$
`Background estimation uncertainty`	51.0% to 223%
`Luminosity` (4.5%)	$< 2.2\%$

Table 6.10: Summary of systematic uncertainties for signal efficiency and background estimation in this analysis and applied to our final results.

6.6 Results

After running our analysis on the SinglePhoton data samples requiring events with at least 2 jets, at least one photon with ECAL time $3.0 < t_\gamma < 13.0$ ns, $\not{E}_T^\gamma > 60$ GeV, and $\not{E}_T > 60$ GeV, we observed a single event passing all our event selection requirements as a signal candidate. This event has one photon and two jets. The photon has a transverse momentum of 224 GeV/c and an ECAL time of 12.17 ns.
Our expected number of background events estimated is $0.093^{+0.301}_{-0.047}$. This number was computed as

$$N_B^{col} = \frac{28246}{604958} \times 3 = 0.140^{+0.108}_{-0.061}$$
$$N_D^{col} = \frac{28246}{604958} \times 2 = 0.093^{+0.093}_{-0.047}$$
$$N_D^{Total} = \left(\frac{1 - 0.14}{3} \times 0\right) + 0.093 = 0.093^{+0.301}_{-0.047}$$

using the event yields presented in Table 6.11.

In our final result, we use the collision background estimated using the $Z \rightarrow e^+e^-$ method which gave us the following:

$$N_B^{col} = 0.51^{+0.28}_{-0.27}$$
$$N_D^{col} = 0.37^{+0.09}_{-0.07}$$
$$N_D^{Total} = \left(\frac{1 - 0.51}{3} \times 0\right) + 0.37 = 0.37^{+0.39}_{-0.07}.$$

Control Sample	Yield
Total Events	
D	1
C	0
B	1
A	3
Collision Background Events	
A	2
C	4
F	28246
E	604958

Table 6.11: Event yields used in our final background estimation for signal candidate events with at least a single photon and at least 2 jets, $\not\!\!E_{\mathrm{T}}^{\gamma} > 60$ GeV, and $\not\!\!E_{\mathrm{T}} > 60$ GeV.

With no significant excess over expected number of background events, we compute limits on the number of events at 95% confidence interval using the CLs limit computing method.

Chapter 7

Statistical Analysis

7.1 Limit Computation

From the results obtained, discussed in the previous chapter, we set limits on the number of observed signal events using the modified *Confidence Limit* computing procedure also known as the *CLs* technique. Using the number of observed events, the expected background events, the expected signal events according to the SPS8 benchmark GMSB model and the systematic uncertainties, we compute 95% Confidence Limit (CL) on the mean lifetime, $\tau_{\tilde{\chi}_1^0}$ (ns), and the mass of the $\widetilde{\chi}_1^0$, $m_{\tilde{\chi}_1^0}$ (GeV/c^2), or the effective SUSY breaking scale, $\mathbf{\Lambda}$ (TeV). We also produce a two dimensional limit in $\tau_{\tilde{\chi}_1^0}$ and $m_{\tilde{\chi}_1^0}$ (GeV/c^2) still using the CLs technique.

The acceptable statistical search and discovery experiment method by CMS is by computing *p-values* from the test statistics of the different hypothesis involved in the search. From these p-values, the confidence intervals or CL (in our case the CLs) is derived. The computation of the CL from the results of the hypothesis testing is according to the following procedure:

- A *NULL* (H_0) and an *Alternate* (H_1) hypothesis are defined. Additional hypothesis can also be defined, however, for limit computing two is enough,
- A Test statistics ($t(x)$), where x is the data, and its corresponding test statistics calculator are selected,
- The confidence interval is computed by inverting the results of the hypothesis test.

Before we discuss the limit computation, first, let us describe the CLs technique.

7.1.1 CLs Technique

The CL_s technique [60] is attributed as the standard technique or framework for computing the confidence or exclusion intervals in a search and discovery experiment. It has been tested and validated during the search for the Higgs boson at previous CERN experiment known as LEP and recently in the discovery of the scalar boson with mass, $m_H = 125.36 \pm 0.37(stat.Unc) \pm 0.18(syst.Unc)$, in 2012, by both CMS and ATLAS experiments.

The CL_s is defined as:

$$CL_s = \frac{CL_{s+b}}{CL_b} = \frac{p_{s+b}}{1 - p_b} \tag{7.1}$$

where $s+b$ means signal and background and CL_{s+b} or p_{s+b} is the p-value of the signal plus background hypothesis and CL_b or p_b is that for the background only hypothesis. The purpose of the using the CL_s method is to compute reliable upper limits in a search scenario when the observed signal is very small compared to the background. In the CL_s technique, one uses not the p-value (CL_{s+b}) but rather divide this by CL_b (which is 1 minus the p-value for background only hypothesis). The reason for this is to define a conditional probability conditioned to the scenario of observing only background or background only hypothesis.

In CMS, the CL_s method has been implemented in a unique statistical software package called *HiggsCombine* [62], with the goal of providing direct access to a variety of robust statistical methods with optimised performance for computing limits or confidence intervals. HiggsCombine is the official standard tool recommended by the CMS statistical committee and CMS Higgs group for calculating limits in any CMS search and discovery analysis. It takes as input estimates on the number or distribution of signal and background and the observed number or distribution from data and produces an upper limit in the production cross section of a given physics process for a given value of a parameter of interest (POI). Higgscombine tool has the advantage in that, it allows for the possibility to use several different statistical methods of calculating the upper limit. This way, one can make comparison and simple checks for any inconsistency. In this analysis, we used an Asymptotic [63], for testing and the HybridNew (a hybrid of

Frequentist and Bayesian methods) [62], to calculate our final observed limits.

7.1.2 Statistical Test Formalism

The Neyman-Pearson Theorem states that the likelihood ratio gives the most powerful hypothesis test. Therefore, we construct our test statistics t_μ as a function of the observed data, as a likelihood ratio. In a search analysis, one defines the null hypothesis H_0 describing only known processes, or the background only which is to be tested against an alternate hypothesis H_1 defined as a background and signal. However in the computation of upper limits:

- H_0 being the NULL hypothesis includes the background and signal $(s + b)$ while
- H_1 being the ALTERNATE hypothesis includes only the background (b).

Using these, two hypothesis we quantify the level of agreement between our observed data with either of the hypothesis by computing a p-value (p-value if the probability under the assumption of a given hypothesis, of finding data of equal or greater incompatibility with the predictions of the given hypothesis). A given hypothesis is then regarded as being excluded if its p-value is observed below a given threshold. In particle physics, this threshold value for the p-value is 0.05 corresponding to 95% of confidence level (CL). The CMS accepted method of computing upper upper limit is based on mix of frequentist-hybrid significance test using the profilelikelihood ratio as a test statistics (HybridNew method). The parameter of interests in in our case the rate (cross section) of signal process as well as *nuissance parameters* as systematics for the background and signal models. This parametrized systematics effects results, as is always the case, to loss in sensitivity.

In this search experiment, for each event in the signal, we measured the timing of the photon as our observable. We use this value to construct a histogram $\mathbf{n} = (n_1, \cdots, n_N)$. The expectation value for each value of n_i can be written as:

$$E[n_i] = \mu s_i + b_i \tag{7.2}$$

where μ is the parameter which determines the signal strength, when $\mu = 0$ means background-only and when $\mu = 1$ then we have the signal and background hypothesis.

The the mean number of entries in the ith bin from signal and background are given as:

$$s_i = s_{tot} \int_{bin,i} f_s \left(t; \theta_{\mathbf{s}}\right) \quad b_i = b_{tot} \int_{bin,i} f_b \left(t; \theta_{\mathbf{b}}\right) \tag{7.3}$$

with the functions $f_s \left(t; \theta_{\mathbf{s}}\right)$ and $f_b \left(t; \theta_{\mathbf{b}}\right)$ being the probability density functions (Pdfs) of the variable t for the signal and background events and $\theta_{\mathbf{s}}$ and $\theta_{\mathbf{b}}$ representing the parameters which characterise the shapes of the pdfs. s_{tot} and b_{tot} represents the total mean numbers of signals and backgrounds while the integrals represent the probabilities for an event to be found in bin i. $\theta = (\theta_{\mathbf{s}}, \theta_{\mathbf{b}}, b_{tot})$ denote all nuisance parameters (systematic uncertainties) while s_{tot} is the signal normalization is fixed to the value predicted by the nominal signal model.

The likelihood function is the product of the Poisson probabilities for all bins:

$$\mathcal{L} \left(\mu, \theta\right) = \prod_{r=1}^{N} \frac{\left(\mu s_r + b_r\right)^{n_r}}{n_r!} e^{-\left(\mu s_r + b_r\right)} \cdot \mathcal{G}(\theta) \tag{7.4}$$

where $\mathcal{G}(\theta)$ is a discrete (Poisson) distribution of the nuisance parameters. This distribution can be different for different nuisance parameter.

Using the likelihood function, the profilelikelihood ratio is then defined as:

$$\lambda(\mu) = \frac{\mathcal{L}(\mu, \hat{\hat{\theta}})}{\mathcal{L}(\hat{\mu}, \hat{\theta})} \tag{7.5}$$

Here $\hat{\hat{\theta}}$ is the the value of θ that maximizes $\mathcal{L}$ for a specified μ, thus, it is referred to as the *conditional maximum-likelihood estimator* (CMLE) of θ (given as a function of μ). While $\mathcal{L}(\hat{\mu}, \hat{\theta})$ is the maximized (unconditional) likelihood function with $\hat{\mu}$ and $\hat{\theta}$ being its *maximum likelihood* (ML) estimators. The nuisance parameters broadens the profilelikelihood as a function of μ relative to what is expected if their values where fixed and this reflects in the loss of sensitivity or information about μ due to the systematic uncertainties.

7.1.3 Test statistics and p-values

The above expression for $\lambda(\mu)$ shows that $0 \leq \lambda \leq 1$, where λ close to 1 indicates a very good agreement between the data and hypothesis value of μ. The test statistics to be used for our statistical test is defined as:

$$t_\mu = -2 \ln \lambda(\mu) \tag{7.6}$$

It is important to note that the test statistics approach to any statistical test is favourable because just be looking at the values of the test statistics, higher values corresponds to increasing incompatibility between the data and the value of μ which is from the signal hypothesis. This incompatibility or disagreement between the data and a given hypothesis is quantified by calculating the probability or p-value as:

$$CL_{s+b} = p_u = \int_{t_{\mu,obs}}^{\infty} f(t_\mu|\mu) dt_\mu \tag{7.7}$$

where, $t_{\mu,obs}$ is the value of the test statistics t_μ obtained from the data and $f(t_\mu|\mu)$ is a pdf constructed from t_μ depending on the signal strength μ. The set of values for μ that a rejected because their p-value is below a specified threshold value α lying on either sides of those not rejected gives a two sided confidence interval of μ and if just on one side of the ones not rejected gives an upper limit on the rejected values of μ.

In the background only scenario i.e $\mu = 0$, the test statistics is defined as:

$$q_\mu = \begin{cases} -2 \ln \lambda(0), & \hat{\mu} \geq 0 \\ 0, & \hat{\mu} \leq 0 \end{cases}$$

where $\lambda(0)$ is the profilelikelihood ratio for $\mu = 0$ defined in 7.5. and again to quantify the disagreement between the background-only hypothesis ($\mu = 0$) and the data is given by the p-value as:

$$CL_b = p_0 = \int_{q_{0,obs}}^{\infty} f(q_0|0) dq_0 \tag{7.8}$$

where $f(q_0|0)$ denotes the pdf if the test statistics q_0 under the background-only ($\mu = 0$) hypothesis. Figure 7.1 shows a sampling distributions of the test statistics and how the

p-values can be extracted from these distributions.

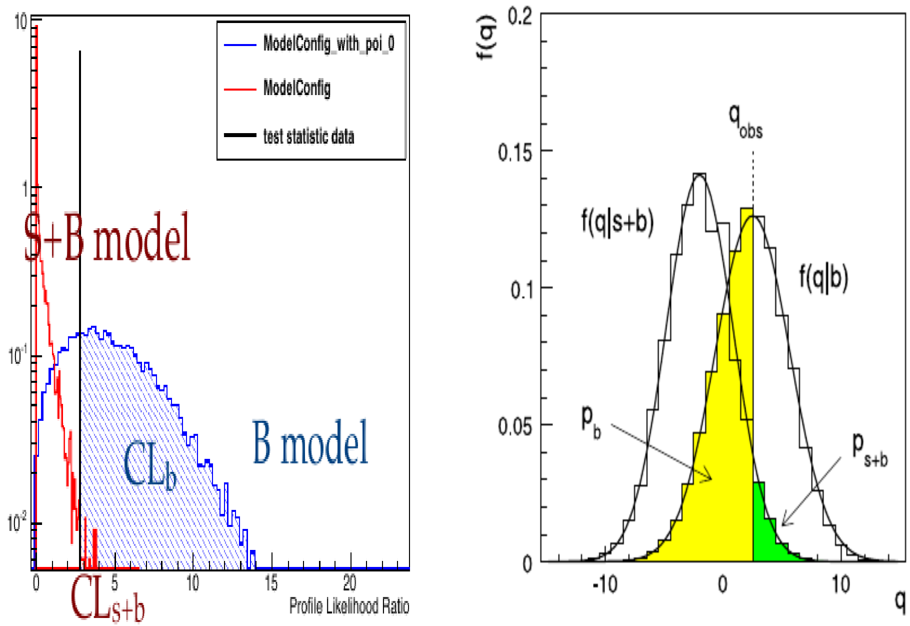

Figure 7.1: Sampling distributions for $f(t_\mu|\mu)$ showing how one extracts the p-vlaues. left: is the using a analytic of the Asymptotic method and right: is from the HybridNew method.

In addition to the p-value, for expressing the disagreement between the data and a given hypothesis, the Higgscombine tool also provides a quantity known as the *significance* ($\mathcal{Z}$). $\mathcal{Z}$ and the p-value have a very non-linear relation. Once can defined that relation using a two-sided fluctuation if a Gaussian variable σ, with 5σ significance corresponding to a p-value of $p = 5.7 \times 10^{-7}$ to denote a discovery. Since, we have not observed any significant excess of events over our standard model background, we will not mention a lot about significance in this thesis, but rather talk about p-values as they are indispensable in computing limits.

The important question is always, how does one obtain an expression or a distribution of the test statistics and $f(t_\mu|\mu)$ from the likelihood function? To answer this question, the HiggsCombine tool was developed which consist of various ways of both analytically (e.g the Asymptotic statistical method [63]) or through numerical integration or Monte Carlo computation (e.g the HybridNew statistical method) obtain the test statistics and $f(t_\mu|\mu)$. We have shown the limit computation results of both methods as used in this analysis. As an example, the pdf $f(q_\mu|\mu)$ of the test statistics (q_μ) obtained though the Asymptotic statistical method as given in [63] is:

$$f(t_\mu|\mu') = \mathbf{\Phi}\left(\frac{\mu-\mu'}{\sigma}\right)\delta(t_\mu) + \frac{1}{2}\frac{1}{\sqrt{2\pi}}\frac{1}{t_\mu}\exp\left[-\frac{1}{2}\left(\sqrt{t_\mu} - \frac{\mu-\mu'}{\sigma}\right)^2\right] \tag{7.9}$$

where result to a half-chi-square distribution when $\mu = \mu'$.

In subtle point worth mentioning is that in the HybridNew approach, systematics uncertainties are taken into account through the Beyesian prior density $\pi(\theta)$, and the distribution of the test statistics is computed under the assumption if the Beyesian model of average given as:

$$f(q) = \int f(q|\theta)\pi(\theta)d\theta$$

and the prior pdf $\pi(\theta)$ is obtained from some measurements characterised by a given likelihood function $\mathcal{L}_\theta(\theta)$ which is then used to find the prior using Bayes' Theorem. Unlike other cases where systematic uncertainties are taking as being part of the data and incorporated directly through $\mathcal{G}(\theta)$ as shown in equation 7.4. Nevertheless, they arrive at the same result.

In summary, the hypothesis test is performed using a given statistical method on each value of a chosen parameter of interest (POI)(usually denoted μ). The p-value if obtained from the sampling distribution of the test statistics being used. Can either obtain this test statistics analytically or through Monte Carlo computation and numerical integration. By plotting the p-value as a function of the POI, we obtain the p-value curve (in this case the $CL_s = \frac{CL_{s+b}}{CL_b}$). The value of μ which has a p-value α (e.g 0.05) is the upper limit (for 1-dimensional limits,2-dimensional limits gives lower and upper limits) of $1-\alpha$ confidence interval (e.g 95%).

Chapter 8

Limit Interpretation

Using the CL_s technique, the HiggsCombine tool produces an upper limit along with the expected limit at different quantiles as the signal strength computed which is a ratio of Number of Signal events over the Number of Expected signal events i.e

$$r = \frac{N^{Obs}}{N_{expect}} \tag{8.1}$$

and using the equation as given in chapter 3 on the cross-section $\sigma = \frac{N}{\varepsilon \cdot A \cdot \mathscr{L}}$ and hence the observed cross-section upper limit is given as:

$$\sigma_{UL}^{Obs} = \frac{r \cdot N^{expect}}{\varepsilon \cdot A \cdot \mathscr{L}} \tag{8.2}$$

where $\mathscr{L}$ is the integrated luminosity ($19\,\mathrm{fb}^{-1}$) and ε and A are the signal selection efficiency and Acceptance respectively. In addition to the observed limits (Solid black line), the uncertainties on the expected limits at 68%/16% ($\pm 1\sigma$) and at 98%/2.5% ($\pm 2\sigma$) provide the GREEN and YELLOW respectively, the error from the median (50%) expected limits (dashed red line) shown in figure 8.2.

8.1 Signal Efficiency and Acceptance

After our final selection on MC signal sample, the number of signal events passing our selection requirements for different neutralino lifetime and same mass, $\Lambda = 180$ TeV, is given in table 8.1. We use these numbers and those for other neutralino lifetimes and masses to compute our exclusion limits.

SPS8 GMSB Signal	Number of Events
GMSB(SPS8) ($\Lambda = 180$ TeV,$c\tau = 250$ mm)	0.2096
GMSB(SPS8) ($\Lambda = 180$ TeV,$c\tau = 500$ mm)	4.5423
GMSB(SPS8) ($\Lambda = 180$ TeV,$c\tau = 1000$ mm)	6.3646
GMSB(SPS8) ($\Lambda = 180$ TeV,$c\tau = 2000$ mm)	6.3968
GMSB(SPS8) ($\Lambda = 180$ TeV,$c\tau = 4000$ mm)	6.1442
GMSB(SPS8) ($\Lambda = 180$ TeV,$c\tau = 6000$ mm)	4.6498
GMSB(SPS8) ($\Lambda = 180$ TeV,$c\tau = 12000$ mm)	2.918

Table 8.1: Final number for $\Lambda = 180$ TeV GMSB SPS8 MC signal events events passing our selection cuts.

The efficiency times acceptance ($\varepsilon \times A$) combined as one is seen the figure 8.1.

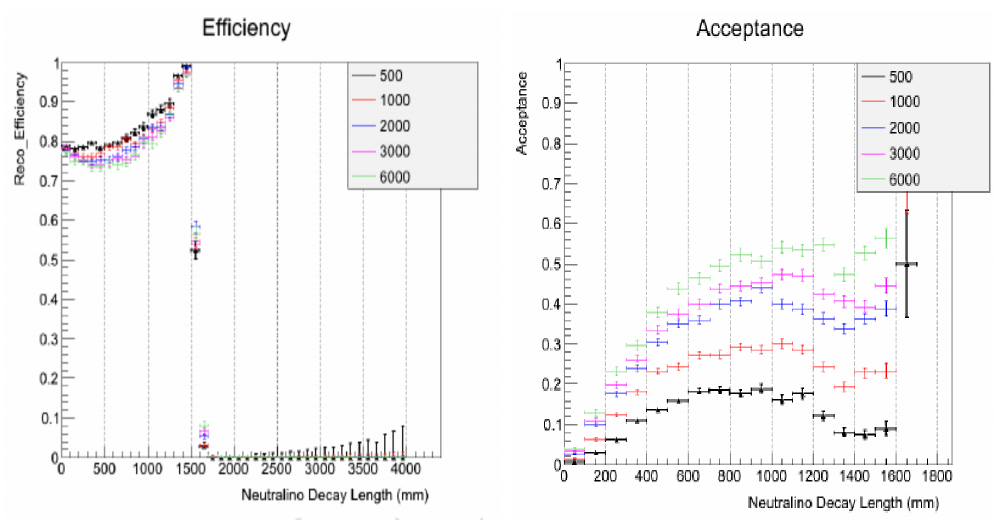

Figure 8.1: The reconstruction and selection efficiency (left) $\times$ Acceptance ($t >$ 3 ns) (right) against transverse decay length in laboratory frame for different $c\tau$ points.

8.2 Limits on SPS8 GMSB Model

The $\frac{N^{expect}}{\mathscr{L}}$ defines the expected signal cross section which is obtained from a given signal model. In our scenario, our choice of signal model we want to produce exclusion limits on the possible production and decay of a long-lived particle described by this signal model is GMSB. Thus the interpretation of our search analysis is given within the context of any GMSB model with a long-live neutral particle decaying to a photon and gravitino. Such a model is the minimal GMSB or the SPS8 model and the general GMSB model. However, the results provided are based on interpretation within the context of the SPS8 model. In GMSB, the neutralino $\tilde{\chi}_1^0$ is the NLSP and decays to the gravitino $\tilde{G}$ the LSP (as a result of R-parity conservation) in association with a very energetic photon γ. Because of the smallness in mass difference between the $\tilde{\chi}_1^0$ and the $\tilde{G}$ as well as the coupling, the $\tilde{\chi}_1^0$ decay to $\tilde{G}$ is delayed and as a result, the photon emitted can arrive late in the calorimeter crystals. Measuring the arrival time of the photon on ECAL crystals, we can extract important parameters of theory of GMSB.

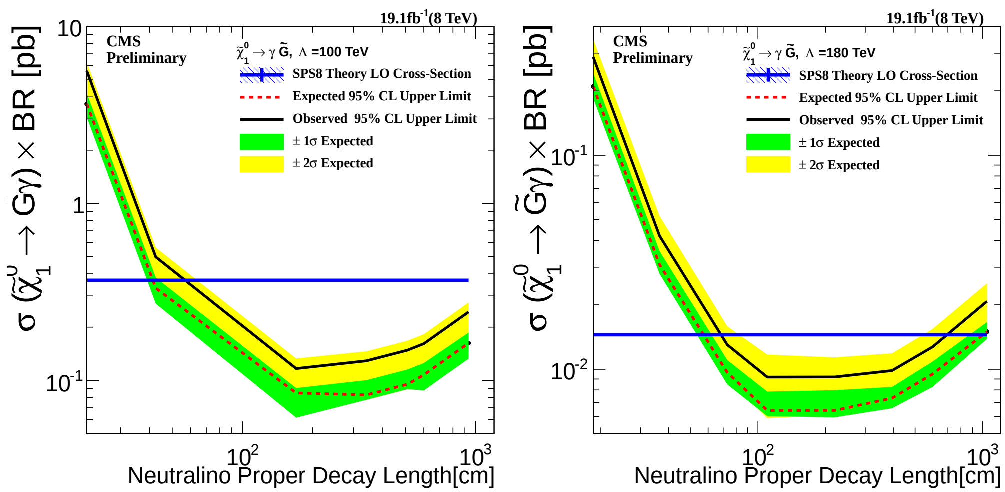

Figure 8.2: Neutralino production cross section against proper delay length upper limit interpretation in SPS8 model. (Left) $\Lambda = 100$ TeV, (Right)(left) $\Lambda = 180$ TeV

In the SPS8 model, the parameter space for long-live neutralinos is govern by $\Lambda_m - c\tau$ 2-dimensional parameter space. For each Λ_m point, we have a fixed neutralino mass with different proper lifetimes $c\tau$. We have obtained limits for Λ_m ranging from 100 TeV to 180 TeV corresponding to lightest neutralino mass $m_{\tilde{\chi}_1^0}$ between 90 to 255 GeV/c^2 and proper lifetime $c\tau$ ranging from 250 to 12000 mm corresponding to $\tau_{\tilde{\chi}_1^0}$ from 0.8 ns to 40 ns.

For a given value of $\Lambda_m = 180$ TeV, we have a lightest neutralino production cross section times branching ratio plot shown in figure 8.2, showing that the ECAL detector is sensitive to lightest neutralinos of mass $m_{\tilde{\chi}_1^0} = 255\ GeV/c^2$ and life time upto 30 ns and we are 95% confident that we have not missed any neutralino whose mass is $m_{\tilde{\chi}_1^0} = 255\ GeV/c^2$ and lifetime is $\tau \leq 30$ ns.

For a given lifetime of $\tau = 20$ ns, we can also obtain upper limits on the production cross section times branching ratio when compared against their theoretically expected values for a lightest neutralino with mass ranging from $m_{\tilde{\chi}_1^0} = 90\ GeV/c^2$ to $m_{\tilde{\chi}_1^0} = 255\ GeV/c^2$. The observed upper limit on this cross section is $\sigma^{UP}_{\tilde{\chi}_1^0} \geq XX$ pb with proper lifetime of $\tau = 30$ ns.

Using both the mass and proper lifetime of the lightest neutralino, we present possible 2-dimensional limits simultaneously on $m_{\tilde{\chi}_1^0}$ or Λ_m and $c\tau$ or τ in the SPS8 model, comparing this with the result of previous experiments. This is shown in Figure 8.3.

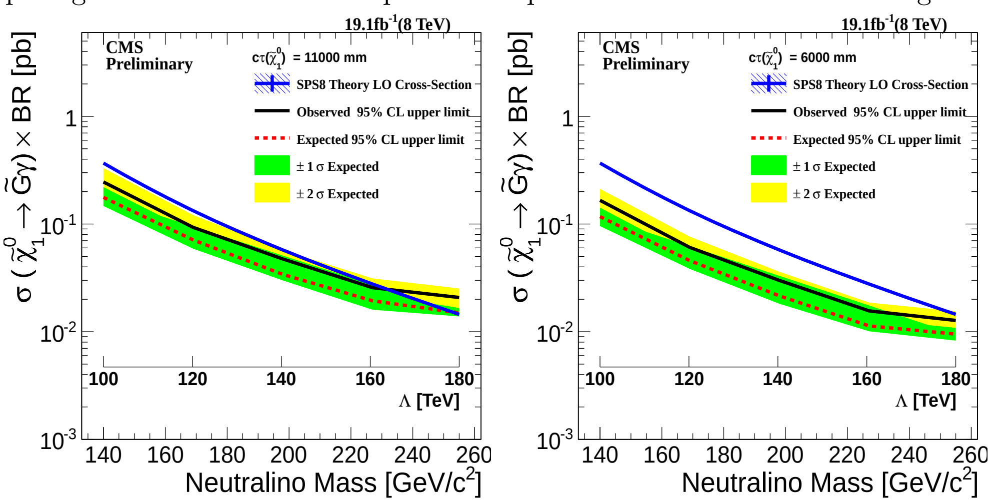

Figure 8.3: Neutralino production cross section against neutralino mass upper limit at 95% confidence levels interpretation in SPS8 model.(Left) $C\tau = 11000$ mm, (Right) $C\tau = 6000$ mm

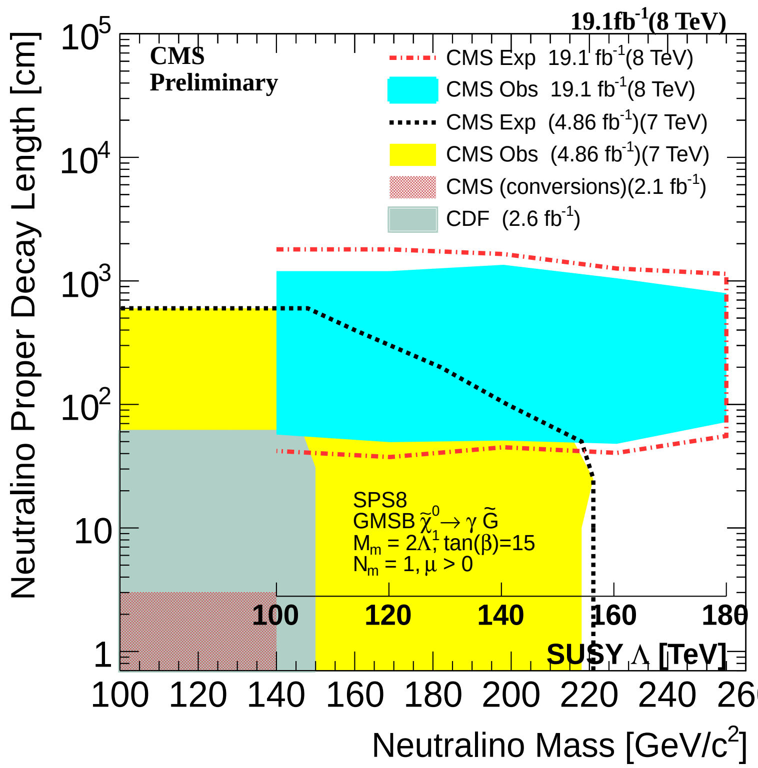

Figure 8.4: Neutralino two dimensional exclusion limit of neutralino mass (Λ) against proper delay length upper limit interpretation in SPS8 model in the decay $\tilde{\chi}_1^0 \to \gamma + \tilde{G}$ with limits from previous experiments shown.

Chapter 9

Conclusion

We have performed a search analysis for NMLLP decaying to photons using the time of arrival of the photon as measured by the ECAL sub detector of the CMS detector. Haven fail to find any significant signal of delayed photons over the standard model background, we interpreted our results in SUSY models with NMLLP like SPS8 of minimal GBSM or general GMSB models. We showed that, neutralinos whose production and decay mechanism is described in the SPS8 mGMSB model, with $m_{\tilde{\chi}_1^0} \leq 235\ GeV/c^2$ and $\tau_{\tilde{\chi}_1^0} \leq 35$ ns are ruled out of existence at 95% confidence level using the 2012 8 TeV LHC dataset. This corresponds to an upper limit of $\sigma^{UP}_{\tilde{\chi}_1^0} \geq 0.02$ pb on the production cross section times branching ratio in a hadron collider. In addition, we mention some of the limitations in this particular analysis from a detector point of view and how in future studies can be improved. We hope that in the future, with increase in center of mass energy of the LHC collider as well as luminosity and an improve in timing resolution beyond what is already very reliable, we will surely find a new fundamental particle whose dynamics cannot be described by the already very successful standard model of particle physics.

Bibliography

[1] N. Jarosik et al. (WMAP), Astrophys. J. SUppl. **192**, 14 (2011); Overview: K.A. Olive et al.(PDG), Chin.Phys.C**38**,090001(2014).

[2] Ellis John, Olive Keith A. (2010). *Supersymmetric Dark Matter Candidates.* arXiv:1001.3651 [astro-ph]

[3] Laura Covi, *Gravitino Dark Matter confronts LHC* Journal of Physics: Conference Series 485 (2014) 012002

[4] M. Kuhlen, M Vogelsberger, R. Angulo, Phys.Dark Univ.**1**,50(2012).

[5] J.Ellis, J.Hagelin, D. Nanopoulos, K.A. Olive and M. Srednicki; *Nucl. Phys.* B238 (1984) 453; H. Goldberg, *Phys. Rev. Lett* 50 (1983) 1419; J. Ellis, T. Falk, G. Ganis, K.A. Olive and M. Srednicki, *Phys. Lett.* B 510 (2001) 236, arXiv: hep-ph/0102098.

[6] K.A. Olive et al. (Particle Data Group), Chin. Phys. C, 38, 090001 (2014).

[7] Steven Weinberg, *A Model of Leptons*, *Phys. Rev. Lett.* 19, 12641266 (1967)

[8] Peter W. Higgs *Broken symmetries and the masses of gauge bosons*, *Phys.Rev.Lett.13.508*,19 October, 1964;

[9] *Observation of a new boson at a mass of 125 GeV with the CMS experiment at LHC*, *Phys. Lett. B 716 (2012) 30-61*

[10] Haag, Rudolf; Sohnius, Martin; opuszaski, Jan T. *All possible generators of supersymmetries of the S-matrix*, Nuclear Physics B 88: 257274 (1975),

[11] Salam, A.; Strathdee, J. (1974). *Super-gauge transformations.* Nuclear Physics B 76 (3): 477201,

[12] Ian J R Aitchison, *Supersymmetry and the MSSM: An Elementary Introduction*, arXiv:hep-ph/0505105,

[13] S.Mathin,*Supersymmetry Primer*, arXiv:hep-ph/9709356,

[14] Howard Baer, Xerxes Tata, *Weak Scale Supersymmetry:From Superfields to Scattering Events.*

[15] H. Nilles, *Supersymmetry, Supergravity and Particle Physics*, Phys. Rept. 110(1984) 1.

[16] G.F. Giudice and R. Rattazzi *Theories with Gauge-Mediated Supersymmetry Breaking* arXiv:hep-ph/9801271v2.

[17] S. Ambrosanio 1 , Graham D. Kribs 2 , and Stephen P. Martin hep-ph/9703211 arXiv:hep-ph/9703211v2.

[18] B.Allanach et al,arXiv:hep-ph/0202233v1.

[19] D.del Re et al, *An algorithm for the determination of the flight path of long-lived particles decaying into photons*, CMS AN -2010/212.

[20] ISAJET 7.84, F.E. Paige, S.D. Protopopescu, H. Baer and X. Tata, http://www.nhn.ou.edu/ isajet/

[21] T. Sj ostrand, S. Mrenna, and P. Skands, *PYTHIA 6.4 physics and manual*, JHEP 05 (2006) 026, doi:10.1088/1126-6708/2006/05/026, arXiv:hep-ph/0603175

[22] GEANT4 Collaboration, *GEANT4a simulation toolkit*, Nucl. Instrum. Meth. A 506(2003) 250, doi:10.1016/S0168-9002(03)01368-8.

[23] J.Dann et al.(LEPSUSY Working Group), Internal note LEPSUSYWG/97-04(1997), P. Janot, talk at the EPS Conference, Jerusalem, 1997.

[24] CDF Collaboration, *Search for Supersymmetry with Gauge-Mediated Breaking in Diphoton Events with Missing Transverse Energy at* CDFII,*Phys. Rev. Lett.*

[25] ATLAS Collaboration *Search for Diphoton Events with Large Missing Transverse Momentum in 1 fb^{-1} of 7TeV Proton-Proton Collision Data with the ATLAS Detector*, arXiv:1111.4116v1,17th Nov 2011.

[26] CMS Draft Analysis,*Search for Long-Lived Particles using Displaced Photons in* PP *Collision at* $\sqrt{S} = 7$ *TeV*, CMS AN AN-11-081 104(2010)011801,

[27] ATLAS Collaboration, J. High Energy Phys. 1212, 124 (2012), arXiv:1210.4457 [hep-ex]

[28] The LHC Machine, Lyndon Evans and Philip Bryant *Jinst*,

[29] CMS Collaboration,*CMS Physics: Technical design report*, Volume 1 CERN-LHCC-2006-001.

[30] CMS Collaboration,*CMS Physics: Technical design report, Volume 2* CERN-LHCC-2006-001.

[31] A. Jeff et al *Measurement of Satellite Bunches at the LHC*, slac-pub-15737, slac-pub-16058.

[32] *Study of the LHC ghost charge and satellite bunches for luminosity calibration.*, CERN-ATS-Note-2012-029 PERF

[33] *LHC bunch current normalization for the April-May 2010 luminosity calibration measurements.*, CERN-ATS-Note-2011-004 PERF

[34] CMS Collaboration, *The CMS experiment at the CERN LHC*, JINST 0803:S08004, 2008.

[35] CMS Collaboration,*The electromagnetic calorimeter. Technical design report*,. CERN-LHCC-97-33.

[36] Bo Lofstedt, *The digital readout system for the CMS electromagnetic Calorimeter*,*Nucl. Inst. Methods in Physics Research*,A 453 (2000) 433-439.

[37] J. Valera et al *Trigger Synchronization Circuits in CMS*,CMS CR 1997/017.

[38] CMS Electromagnetic Calorimeter Collaboration, *Energy resolution of the barrel of the CMS Electromagnetic Calorimeter*,JINST 2(2007)P04004.

[39] CMS Collaboration, *Reconstruction of the signal amplitude of the CMS electromagnetic Calorimeter*, Eur.Phys.J. C46S1(2006)23-35.

[40] CMS Collaboration, *Time Reconstruction and Performance of the CMS Crystal Electromagnetic Calorimeter*,CFT-09-006, 2009.

[41] https://twiki.cern.ch/twiki/bin/viewauth/CMS/ECALDPGTimeCalibration

[42] https://twiki.cern.ch/twiki/bin/viewauth/CMS/ECALDPGHwTimeCalibration

[43] CMS Collaboration, *The CMS ECAL performance With examples*, JINST 9 C02008, 2014.

[44] Daniele Del Re for CMS Collaboration, *Timing performance of the CMS electromagnetic calorimeter and prospects for the future.*, CMS-CR-2014/074

[45] CMS-DP-2014/011: *ECAL Timing Performance Run1*

[46] https://twiki.cern.ch/twiki/bin/view/CMSPublic/EcalDPGResultsCMSDP2014011

[47] https://twiki.cern.ch/twiki/bin/view/CMSPublic/EcalDPGResultsCMSDP2014012

[48] Florian Beaudette (the CMS Collaboration), *The CMS Particle Flow Algorithm*, arXiv:1401.8155 [hep-ex].

[49] CMS Collaboration, *Particle-Flow Event Reconstruction in CMS and Performance for Jets, taus and* $\not\!\!E_{\rm T}$CMS Physics Analysis Summary CMS-PAS-PFT-09-001(2009).

[50] CMS Collaboration, *Jet Performance in pp Collisions at* $\sqrt{\boldsymbol{S}} = \mathbf{7}$ *TeV*, CMS PAS JME-10-003 (2010).

[51] CMS Collaboration, *8 TeV Jet Energy Corrections and Uncertainties based on 19.8* fb^{-1} *of data in CMS*, CMS-DP-2013-033 ; CERN-CMS-DP-2013-033, *Jet Energy Corrections and Uncertainties*, CMS Public Note CMS-DP-2012/012.

[52] CMS Collaboration, *Missing Transverse Energy Performance in Minimum-Bias and Jet Events from Proton-Proton Collisions at* $\sqrt{s} = 7$ *TeV*, CMS Physics Analysis Summary CMS-PAS-JME-10-004 (2010).

[53] CMS Collaboration, *Missing transverse energy performance of the CMS detector*, arXiv:1106.5048v1., Missing Transverse Energy, JINST ,arXiv:1106.5048.

[54] *Characterization and treatment of anomalous signals in the CMS Electromagnetic Calorimeter* CMS AN AN-10-357.

[55] *Mitigation of Anomalous APD signals in the CMS ECAL,2013, JINST 8 C03020*, W.Bialas and D.A. Petyt.

[56] CMS Collaboration,*Determination of Jet Energy Scale in CMS with pp collisions at* $\sqrt{S} = 8$ *TeV*, JME-10-010(2012).

[57] "https://twiki.cern.ch/twiki/bin/viewauth/CMS/EGamma2012."

[58] CMS Collaboration, *Search for ADD Extra-dimensions with Photon + MET signature*, AN-11-319(2011).

[59] *Parton distributions for the LHC*, Eur.Phys.J C63(2009) 189-285 or arXiv:0901.0002.

[60] *Presentation of search results: the CLs technique*,A L Read 2002 J. Phys. G: Nucl. Part. Phys. 28 2693.

[61] *Computation of confidence levels for search experiments with fractional event counting and the treatment of systematic errors*, Peter Bock JHEP01(2007)080.

[62] https://twiki.cern.ch/twiki/bin/viewauth/CMS/

[63] *Asymptotic formulae for likelihood-based tests of new physics*,G. Cowan et al, arXiv:1007.1727v3.

Appendix A

Glossary and Acronyms

Care has been taken in this thesis to minimize the use of jargon and acronyms, but this cannot always be achieved. This appendix defines jargon terms in a glossary, and contains a table of acronyms and their meaning.

A.1 Glossary

- **Cosmic-Ray Muon** (**CR** μ) – A muon coming from the abundant energetic particles originating outside of the Earth's atmosphere.
- **SUSY** – A theoretical model based on a fundamental symmetry called supersymmetry in which the fermions and bosons can exchange their spin, extending the standard model to account for the stability in the observed Higgs boson mass and to also predicting the existence of many extra new particles which could be candidates of dark matter.
- **CMS Coordinate System** – CMS uses a right-handed coordinate system, with the origin at the nominal interaction point, the x-axis pointing to the center of the LHC, the y-axis pointing up (perpendicular to the LHC plane), and the z-axis along the counterclockwise-beam direction. The polar angle, θ, is measured from the positive z-axis and the azimuthal angle, ϕ, is measured in the x-y plane.
- **Eta** –

$$\boldsymbol{\eta = -\ln\tan(\theta/2)} \tag{A.1}$$

- **Transverse Energy and Momentum** – The transverse energy and momentum are defined as

$$E_{\mathrm{T}} = E \sin\theta \tag{A.2}$$

$$p_{\mathrm{T}} = p \sin\theta \tag{A.3}$$

where p is the momentum measured in the tracking system and E is the energy measured in the calorimeters.

- **Missing Transverse Energy** or $E_{\mathrm{T}}^{\mathrm{miss}}$–

$$\boldsymbol{E}_{\mathbf{T}}^{\mathrm{miss}} = |-\sum_{i} \boldsymbol{E}_{\mathbf{T}}^{i} \vec{\boldsymbol{n}}_{i}| \tag{A.4}$$

where $\vec{n_i}$ is a unit vector that points from the interaction vertex to the transverse plane.

A.2 Acronyms

Table A.1: Acronyms

LLNP	Long-Lived Neutral Particle.
DM	Dark Matter.
DE	Dark Energy.
SM	Standard Model
BSM	Beyond Standard Model
SUSY	Supersymmetry
GMSB	Gauge Mediated Supersymmetry Breaking
LHC	Large Hadron Collider
CMS	Compact Muon Solenoid
CRμ	Cosmic-Ray Muon

A.3 Analysis How To and Data Samples

A.3.1 Check Out Software Packages

To check out the analysis packages, do the following steps:

- `cmsrel CMSSW_5_3_29`
- `cd CMSSW_5_3_29\src`

A.3.2 Data Samples

In Table A.2 show the data samples and the corresponding integrated luminosity. The *jason* file with the list of certified good luminosity sections is **Cert_8TeVPromptReco_Colllisions12_JASON.txt**.

Data Sample	**Recorded Luminosity** $[\mathrm{fb}^{-1}]$
`/Run2012B/SinglePhoton/EXODisplacedPhoton-PromptSkim-v3`	5.1
`/Run2012C/SinglePhoton/EXODisplacedPhoton-PromptSkim-v3`	6.9
`/Run2012D/SinglePhoton/EXODisplacedPhoton-PromptSkim-v3`	7.1
`/SingleElectron/Run2012A-22Jan2013-v1/AOD`	5.2
`/DoubleElectron/Run2012C-22Jan2013-v1/AOD`	4.8

Table A.2: Data samples and their corresponding integrated luminosity totaling 19.1 fb^{-1} used in the our delayed photon search analysis